



KAPITAŁ LUDZKI
NARODOWA STRATEGIA SPÓJNOŚCI



Politechnika Wroclawska

UNIA EUROPEJSKA
EUROPEJSKI
FUNDUSZ SPOŁECZNY



ROZWÓJ POTENCJAŁU I OFERTY DYDAKTYCZNEJ POLITECHNIKI WROCŁAWSKIEJ

Wrocław University of Technology

Electronics, Photonics, Microsystems

Leszek Golonka (Chapters 1-5)

Karol Malecha (Chapters 6-9)

CERAMIC MICROSYSTEMS

Wrocław 2011

Wrocław University of Technology

Electronics, Photonics, Microsystems

Leszek Golonka (Chapters 1-5)

Karol Malecha (Chapters 6-9)

CERAMIC MICROSYSTEMS

Wrocław 2011

Copyright © by Wrocław University of Technology
Wrocław 2011

Reviewer: Andrzej Dziejic

ISBN 978-83-62098-29-3

Published by PRINTPAP Łódź, www.printpap.pl

CERAMIC MICROSYSTEMS

Contents

i

Chapter 1. Thick film materials and processing	1.1
1.1. Introduction	1.1
1.2. Thick film manufacturing process	1.2
Substrate	1.3
Paste	1.4
Design	1.9
Screen	1.10
Screen printing	1.11
Firing process	1.12
Trimming process	1.14
Assembling and packaging	1.15
References	1.17
Chapter 2. LTCC (Low Temperature Cofired Ceramics) materials and processing	2.1
2.1. Introduction	2.1
2.2. Multichip Module (MCM)	2.1
2.3. LTCC manufacturing process	2.3
2.4. Properties of cofired LTCC module	2.6
2.5. Design of LTCC module	2.9
2.6. Integrated passive components	2.12
2.7. Microwave application	2.16
2.8. LTCC processes for microsystems	2.17
References	2.18
Chapter 3. Sensors, actuators and microsystems – fundamentals and classification	3.1
3.1. Introduction	3.1
3.2. Fundamentals	3.1
3.3. Physical and chemical sensors	3.3
3.4. LTCC microsystems – general information	3.5
3.5. MEMS, MOEMS packaging	3.7

3.6. Heating and cooling systems	3.9
3.7. Energy source	3.11
References	3.14

Chapter 4. LTCC and thick film physical sensors	4.1
--	------------

4.1. Temperature sensors	4.1
Thermocouples	4.1
RTD (Resistive Temperature Device) sensors	4.3
Thermistors	4.6
4.2. Flow sensors	4.10
4.3. Pressure sensors	4.13
4.4. Force sensors	4.17
4.5. Proximity sensor	4.17
References	4.19

Chapter 5. LTCC and thick film chemical sensors	
--	--

5.1. Humidity sensors	5.1
Ceramic humidity sensors	5.4
5.2. Gas sensors	5.7
Semiconductor gas sensors	5.7
Electrochemical gas sensors	5.10
References	5.11

Chapter 6. Foundation of microfluidics	6.1
---	------------

6.1. Introduction	6.1
6.2. Basic terms and equations of fluid dynamics	6.2
Reynolds number	6.2
The continuity equation	6.4
Navier-Stokes equation	6.6
Pressure drop	6.8
6.3. Scaling laws in microfluidics	6.10
References	6.16

Chapter 7. Technology of the LTCC-based microfluidic systems	7.1
<hr/>	
7.1. Introduction	7.1
7.2. Laser processing of green ceramic tapes	7.3
7.3. Mechanical machining of green ceramic tapes	7.7
7.4. Hot embossing	7.9
7.5. Jet vapor etching	7.12
7.6. Photolithographic patterning	7.14
7.7. Photoformable LTCC tapes	7.15
7.8. Sacrificial volume material	7.18
7.9. Low pressure lamination methods	7.24
References	7.29
Chapter 8. Bonding techniques of the LTCC with different materials	8.1
<hr/>	
8.1. Introduction	8.1
8.2. LTCC-Si	8.1
8.3. LTCC-glass	8.5
8.4. LTCC-PDMS	8.8
8.5. LTCC-ceramic	8.11
References	8.12
Chapter 9. LTCC-based microfluidic systems	9.1
<hr/>	
9.1. Introduction	9.1
9.2. Microvalves and micropumps	9.1
Piezoelectric action	9.1
Piezoelectric valve	9.4
Piezoelectric pump	9.6
Electromagnetic actuation	9.8
Electromagnetic valve	9.9
Electromagnetic pump	9.11
9.3. Ceramic micromixers	9.13
Magneto-hydro-dynamic (MHD) mixer	9.15
Serpentine passive mixres	9.17
9.4. Microreactors	9.20
Enzymatic microreactor for urea determination	9.20

PCR (Polymerase Chain Reaction) microreactor	9.23
9.5. Electrochemical sensors	9.26
Potentiometric sensor with ion selective (ISE) based array	9.26
PDMS/ceramic module for potentiometric determination of urea	9.29
Amperometric sensor for continuous glucose monitoring	9.31
Electrochemical sensor for heavy metal determination in biological and environmental fluids	9.34
9.6. Optical sensors	9.35
LTCC-based microfluidic sensor for absorbance measurement	9.35
LTCC-based fluorescent sensor	9.37
LTCC-based microfluidic system with optical detection	9.39
References	9.40

Chapter 1

Thick film materials and processing

1.1. Introduction

In the thick film technology, the individual layer is deposited by screen printing on the insulator substrate. The thick film material is referred to as an ink or paste. The paste contains three main components: a functional phase (metal or oxide powder) which determines the electrical properties of the fired films, a binder (glass powder) which provides adhesion between the fired film and the substrate, and the organic vehicle which enables the screen printing process. After deposition the films are dried and then fired at the temperature around 850°C.

The screen print technique has been known for few thousand years. It was used in China to decorate ceramics with gold patterns. In electronics the technique was used for the first time around 1930 to make a silver electrode on a capacitor. The first thick film hybrid device was made in 1945 in the USA.

The mass production of thick film hybrid microelectronics started around 1960. Thirty years later the technology was also used for production of MCM (Multichip Module), sensors, actuators and microsystems. The pastes were deposited not only on alumina substrates but also on green ceramic tape to form a multilayer LTCC (Low Temperature Cofired Ceramics) module [1-6].

Advantages of thick film technology:

- low cost,
- simple automation,
- inexpensive production of short series,
- miniaturisation,
- very good electrical properties,
- production of various components,
- resistance to high temperatures,
- good mechanical properties.

Disadvantages:

- dimensions,
- no active components,
- tolerance.

Thick film components:

- conductor,
- resistor,
- capacitor,
- inductor,
- sensor,
- actuator,
- microsystem,
- thermistor,
- varistor,
- heaters,
- . . .

This chapter will focus on the basic technology for thick film materials with an emphasis on composition, design, processing and properties of the thick film components.

1.2. Thick film manufacturing process

After printing, the pastes are typically dried at 150°C for 10 min to remove the volatile solvent component of the vehicle. Next, the film is fired in a tunnel oven with a temperature profile which includes 10 min at a peak temperature of 850°C and an overall firing cycle time from 30 to 60 min. The process is shown in Fig. 1.1. Precious metal conductors are fired in air while copper requires firing in nitrogen. The print, dry, and fire steps are repeated to fabricate the final structure. The process can be automated for low cost, high volume production.

Typical parameters of thick films:

- film thickness \approx 5-15 μm (dielectric 50 μm)
- width (min) \approx 100 μm (min 15 μm)

conductor film – Au, Ag, PdAg . . .
 resistor film – RuO₂ , IrO₂ , Bi₂Ru₂O₇ ,

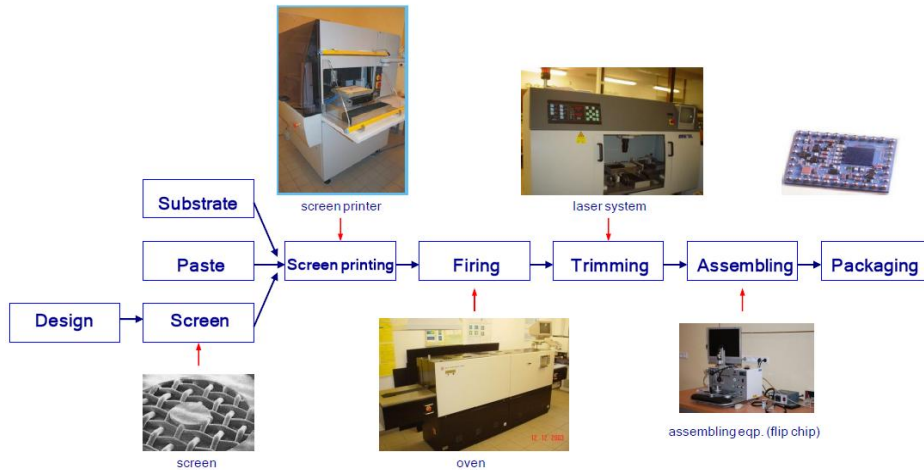


Fig. 1.1. Thick film technology process

Substrate

The substrate provides conductive traces for electrical interconnections between various passive and active components, mechanical support and a path for heat removal from the device. Typical substrate materials and properties are presented in Table 1.1. Alumina (96% Al₂O₃) is the most widely used substrate for thick film hybrids. Alumina combines a reasonable thermal conductivity and Coefficient of Thermal Expansion (CTE) with high temperature process compatibility, high strength, and low cost. Aluminium nitride and beryllia are used in the applications requiring high thermal conductivity. The CTE of alumina nearly matches the gallium arsenide one, while the CTE of aluminium nitride is comparable to that of silicon [7].

Desirable properties of the substrate:

- resistance to very high temperatures,
- electric insulator,

- good thermal conductivity,
- proper CTE,
- surface flatness.

Substrate materials:

- alundum ceramics (96% Al_2O_3),
- AlN ceramics,
- BeO ceramics,
- enamel steel.

Table 1.1.

Summary of typical substrate materials

Ceramics	AlN	Al_2O_3	BeO	LTCC
Thermal Conductivity [W/m·K]	140-170	10-35	150-250	2-3
Coefficient of Thermal Expansion (CTE) [$10^{-6}/\text{K}$]	4.6	7.3	5.40	5.8-7
Resistivity [$\Omega\cdot\text{m}$]	4×10^{11}	$> 10^{14}$	10^{13} - 10^{15}	$> 10^{12}$
Electrical permittivity ϵ (1 MHz)	10	9.5	7	5.9-9

Paste

The paste contains three components: the main ingredient (functional phase - metal or oxide powder) which determines the electrical properties of the fired films, the binder (glass powder) which provides adhesion between the fired film and the substrate, and the organic vehicle which enables the screen printing process.

- **Main ingredient** (powdered functional phase):
 - conductive paste - Au, Ag, PdAg, ...
 - resistive paste - RuO_2 , IrO_2 , $\text{Bi}_2\text{Ru}_2\text{O}_7$,

- **Glass** (powdered glass phase):
PbO - B₂O₃ - SiO₂ (or without PbO)

- **Organic vehicle:**

- solvent
 - viscosity (η) correction,
 - reduction of surface tension,
 - improving of wetting,

Ethylcellulose - adhesion to substrate after drying at the temperature of 120°C.

All the components are mixed together. The paste productivity depends on the quality of the paste, screen density and emulsion thickness. Typical productivity is presented in Table 1.2.

Table 1.2.

Paste productivity

	Substrate coverage [cm ² /g]	Screen [mesh]
Au	45 ÷ 55	325
Pt-Au	40 ÷ 45	200
Pd-Ag	65 ÷ 75	200
Pt-Ag	55 ÷ 65	200
Cu	65 ÷ 75	240
Dielectric paste	75 ÷ 85	200

Emulsion thickness: 10 ÷ 12 μ m

Mesh –number of openings in 1 inch length

Conductor paste

The functional phase for conductors may be made of gold, palladium-gold, platinum-gold, silver, palladium-silver, platinum-silver or copper. The

choice of the metallurgy depends on bondability or solderability of the wire, environmental requirements, electrical conductivity and the cost [7]. A comparison of various conductors is provided in Table 1.3.

Thick film conductor sheet resistance $R_{\square} = \rho/d = 2 \div 100 \text{ m}\Omega/\square$

where: ρ - resistivity of film

d – film thickness

Materials fired in air: Au, PtAu, PdAu, Ag, PtAg, PdAg
(disadvantage: Au – dissolution in solder,

Ag – diffusion)

Material fired in nitrogen: Cu

Application: electrode, connection, soldering pads etc.

Requirements: low resistivity, adhesion, solderability,

Table 1.3.

Properties of thick film conductors

Material	R_{\square} [m Ω / \square]	Material	R_{\square} [m Ω / \square]
Au	2 \div 10	PdAg	10 \div 50
Pt-Au	15 \div 100	Pt	50 \div 80
Pd-Au	10 \div 100	Cu *	2
Ag	2 \div 10	Ni *	7 \div 40

* firing in nitrogen

Resistor paste

Resistor systems are formulated with ruthenium (RuO₂, Bi₂Ru₂O₇, etc.) or IrO₂ doped glasses. Thick film resistor pastes provide a wide range of resistance values by varying the concentration of the glass. The most important resistor properties are sheet resistance (R_{\square}), Temperature Coefficient of Resistance (TCR) and stability. There are resistor systems for

general purposes, high voltage, potentiometric and sensor (high Gauge Factor) applications.

Sheet resistance (R_{\square})

$$R_{\square} = \rho/d = 10 \div 10^8 [\Omega/\square],$$

Temperature Coefficient of Resistance (TCR)

$$TCR = (R_2 - R_1) \times 10^6 / [R_1(T_2 - T_1)] = \pm (50 \div 300) [\text{ppm/K}]$$

where: R_1 – resistance at temperature T_1
 R_2 - resistance at temperature T_2

Cold TCR ($T_1 = 25^\circ\text{C}$, $T_2 = -55^\circ\text{C}$)

Hot TCR ($T_1 = 25^\circ\text{C}$, $T_2 = 125^\circ\text{C}$)

Piezoresistive properties - Gauge Factor (GF)

$$GF = (\Delta R/R) / (\Delta l/l) = 10 \div 20$$

where: ΔR – resistance change
 R - initial resistance
 Δl - length change
 l - initial length

Parameters of thick film resistors:

R_{\square}	$1\Omega/\square \div 100 \text{ M}\Omega/\square$
TCR	$\pm 50 \text{ ppm}/^\circ\text{C} \div \pm 300 \text{ ppm}/^\circ\text{C}$
d – film thickness	$5 \div 15 \mu\text{m}$
tolerance (without trimming)	$\pm 20\%$
P_r (alumina substrate 96% Al_2O_3)	$8 \text{ W}/\text{cm}^2$
P_p (for substrate surface)	$0.25 \text{ W}/\text{cm}^2$
S – noise index	$-35 \div +35 \text{ dB}$

P_r - max power density dissipated by the resistor (area of the resistor film)

P_p - max power density dissipated by the substrate (area of the substrate).

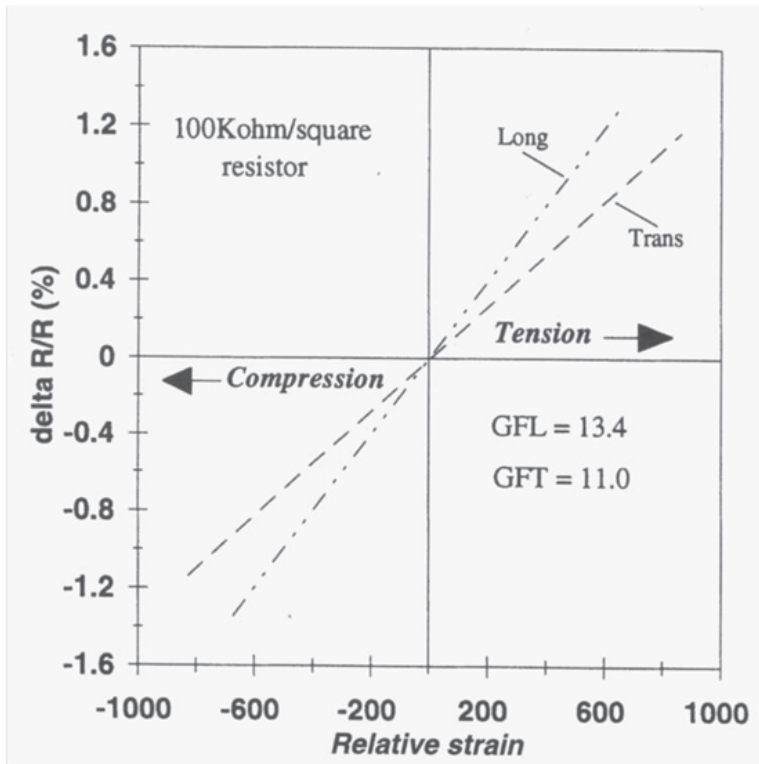


Fig. 1.2. Typical characteristic of piezoresistor [7]

Dielectric paste

Dielectric pastes are used for insulation between conductor layers, formation of capacitors and encapsulation of the hybrid substrate. Dielectric for insulation are typically glass-ceramics compositions with low dielectric constant, low dissipation factor, high voltage strength, high insulation

resistance and a CTE matched to the substrate. Thick film parallel plate capacitors are not widely used [7].

Other pastes: solder, thermistor, varistor, magnetoresistor, sensor, etc.

Design

The screen printing process is capable of resolving lines and spaces down to 100 μm or less. However, in high volume production it is advisable to restrict the resolution [7]. Typical thick film resistors guidelines are presented in Fig. 1.3, Fig. 1.4 and Table 1.4.

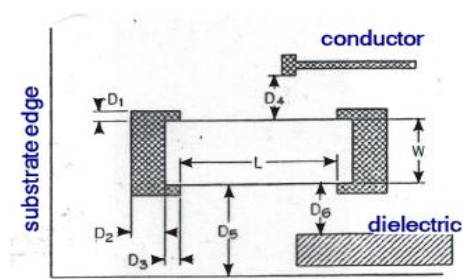


Fig. 1.3. Thick film resistor dimensions [7]

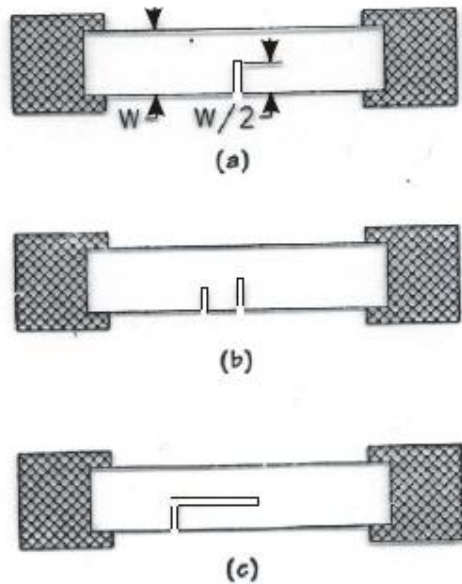


Fig. 1.4. Laser trim cut modes [7]

Table 1.4.

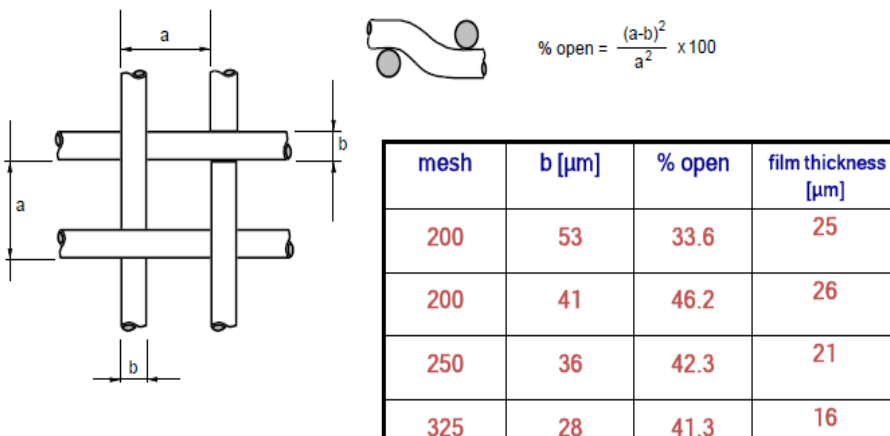
Thick film resistor dimensions (vide Fig. 1.3)

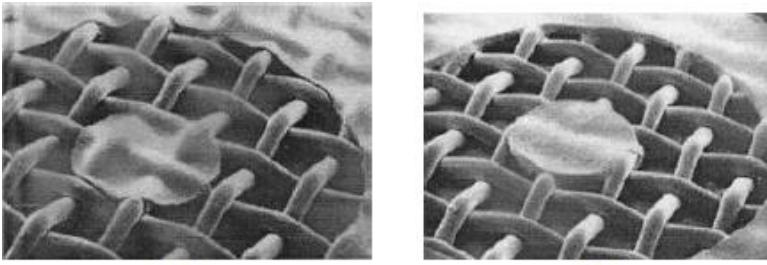
Dimension	Length [μm]	Remarks
L	1000 (500)	$0.5 < L/W < 5$ ($0.3 < L/W < 10$)
W		width depends on tolerance and power
D ₁	250 (125)	
D ₂	250 (125)	
D ₃	250 (200)	
D ₄	500 (375)	
D ₅	750 (500)	
D ₆	500 (500)	

(i) – in brackets minimal value

Screen

The screen is fabricated by stretching a fine stainless steel mesh screen over a frame and epoxying the mesh to the frame. The screen dimensions are presented in Fig. 1.5. The most important screen parameters are: mesh angle, screen frame size, screen mesh size and screen tension. The photosensitive emulsion is applied by one of two methods: by using liquid emulsion or by using a photosensitive film. The emulsion is exposed to the ultraviolet light to get the desired circuit pattern. The screen covered with emulsion is shown in Fig. 1.6. It is also possible to buy ready made screens, both with and without the emulsion.

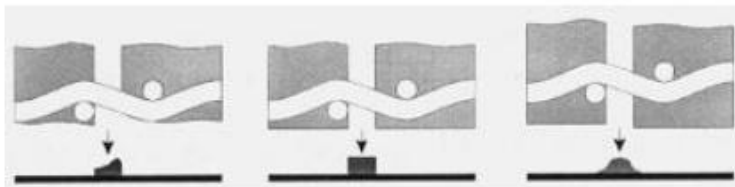
**Fig. 1.5.** Screen dimensions



(a)

(b)

**SEM picture of screen covered with emulsion.
Emulsion: (a) too thin, (b) proper thickness**



(a)

(b)

(c)

Emulsion: (a) too thin, (b) proper thickness, (c) too thick

Fig. 1.6. Screen covered with the emulsion [8]

Screen printing

The purpose of screen printing is to deposit a film of ink with predictable dimension on a substrate. The individual layer is deposited as illustrated in Fig. 1.7. Screen printing determines the accuracy of the printed pattern. The important process parameters in screen printing include screen printer setup (snap-off distance, speed, pressure), squeegee (hardness, shape), screen (wire diameter, mesh opening size, emulsion chemistry and thickness, screen tension) and paste rheology. The change in paste viscosity during the printing process is shown in Fig. 1.8.

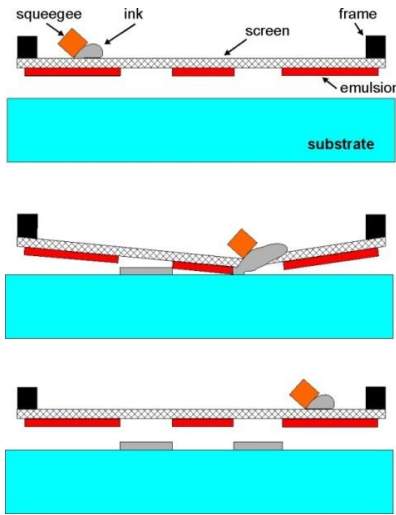


Fig. 1.7. Screen printing process [7]

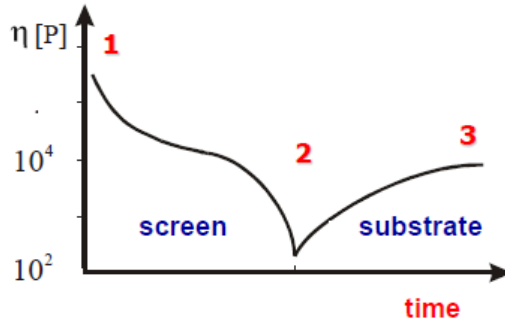


Fig. 1.8. Paste viscosity during printing process

Other methods of paste deposition on the substrate can also be used. Minimal width of the line and space between them for these methods are presented below:

	min. width / space [μm]
• standard screen printing	100 / 100
• fine line printing	40 / 75
• FODEL photosensitive paste	15 / 25
• photoimageable paste	25 / 25
• gravure-offset	15 / 25
• ink jet printing	30 / 30
• laser patterning	10 / 10

Firing process

A typical furnace profile used for thick film materials firing is shown in Fig. 1.9. Belt furnaces are commonly used for firing. At the first stage of the firing process (300 to 500°C) the nonvolatile resin portion of the vehicle is pyrolyzed. In the temperature range from 600 to 850°C, the glass flows,

sintering of the particles occurs, and chemical reactions take place to form the final product and to provide adhesion of the film to the substrate. The peak firing temperature is determined by the composition of the thick film materials. The cooling rate influences thermal shock stresses in the substrate and in the film. The thick film density is growing during the drying and firing processes (Fig. 1.10).

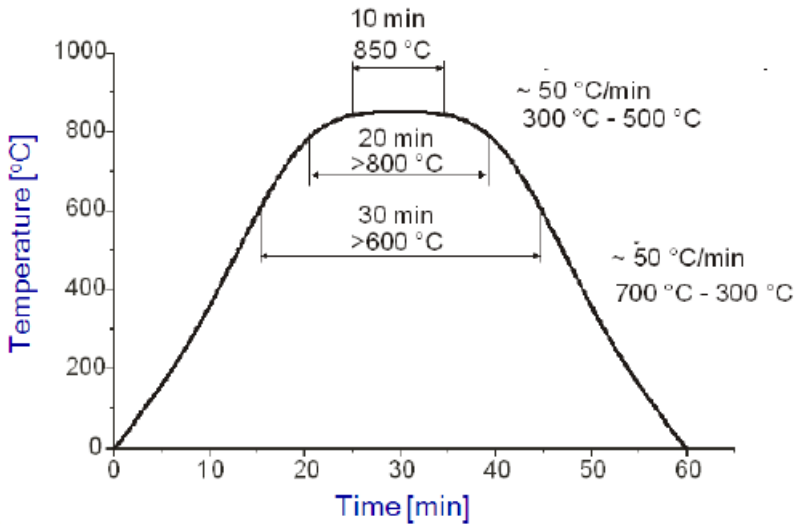


Fig. 1.9. Firing profile

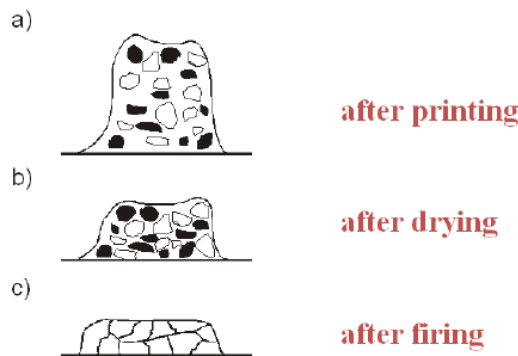


Fig. 1.10. Film thickness at various stages of the thick film process

Trimming process

Thick film resistors are required to meet sometimes tolerances of $\pm 0.1\%$. Because of the complex nature of the resistor they cannot be fired with the required tolerance. Very often the tolerance after firing is equal to $\pm 20\%$. Therefore, the resistors are trimmed to the target value by removing a part of the resistor film with a laser. The film absorbs the light, which causes it to heat rapidly and vaporise. Decreasing the effective width of the resistor increases the resistance value (Fig. 1.11). A neodymium-doped yttrium aluminium garnet (Nd:YAG) laser operating at 1064 nm wavelength is typically used. The laser parameters (Q-rate, power, cut speed) must be experimentally determined. The laser trims can be classified into four major types of cut: plunge, double plunge, L and serpentine (Fig. 1.12).

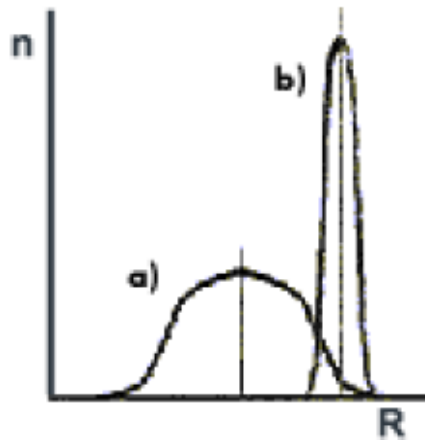


Fig. 1.11. Resistance distribution a) after firing, b) after trimming

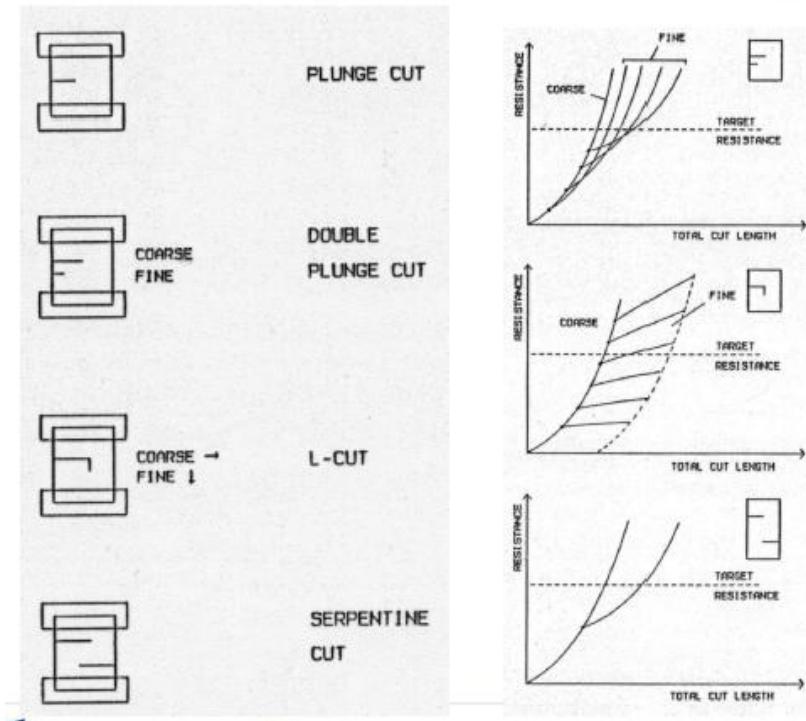


Fig. 1.12. Type of laser trim cuts [9]

Assembling and packaging

Various assembly technologies are used for the electro-mechanical attachment of discrete components to the substrate. The attachment can be realised by soldering or wire bonding methods. Moreover, polymer adhesives can be used for the attachment. Various assembling methods are shown in Fig. 1.13 and Fig. 1.14.

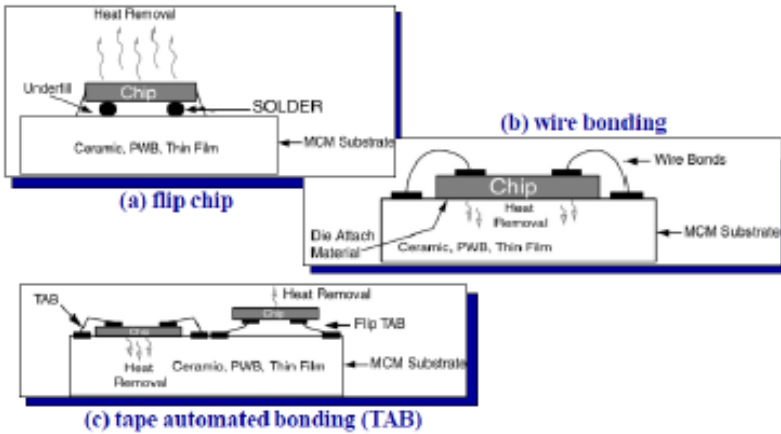


Fig. 1.13. Various assembling methods [10]

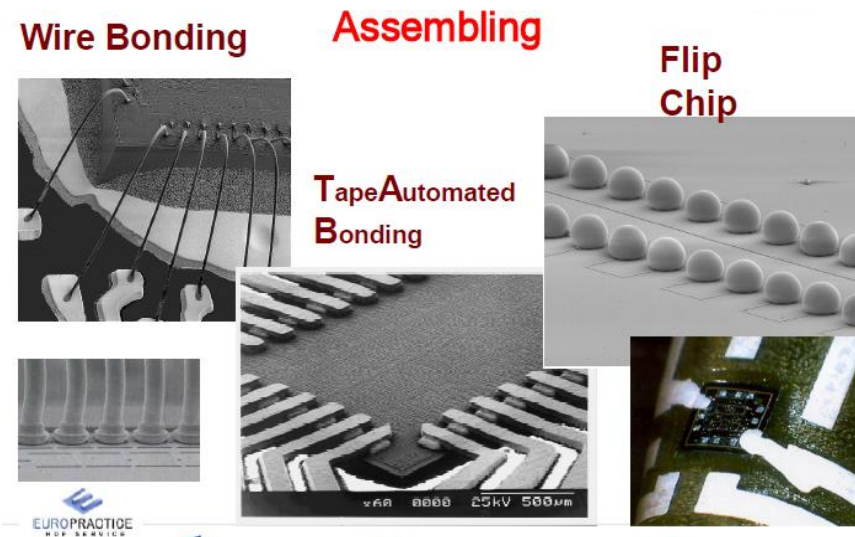


Fig. 1.14. Various assembling methods [Europractice EU Project]

Proper operating conditions can be maintained by encasing the thick film circuit in a protective package. A significant performance improvement can be achieved by optimising the electronic package. The device requires the electronic package that can match its performance in electrical, mechanical

and thermal aspects. The packaging of the device or microsystem should ensure the following conditions: proper operating temperature, protection from humidity and contaminants, mechanical support, good thermal management [10,11]. Various packaging levels are presented in Fig. 1.15.

Packaging Hierarchy

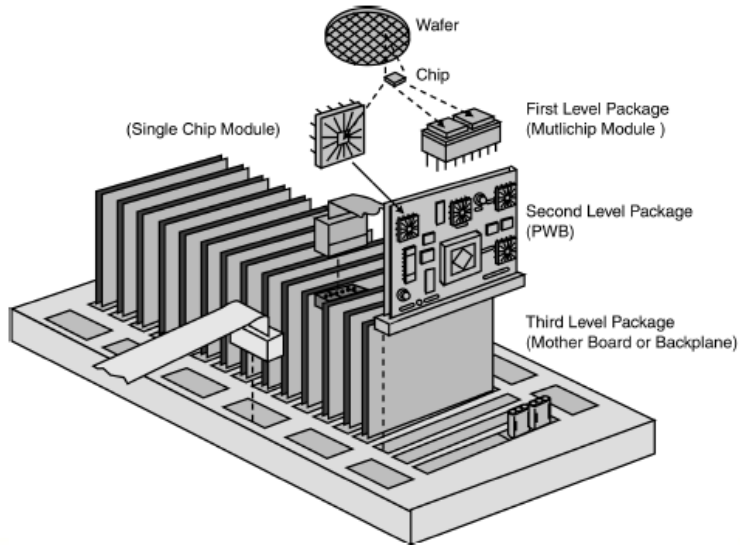


Fig. 1.15. Electronics packaging levels [10]

References

- [1] P.E. Garrou, I. Turlik, Multichip Module technology handbook, McGraw-Hill, New York, 1998.
- [2] L.J. Golonka, Zastosowanie ceramiki LTCC w mikroelektronice, Oficyna Wydawnicza Politechniki Wroclawskiej, Wroclaw 2001.
- [3] L.J. Golonka, Application of thick films in LTCC technology, Informacje MIDEM, vol. 29 (4), 169-175 (1999).

- [4] L.J. Golonka, A. Dziedzic, J. Kita, T. Zawada, LTCC in microsystems application, Informacje MIDEM, 4, 272-279 (2002).
- [5] L.J. Golonka, Low Temperature Co-fired Ceramic (LTCC) technology in microelectronics, Proc. Symp. Processing of Electroceramics, Bled (Slovenia), 313-329 (2003).
- [6] L.J. Golonka, New application of LTCC technology, Proc. 28th Int. Spring Sem. on Electronics Technology, Wiener Neustadt (Austria), 148-152 (2005).
- [7] J.E. Sergent, C.A. Harper, Hybrid microelectronics handbook, McGraw-Hill, New York, 1995.
- [8] B. Dziurdzia, PhD dissertation, AGH Kraków, 1998.
- [9] Instruction of PbTechnic laser.
- [10] R.R. Tummala, Fundamentals of microsystems packaging, McGraw-Hill, New York, 2001.
- [11] R.R. Tummala, M. Swaminathan, Introduction to System-on-Package (SOP), McGraw-Hill, New York, 2008.

Chapter 2

LTCC (Low Temperature Cofired Ceramics) materials and processing

2.1. Introduction

The Low Temperature Cofired Ceramic (LTCC) technology started at eighties of the last century as one of the technologies used for production of Multichip Modules (MCM). Multilayer MCM substrate is capable of supporting several chips in one package [1]. At the beginning, the technology was mostly used for production of high volume microwave devices. Recently, the LTCC is applied to the production of sensors, actuators, microreactors, microsystems, MEMS and MOEMS packages [2-7]. The LTCC module exhibits very good electrical and mechanical properties, high reliability and stability as well as possibility of making three-dimensional (3D) integrated microstructures. The technology is well established both for low volume, high performance applications (military, space) and high volume low cost applications (wireless communication, car industry). A great advantage of LTCC technology is the low temperature of cofiring (in comparison with standard ceramic processes). It enables the use of typical thick film materials.

2.2. Multichip Module (MCM)

Multichip Module technology is the most efficient packaging technology. It has the features that enable size reduction and higher speed performance to be obtained by eliminating individual packages and their parasitics. The semiconductor devices are attached to the MCM substrate by using various interconnection methods such as wire bonding, tape automated bonding or flip chip [1]. Depending on the method of fabrication, MCMs have been divided into three basic groups, shown in Fig. 2.1:

- MCM-C are built using either multilayer cofired ceramic substrates or thick film interconnection technology on ceramic substrate,

- MCM-D have interconnection structure built by deposition of thin film metals and dielectric materials over silicon, diamond, ceramic or metal substrate,
- MCM-L have substrates built by using the most advanced PWB (Printing Wired Boards) technology

Examples of the MCM-D and MCM-C modules are presented in Fig. 2.2.

Ceramic technology (MCM-C) for multilayer modules can be divided into three major categories:

- Thick film multilayer process (TFM),
- High temperature cofired alumina processes (HTCC),
- Low temperature cofired ceramic/glass based processes (LTCC).

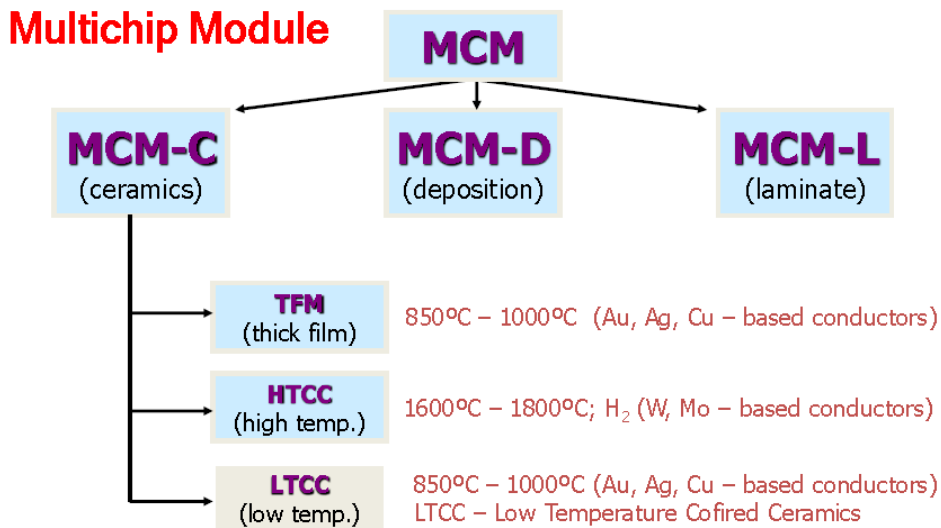


Fig. 2.1. Various Multichip Modules

LTCC modules have a number of advantages over HTCC (High Temperature Co-fired Ceramics) structures used before. The cofiring process takes place at lower temperature (LTCC at 850⁰C; HTCC at 1600⁰C÷1800⁰C) and therefore well established thick film materials and processing can be adopted to this technology. Metals with higher conductivity like gold, silver

or copper replace tungsten or molybdenum used in HTCC modules. Two basic materials are used in the LTCC tape fabrication – alumina filled glasses and glass-ceramics. The basic LTCC ceramic tape can be modified to produce dielectric materials with different electrical and physical properties. The coefficient of thermal expansion can be adopted to match alumina, gallium arsenide, or silicon. Standard thick film conductor, resistor and capacitor materials are used in LTCC circuits as buried (2D or 3D) or surface components. Lower mechanical strength and thermal conductivity are the main disadvantages of LTCC, in comparison with HTCC. The advantages of the LTCC technology in comparison with other MCM-C techniques are presented in Fig. 2.3.

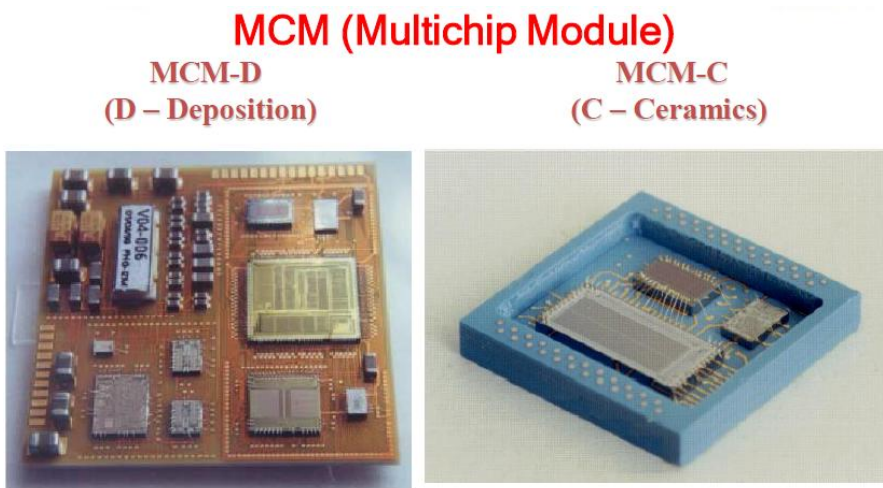


Fig. 2.2. Examples of MCM-D and MCM-C (LTCC) modules

2.3. LTCC manufacturing process

The LTCC multilayer structure is presented in Fig. 2.4. The module consists of dielectric tapes, connecting vias, external and internal conductors and passive components (resistors, capacitors, inductors). The components are made by a standard screen printing method. Thick or thin film components can be made on the top and bottom surfaces of the fired module. Additional

circuits and elements are added on the top and the bottom of the structure using various assembling methods. Moreover, the module can integrate sensors, actuators, channels, optoelectronic components, heating and cooling systems.

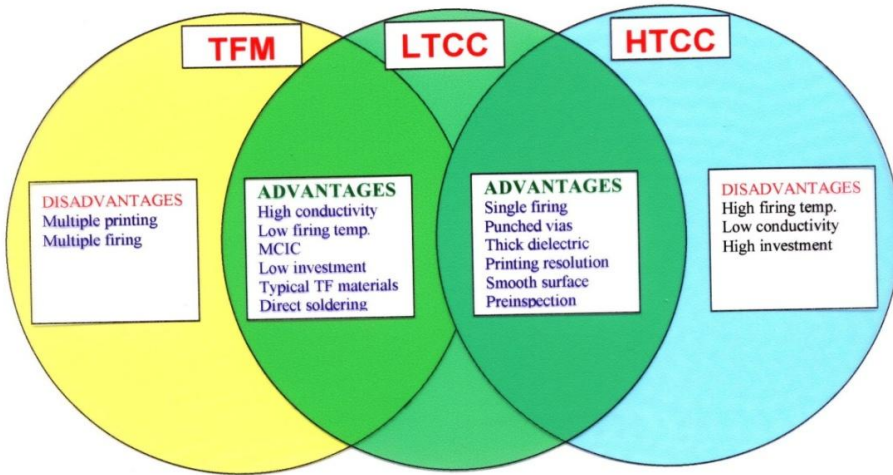
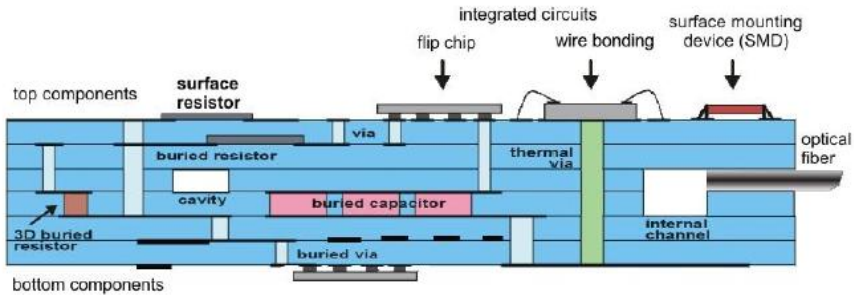


Fig. 2.3. Advantages of LTCC technology



- conductive paths and vias
- sensors and actuators
- channels (gas, fluid)
- electronic components
- optoelectronic components
- heating and cooling system

Fig. 2.4. Cross-section of a LTCC module (author: T. Zawada)

The conductors and passive components are printed by a standard screen printing method. After printing the cavities are made using automatic punch or laser. The finished sheets are stacked on a laminating plate and laminated in an uniaxial or isostatic laminator. The typical laminating parameters are 200 atm at 70°C for 10 minutes. After the lamination process the structures are cofired in two steps (Fig. 2.7). The first step, typically at around 500°C is the binder burnout step. The second, at 850°C, makes the ceramic material densify. The firing process is carried out in one programmable oven or in two separate ovens. The processes which occur during the cofiring process are described in [7,8]. The second firing step can be made in an ordinary thick film furnace. The fired parts usually shrink by 12% in the x- and y- directions and by about 17% in the z-direction. After cofiring the thick film or thin films components can be made on the top and bottom surfaces and additional active or passive elements can be added using various assembling methods. Thin film deposition process is a very expensive one, and the surface of the fired tape must be extremely smooth for good adhesion [9]. In the end the structures are singulated using dicing saw, ultrasonic cutting or laser cutting.

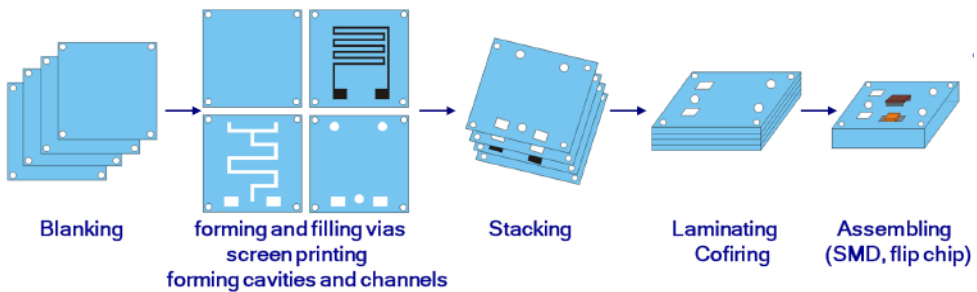


Fig. 2.5. LTCC process flow

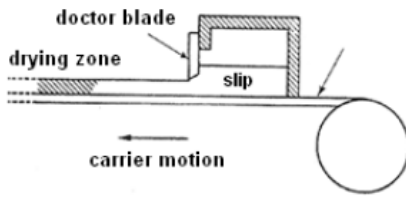


Fig. 2.6. Tape casting process

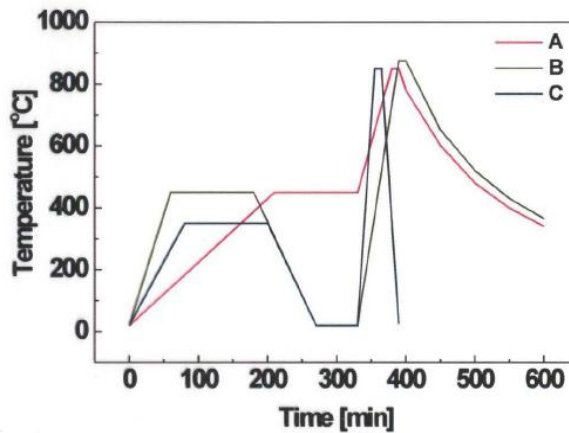


Fig. 2.7. Cofiring profile

2.4. Properties of cofired LTCC module

LTCC materials are based either on crystallizable glass [10,11] or a mixture of glass ($\text{CaO-B}_2\text{O}_3\text{-SiO}_2, \dots$) and ceramics, for example, alumina, silica or cordierite ($\text{Mg}_2\text{Al}_4\text{Si}_5\text{O}_{18}$) [12,13]. Typical properties of LTCC materials are presented in Table 2.1.

Shrinkage variations and poor thermal conductivity are the main limitations of LTCC technology. To eliminate shrinkage, Heraeus produces new tape HeraLockTM 2000 (Table 2.2).

Table 2.1. Typical properties of the LTCC materials

Property \ Tape	DuPont DP 951	DuPont DP 943	Ferro A6M	ESL 41110- 7-C	Heraeus CT 2000	Heraeus HL2000
Electrical						
Dielectric constant	7.85	7.5	5.9	4.3÷4.7	9.1	7.3
Dissipation factor	0.0045	0.001	0.002	0.004	0.002	0.0026
Breakdown voltage [V/25µm]	> 1000	> 1000	> 1000	> 1500	> 1000	> 800
Insulation resistance [Ωcm]	> 10 ¹²	> 10 ¹²	> 10 ¹²	> 10 ¹²	> 10 ¹³	> 10 ¹³
Dimensional						
Thickness – green [µm]	50, 112, 162, 250	125	125, 250	125	25, 50, 97, 127, 250	131
Thickness – fired [µm]	42, 95, 137, 212	112	92, 185	105	20, 40, 77, 102, 200	87÷94
Shrinkage x,y [%]	12.7±0.3	9.5±0.3	14.8±0.2	13±0.5	10.6±0.3	0.16÷0.24
Shrinkage z [%]	15.0±0.5	10.3±0.3	27±0.5	16±1	20.0±1.5	32
Camber [µm/mm]	< 2	< 2	< 2			< 1
Colour	blue	light blue	white	blue	light blue	light blue
Thermal						
CTE [ppm/K]	5.8	4.5	7	6.4	5.6	6.1
Thermal cond. [W/m·K]	3	4.4	2	2.5÷3	3	3
Mechanical						
Density [g/cm ³]	3.1	3.2	2.45	2.3	2.45	2.45
Flexural Strength [MPa]	320	230	> 170		310	> 200
Young's Modulus [GPa]	152		92			

The tape exhibits near-zero shrinkage (less than 0.2% with variation in the shrinkage less than 0.014%) in the x and y directions upon firing. The tape shows about 30% z -axis total shrinkage through firing [14-18]. HeraLock™ 2000 is a lead and cadmium free formulation with the properties appropriate for RF applications, automotive modules and general purpose packaging. For optoelectronic applications it is possible to make buried optical channels and fibers which remain undistorted after firing. Low x - y shrinkage also enables firing the tape with embedded passive devices such as ferrite transformers or chip capacitors. HL2000 exhibits a nearly dry (glass free) ceramic surface after firing without negative effect on conductor solderability.

LTCC's thermal conductivity of $2.0 \div 2.5$ W/mK is a limitation to the structures dissipating many watts of power. The most common method of increasing heat transfer in the z -axis is the application of thermal vias [19]. The thermal vias are the holes that are filled with silver or gold and are placed beneath the hot components. The thermal conductivity in the z - axis can be increased up to 120 W/mK or 70 W/mK in the case of Ag and Au, respectively [3].

Generations of LTCC modules

- | | |
|----------------|---|
| I generation | - conductive paths and vias |
| II generation | - conductive paths and vias
- passive components (MCIC) |
| III generation | - conductive paths and vias
- passive components (MCIC)
- sensors and actuators
- microsystems |

Advantages and disadvantages of LTCC technology

Advantages:

- very good electrical and mechanical properties,
- high stability,
- integration of various components,
- 3-dimensional (3D) structures,
- various applications,
- low cost.

Disadvantages:

- dimension,
- no active components,
- thermal conductivity.

Applications of LTCC technology:

- Multichip Modules
- microwave modules
- passive components
- sensors and actuators
- photonic modules
- smart packages
- fuel cells
- microreactors
- microsystems

2.5. Design of LTCC module

Some basic DuPont information on design rules are presented in Figs. 2.8 - 2.10 and Table 2.2 [20].

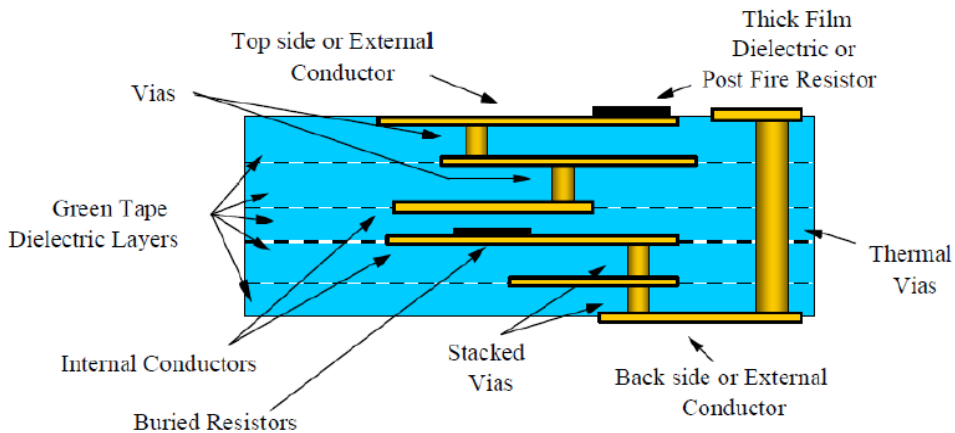


Fig. 2.8. Interconnect terminology [20]

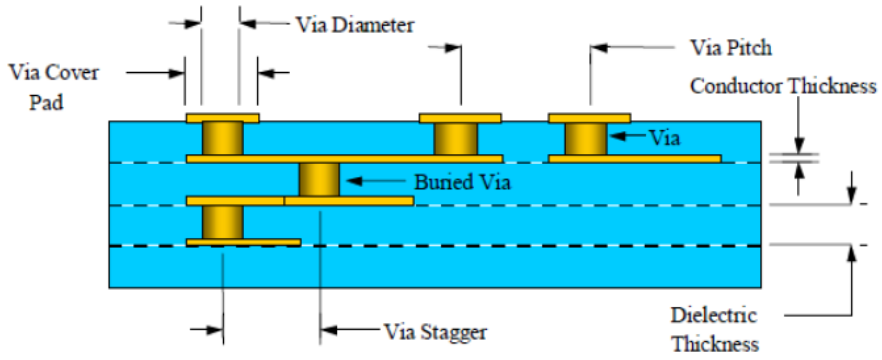


Fig. 2.9. Design of vias in LTCC module [20]

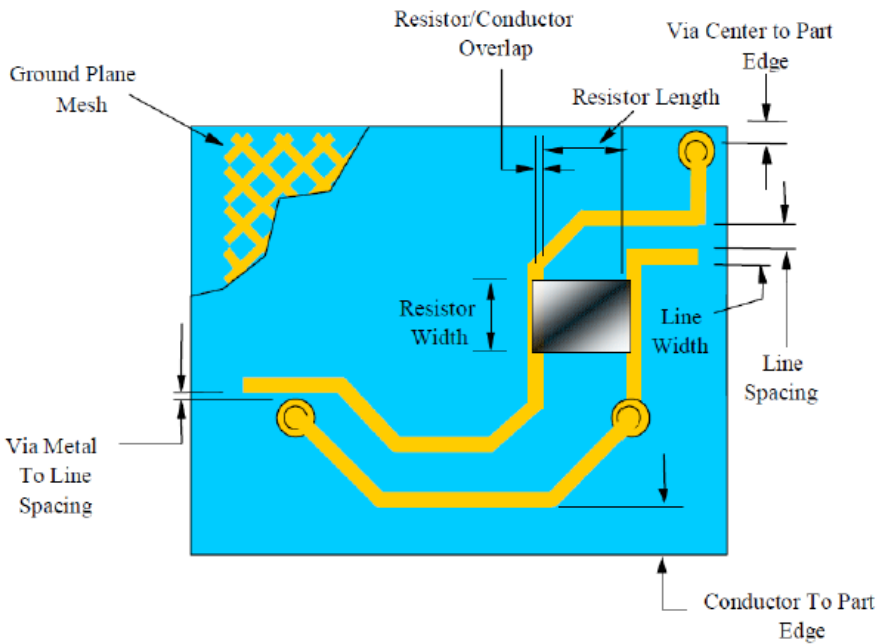


Fig. 2.10. Design of resistor and ground plane in the LTCC module [20]

Table 2.2.

Design parameters [20]

Feature	Typical	Demonstrated capability
# tape layers	20	100
Substrate x, y dimension (green) [mm]	200 x 200	450 x 450
Substrate thickness [mm]		
< 100 x 100	0.625	0.095
> 100 x 100	1.25	0.500
Lines / spaces		
Co-fired [μm]	125 / 125	50 / 50
Post fired [μm]	175 min	75
Via diameter	1:1 aspect ratio	< 1:1 aspect ratio
Via cover pad	2x via dia	1x via dia
Via pitch (min)	3x via dia	2x via dia
Via center to center	3x via dia	0x via dia
Via metal to line spacing [μm]	125 min	no pad
Via stagger (min)	2x via dia	no stagger
Thermal via diameter/pitch [μm]		
Option I	250 / 750	thermal slots
Option II	375 / 1000	-
Space from gnd/pwr/sig to part edge [μm]	250 min	0
Gnd/pwr plane coverage	70% gridded	100%
Gnd/pwr plane openings for feed throughs [mm]		
Thermal via	1.75	1.25
Signal via	1.25	0.625

Post fired resistors		
Length	750	250
Width	750	250
Overlap	125	125
Product	Thickness (green) [μm]	
951C2	50	
951PT, 951AT	114	
951P2, 951A2	165	
951PX, 951AX	254	
951RT	release tape 127	

2.6. Integrated passive components

The LTCC module can integrate electrical, optical, gas and fluidic networks with electronic measurement, control and signal conditioning circuits. Passive electronic components are embedded inside the LTCC module or made on the top. The properties of the passive components are presented below:

R Resistors - sheet resistance	surface $10 \Omega/\text{sq.}$ to $1 \text{ M}\Omega/\text{sq.}$ (tolerances of 1% to 2%) buried $10 \Omega/\text{sq.}$ to $100 \text{ k}\Omega/\text{sq.}$ (tolerances of 10% to 20%)
L Inductors - inductance	5 nH to 200 nH
C Capacitors – capacitance	$70 \text{ pF}/\text{cm}^2$ using standard tape (accuracy of 10%-20%) up to $25 \text{ nF}/\text{cm}^2$ using K700 dielectric

The resistor can be made on the top of the LTCC module as “postfired” (print on fired ceramics) or cofired (print on green tape). Embedded resistors are printed on green tapes and cofired with the module.

Various methods of resistor trimming are shown in Fig. 2.11. The resistors can be made as planar (2D) or 3-dimensional (3D) as presented in Fig. 2.12. The designs of capacitors and inductors are shown in Figs. 2.13 - 2.18. Microwave transmission lines in LTCC are presented in Fig. 2.19.

Type	Advantages	Disadvantages
Postfire	- like thick film	- surface demand
Cofire (surface)	- trimming possible	- influenced by cofiring - problems for many inks/sheet resistances
Cofire (buried)	- saving of surface, free for active components	- influenced by cofiring - limited available inks - limited performance - trimming by HVP

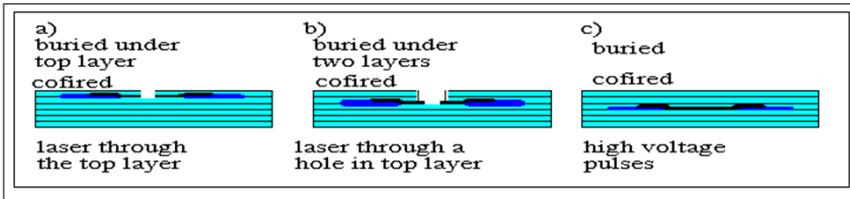
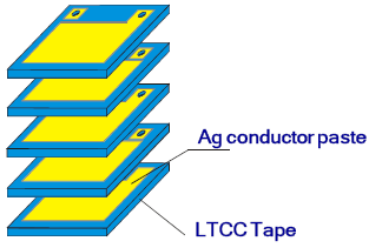


Fig. 2.11. Resistors in LTCC [21]



Fig. 2.12. Planar (2D) and 3-dimensional (3D) resistors

Capacitors



Multilayer inductor

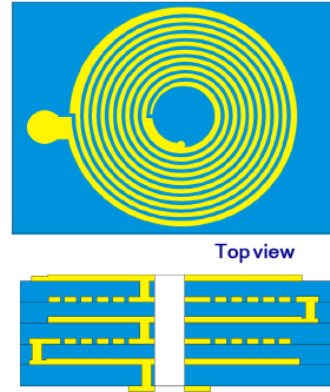


Fig. 2.13. Passive LTCC components (capacitor and inductor)

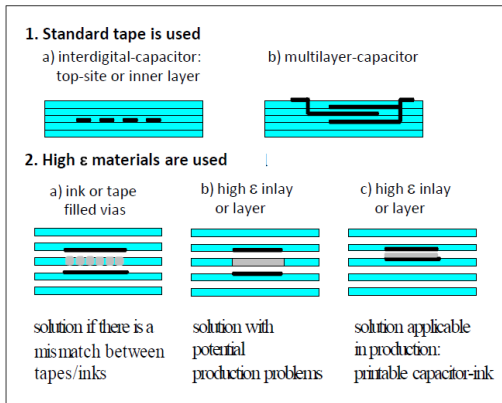


Fig. 2.14. Basic design of capacitors in LTCC [21]

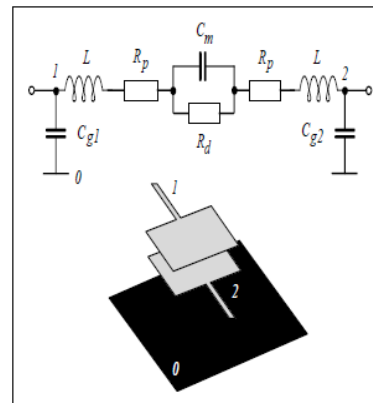


Fig. 2.15. Capacitor model for wide-band simulations [21]

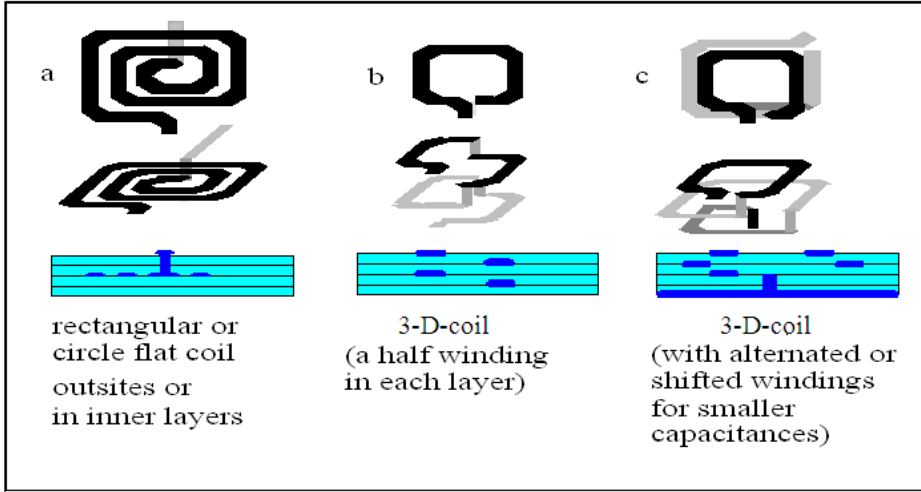


Fig. 2.16. Inductors in LTCC [21]

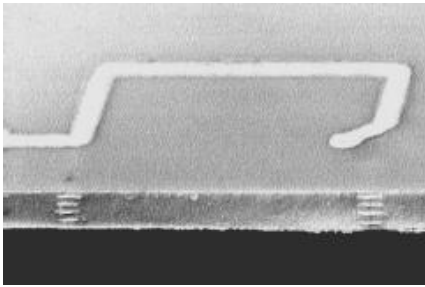


Fig. 2.17. Inductor design in LTCC and a photo of 4.5 turns buried coil [21]

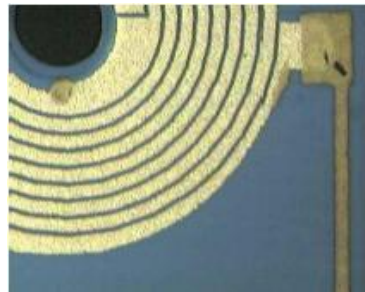


Fig. 2.18. Fine-line laser patterned top layer inductor spiral

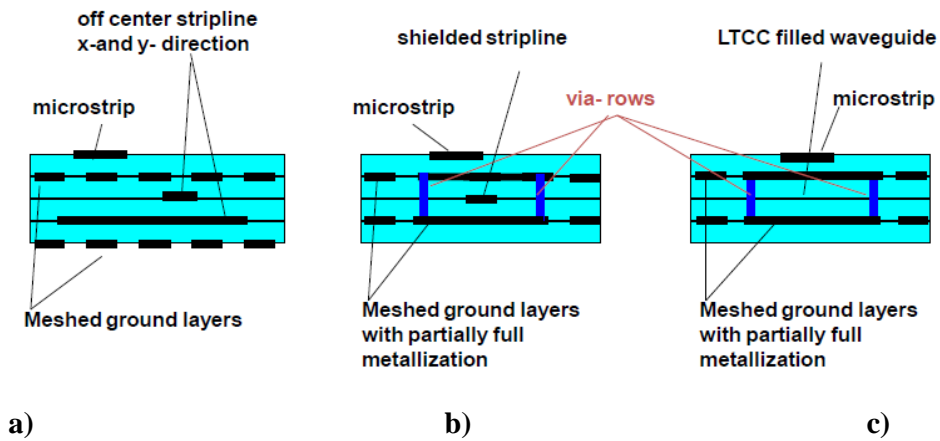
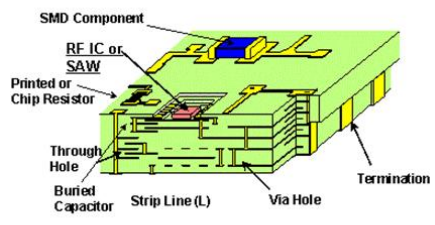


Fig. 2.19. Transmission lines in LTCC a) RF/high-speed-line, b) microwave-stripline, c) waveguide [21]

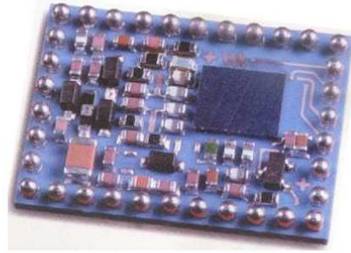
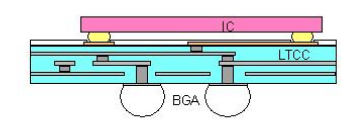
2.7. Microwave application

Microwave circuits were the first application of the LTCC technology. This area of LTCC products is still the biggest one. Various LTCC microwave devices are presented in Fig. 2.20.

- Mobile Phone, 0.9 – 1.9 GHz
- Bluetooth, 2.4 GHz
- Distance Radar, 70 GHz



www.murata.com



Bluetooth module on LTCC substrate (Ericsson)

Fig. 2.20. Microwave application of LTCC [22].

Murata is one of the biggest producers of LTCC microwave components. It has delivered over 950 million pieces of multilayer LTCC based components in the years 1989 - 2000 (LC filters, baluns, couplers, chip antennas, RF diode SW) [22]. The parameters of Murata components are presented below:

Substrate	length and width	max 10 mm
	thickness	1 – 2 mm
	layer thickness	50 μm (25, 100, 150 μm)
optional)		
Conductor	line width/space	100 μm / 100 μm
	via diameter	130 μm
Resistor	range	50 Ω - 100 k Ω
	tolerance	$\pm 5\%$
	TCR	± 300 ppm/K
Buried capacitor	C	1 pF/mm ² x layer
	tolerance	$\pm 5\%$
	TCC	80 \pm 20 ppm/K
Strip line inductance	impedance	100 Ω max
	spiral or radial	100 nH max

2.8. LTCC processes for microsystems

New materials for tape casting (high k, piezoelectric, piroelectric etc.) and special LTCC techniques are developed for the fabrication of LTCC microsystems. These techniques are connected with the following processes: fine line patterning, micromachining of LTCC tapes, lamination, making of cavities, holes and channels, bonding of LTCC tapes to other materials.

The LTCC techniques for ceramic microsystems are described in Chapter 7 (laser processing and mechanical machining of green ceramic tapes, hot embossing, jet vapor etching, photolithographic patterning, photoformable LTCC tapes, sacrificial volume material, low pressure lamination methods). LTCC can be joined to various materials by different techniques. These methods are described in Chapter 8.

References

- [1] P.E. Garrou, I. Turlik, Multichip Module technology handbook, McGraw-Hill, New York, 1998.
- [2] L.J. Golonka, Zastosowanie ceramiki LTCC w mikroelektronice, Oficyna Wydawnicza Politechniki Wroclawskiej, Wroclaw 2001.
- [3] L.J. Golonka, Application of thick films in LTCC technology, Informacje MIDEM, vol. 29 (4), 169-175 (1999).
- [4] L.J. Golonka, A. Dziedzic, J. Kita, T. Zawada, LTCC in microsystems application, Informacje MIDEM, 4, 272-279 (2002).
- [5] L.J. Golonka, Low Temperature Co-fired Ceramic (LTCC) Technology in microelectronics, Proc. Symp. Processing of Electroceramics, Bled (Slovenia), 313-329 (2003).
- [6] L.J. Golonka, New application of LTCC technology, Proc. 28th Int. Spring Sem. on Electronics Technology, Wiener Neustadt (Austria), 148-152 (2005).
- [7] C.B. DiAntonio, D.N. Bencoe, K.G. Ewsuk, "Characterization and control of Low Temperature Co-fire Ceramic (LTCC) sintering", *Proc. IMAPS Conf. on Ceramic Interconnect Technology*, Denver 2003, pp. 160-164.
- [8] T.J. Garino, "The co-sintering of LTCC materials", *Proc. IMAPS Conf. on Ceramic Interconnect Technology*, Denver 2003, pp. 171-176.
- [9] T. Pisarkiewicz, A. Sutor, W. Maziarz, H. Thust, T. Thelemann, "Thin film gas sensors on Low Temperature Cofired Ceramics", *Proc. European Microelectronics Packaging and Interconnection Symposium*, Prague, 2000, pp. 399-403.
- [10] A.A. Shapiro, D.F. Elwell, P.Imamura, M.L. McCartney, "Structure-property relationships in low-temperature cofired ceramic", *Proc. 1994 Int. Symp. on Micr ISHM-94, Boston*, 1994, pp. 306-311.

- [11] J.-H. Jean, C.-R. Chang, "Camber development during cofiring Ag-based low-dielectric-constant ceramic package", *J. Mater. Res.*, 12, (10), (1997), pp. 2743-2750.
- [12] R.E. Doty, J.J. Vajo, "A study of field-assisted silver migration in low temperature cofirable ceramic", *Proc. 1995 Int. Symp. on Micro ISHM-95*, Los Angeles, 1995, pp. 468-474.
- [13] C.-J. Ting, C.-S. Hsi, H.-J. Lu, "Interactions between ruthenium-based resistors and cordierite-glass substrates in low temperature co-fired ceramics", *J. Am. Ceram. Soc.*, 83, (12), (2000), pp. 2945-2953.
- [14] P. Barnwell, E. Amaya, F. Lautzenhiser, J. Wood, "HeraLock™ 2000 self-constrained LTCC tape – benefits and applications", *Proc. IMAPS Nordic Annual Conference*, Stockholm (Sweden), Sept. 2002, pp. 250-256.
- [15] M. Ehlert, B. Spenser, F. Lautzenhiser, E. Amaya, "Characterization of unrestrained zero shrink LTCC material for volume production of RF LTCC modules", *Proc. Int. Symp. on Microel. IMAPS USA*, Denver, Sept. 2002.
- [16] F. Lautzenhiser, E. Amaya, P. Barnwell, J. Wood, "Microwave module design with HeraLock™ HL2000 LTCC", *Proc. Int. Symp. on Microel. IMAPS USA*, Denver, Sept. 2002.
- [17] Q. Reynolds, P. Barnwell, "Self constrained LTCC technology – HeraLock", *Proc. MicroTech 2003*, London, Feb. 2003, pp. 3-38.
- [18] C. Modes, M. Neidert, F. Herbert, Q. Reynolds, F. Lautzenhiser, P. Barnwell, "A new constrained sintering LTCC technology for automotive electronic applications", *Proc. 14th European Microel. and Pack. Conf.*, Friedrichshafen (Germany), June 2003, pp. 118-122.
- [19] R. Kandukuri, Y. Liu, M. Zampino, W. Kinzy Jones, "High density thermal vias in Low Temperature Cofire Ceramic (LTCC)", *Proc. Int. Symp. on Microel. IMAPS USA*, Denver, Sept. 2002.
- [20] http://www2.dupont.com/MCM/en_US/assets/downloads/prodinfo/LTCC_DesignGuide.pdf
- [21] L.J. Golonka, H. Thust, Applications of LTCC ceramics in microwave, *Proc. 9th Int. Conf. MIXDES'2002*, Wroclaw (Poland), June 2002, pp. 101-110.
- [22] Chiang S-K, Radio frequency packaging, *Proc. IEMT/IMC*, Japan 2000, pp. 367-370.

Chapter 3

Sensors, actuators and microsystems - fundamentals and classification

3.1. Introduction

The transducer that converts a non-electrical quantity into an electrical signal is called a *sensor*, and the type of transducer that converts an electrical signal into a non-electrical quantity is called an *actuator*. A reduction in the size of a sensor leads to an increase in its applicability and a lower cost [1]. The microsensors are made using conventional thin film, thick film and LTCC technologies as well as silicon micromachining. This Chapter focuses on fundamental information on physical and chemical sensors as well as packaging, heating, cooling and energy source LTCC modules for microsystems.

3.2. Fundamentals

Sensor terminology

A sensor may be regarded as a system with an input $x(t)$ and output $y(t)$. The input signal can be of physical, chemical or biological nature. The output signal is electrical or optical (Fig. 3.1).

The input-output curve $y=f(x)$ is called *sensor conversion function* (Fig. 3.2). The ideal sensor has a linear output signal $y(t)$ which instantaneously follows the input signal $x(t)$, hence

$$y(t) = S x(t)$$

The slope S of the input-output curve has a constant value for a linear sensor and is called the *sensitivity*. In practice, the sensor conversion function is not linear and the sensitivity does not have a constant value (Fig. 3.3).

The sensor can not respond instantaneously to a change in the input signal but requires some time to reach its steady-state value (Fig. 3.4). The rise (and fall) of an output signal from a sensor is exponential with a characteristic time constant τ . The characteristic time constant τ can be related

to the physical properties of the system. Often the time taken for the sensor signal to reach 90% of its final value is referred to as the t_{90} time or sometimes the *response time*. It is desirable for the value of the t_{90} to be less than a few seconds.

Electrical sensor --

component which explicitly projects a physical or chemical signal x determined as a set of values X into an electrical signal y in a set of values Y

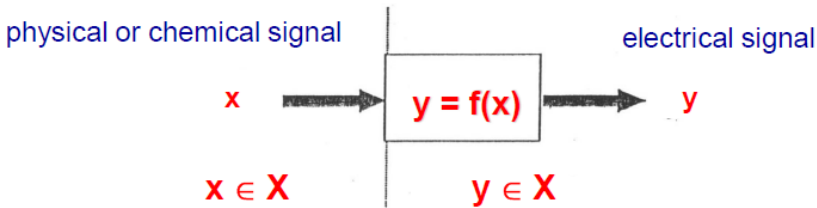


Fig. 3.1. Schematic representation of an electrical sensor

Sensor conversion function $y = f(x)$ should be continuous and monotonic in the whole definite range $x \in X$

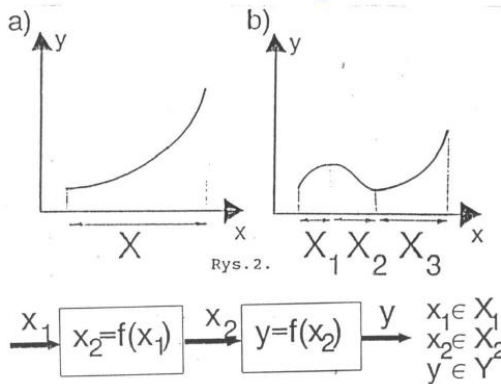


Fig. 3.2. Sensor conversion function (author: R. Jachowicz)

Sensitivity S_x
 $S_x = df/dx \quad x \in X$

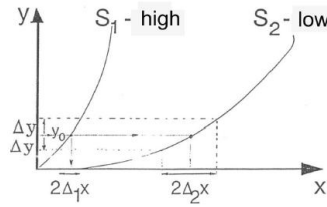


Fig. 3.3. Sensor sensitivity S_x (R. Jachowicz)

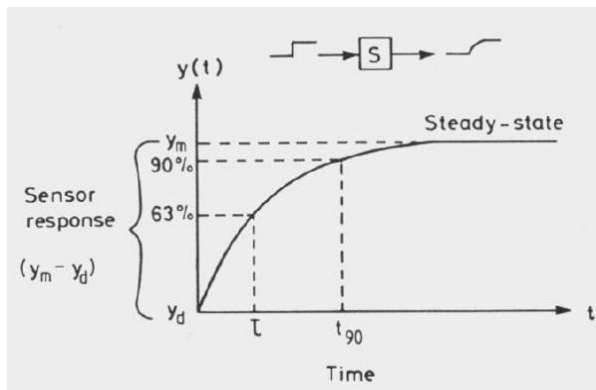


Fig. 3.4. Transient response of an ideal sensor system [1]

3.3. Physical and chemical sensors

The classification of the sensors can be made in different manner. It can be made on the base of the input signal, technology, signal processing, energy conversion or the effect applied in signal conversion [1,2].

Sensor classification

Input signal:

- physical
- chemical
- biological (biosensor)

Technology:

- conventional
- thick film, LTCC
- thin film
- semiconductor processing

Signal processing:

- electronic
- optic

Energy conversion:

- generation (self-exciting)
- parametric (modulating)

Effect applied in signal conversion:

- piezoelectric
- piezoresistive
- magnetoresistive
- pyroelectric
- thermoelectric
- polarymetric
-

Depending on the input signal the sensors are divided into two groups:
physical and chemical sensors:

Physical sensors

- temperature
- pressure
- force
- air flow
- heat flow
- radiation
- fluid level
- inclination
-

Chemical sensors

- humidity
- pH
- ion concentration
- gas concentration
- . . .

Very important parameters of the sensors are as follows:

- sensitivity
- selectivity
- stability (reproducibility)
- protection against environment
- system compatibility
- cost

Due to the possibility of very good electronic conditioning of the signal the sensitivity is not a big problem nowadays. Selectivity is still enormous problem for gas sensors. Stability and protection against environment does not pose any problems for physical sensors. We can protect them very well from the ambient atmosphere. However, it is a great problem for chemical sensors. In this case the sensitive material of the sensor has to be exposed to the environment. There is still a real problem for all sensors with a time drift and a calibration.

3.4. LTCC microsystems – general information

The Low Temperature Cofired Ceramic (LTCC) technology has been used at the beginning to produce a multilayer substrate for packaging integrated circuits and microwave devices. Recently, the LTCC was also applied to the production of sensors, actuators and microsystems because of

its very good electrical and mechanical properties, high reliability and stability as well as possibility of making three-dimensional (3D) integrated microstructures [3-5]. A great advantage of the LTCC technology is the low temperature of cofiring. It enables the use of the typical thick film materials. A great variety of these materials with different electrical properties are used to make a network of conductive paths in a package and to integrate other electronic components, sensors, actuators, microsystems, cooling and heating systems in one module. With the use of this technology it is also possible to produce MEMS and MOEMS packages.

LTCC sensors and actuators

- temperature sensor
- pressure sensor
- gas sensor
- heating system
- cooling system
- flow sensor
- proximity sensor
- microvalve
- micropump

LTCC technology advantages and disadvantages:

Advantages

- simple and inexpensive technology
- low cost and short time of a new design prototyping
- sensor integration
- resistance to environment and high temperature
- system integration (sensor, actuator, electronics)
- microsystems

Disadvantages

- dimension
- no active components
- ...

LTCC physical sensors:

- temperature
- gas and liquid flow
- pressure
- force
- proximity sensor
- heat flow
- radiation
- fluid level
- inclination
- ...

LTCC chemical and biochemical sensors

- humidity
- pH
- ion concentration
- gas concentration
- glucose
- urea
- ...

3.5. MEMS and MOEMS packaging

The LTCC technology can be used for making a “smart” packaging for MEMS and MOEMS microsystems [6-9]. The package not only protects mechanically the microsystem. The integrated electronics, cooling or heating system and sensors can be made inside the LTCC multilayer module. Moreover, electrical, optical, fluid and gas connections can be realized via a channel made inside the module. The LTCC packaging is presented in Fig. 3.5.

The acceleration chip sensor using the differential capacitive method, bonded to the LTCC package is shown in Fig. 3.6. The metallized LTCC wafer was bonded simultaneously with the Si-wafer and glass wafer. Joining of the metallized LTCC multilayer and silicon in a wafer process without any

intermediate bonding layers is possible. Further chip packaging includes joining the chip and LTCC; some functions will be performed in the chip, some in the LTCC. The overall manufacturing cost may decrease because of the reduced packaging size [9]. The photonic LTCC package is presented in Fig. 3.7.

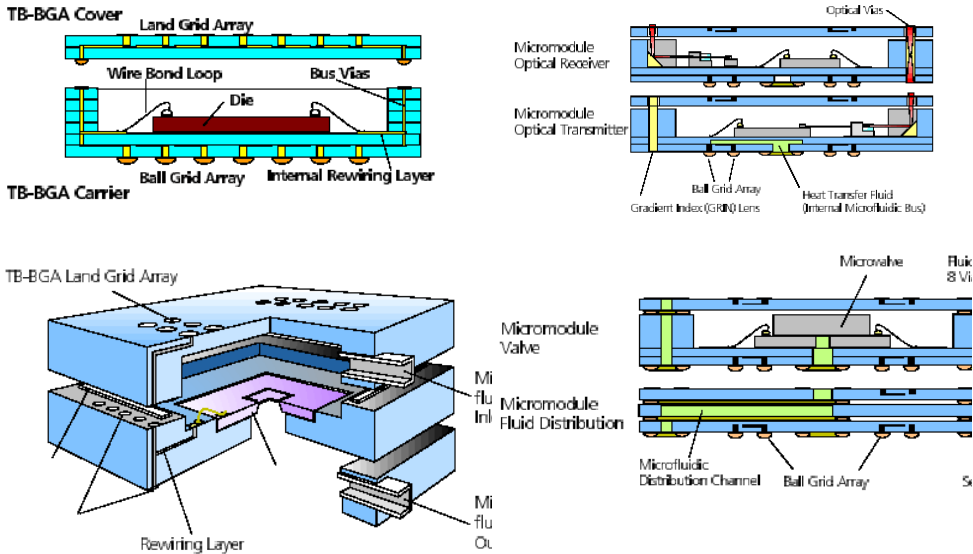


Fig. 3.5. The LTCC packaging for MEMS and MOEMS [6]

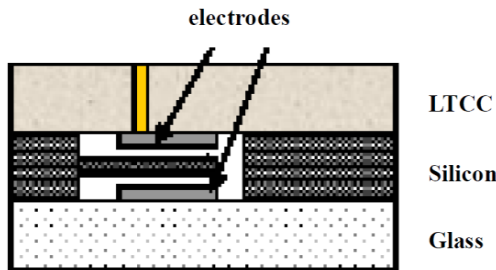
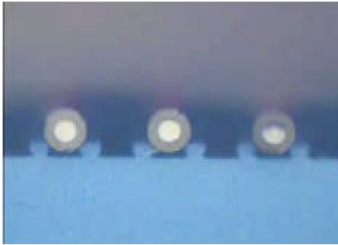


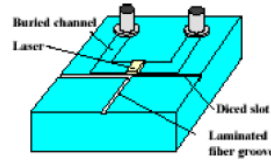
Fig. 3.6. Cross-section of an acceleration chip sensor and bonded layers (anodic bonding) [9]

The LTCC can be applied to photonic integration. A 3D LTCC structure with the grooves, cavities, holes, bumps and alignment fiducials for passive alignment of photonic devices was presented by Kautio and Karioja

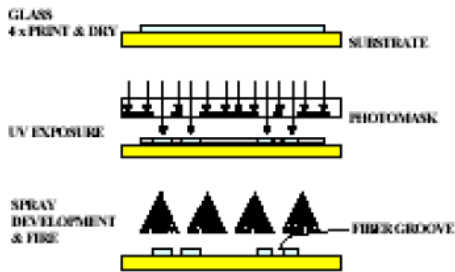
[10,11]. The thermal vias and liquid cooling channels were used for high power laser cooling (Fig. 3.7). Moreover, high speed integrated circuits as well as millimeter wave circuits can be integrated into the LTCC substrate.



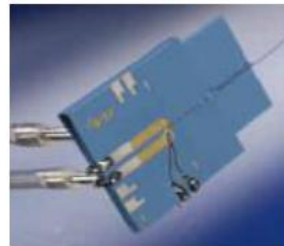
Photoimaged fiber grooves



Principle of demonstrator module



Processing of photoimaged alignment grooves



Demonstrator module

Fig. 3.7. Photonic package [10,11]

3.6. Heating and cooling systems

The LTCC module can integrate the heating and cooling systems [12-14]. The proper temperature of the sensor or ceramic microreactor is very important. For example, the sensitivity of the gas sensor depends strongly on the temperature and its distribution on the surface of the gas sensitive material. The LTCC gas heater is shown in Fig. 3.8 and the microfluidic

mixer with the heater and temperature sensor is presented in Fig. 3.9. The rate of the chemical reaction between two fluids in the ceramic microreactor is temperature sensitive. The special design of the heater allows one to get a uniform temperature distribution in the reaction area.

The cooling system is very important in the device with high density of power. The model LTCC module with a laser diode soldered to the package with the cooling system is shown in Fig. 3.10a. The temperature near the laser diode with and without the cooling system is presented in Fig. 3.10b.

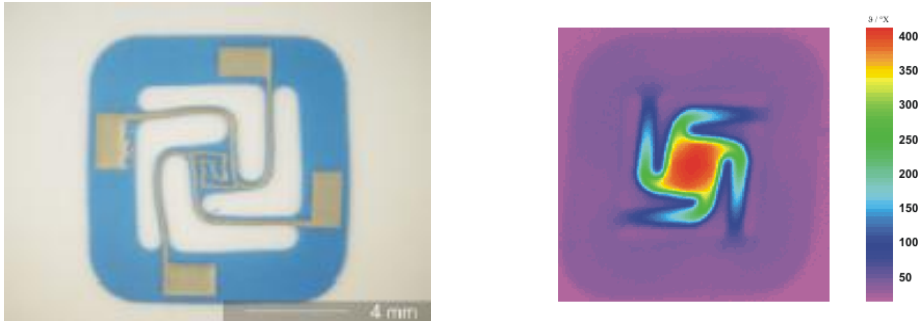


Fig. 3.8. Gas sensor hot-plate LTCC heater [14]

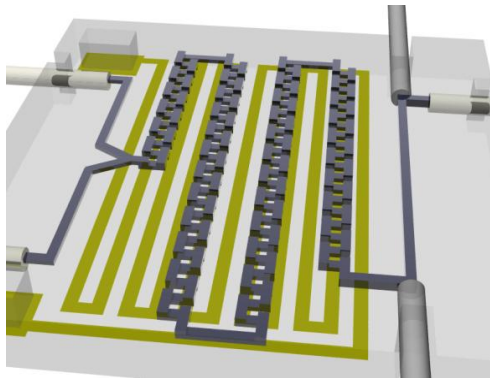


Fig. 3.9. LTCC microfluidic mixer with heater and temperature sensor [13]

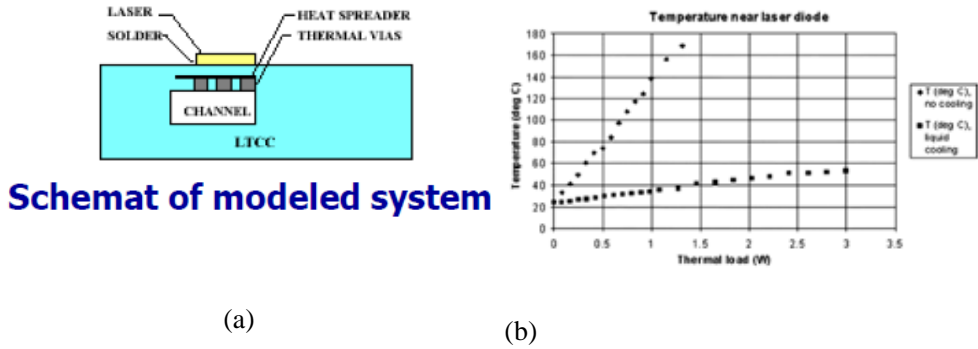


Fig. 3.10. a) Scheme of a model LTCC package with a laser diode and water cooling system [10], b) temperature near the laser diode measured with a thermistor (b) [15]

3.7. Energy source

The LTCC technology can be used successfully for producing integrated fuel cell system (sensors, mixer, channels, cavities, conditioning electronics) [16,17]. Fuel cells are an alternative way to conventional batteries for supplying electronic products (mobile phones, notebooks) with electrical energy. The miniature fuel cells have a high efficiency and a high power density due to the direct conversion of chemical to electrical energy. Fig. 3.11 shows the schematic configuration of the fuel cell system [16]. At the anode the oxidation of hydrogen takes place. The hydrogen ions move through the electrolyte to the cathode. The electrons are directed through an outer electrical circuit to the cathode (Fig. 3.12).

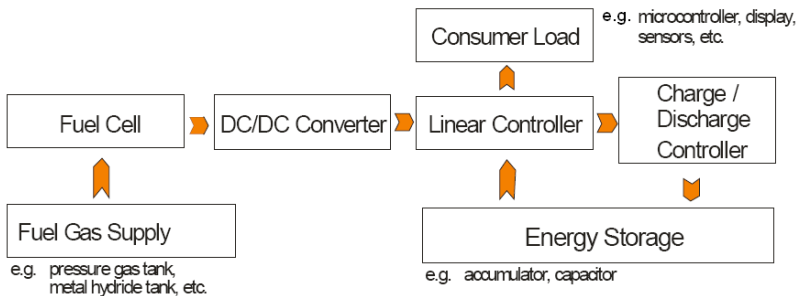


Fig. 3.11. Schematic configuration of the fuel cell system [16]

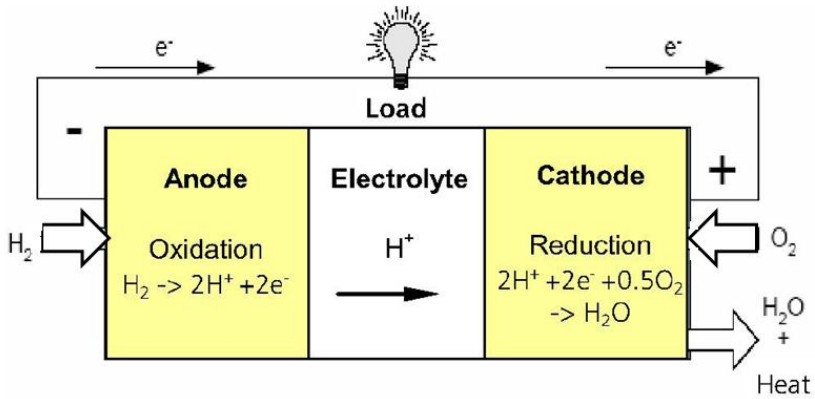
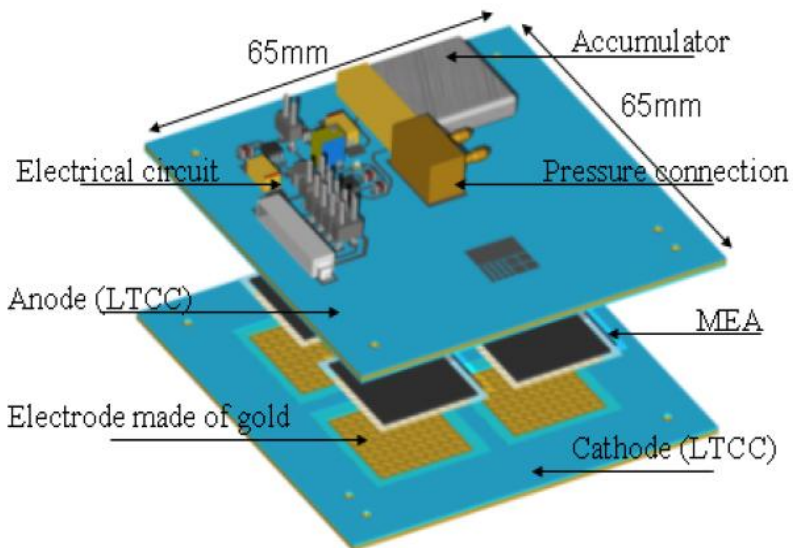


Fig. 3.12. Principle reaction in fuel cell [16]



PEM - Proton Exchange Membrane
 MEA - Membrane Electrode assembly
 GDL – Gas Diffusion Layer

Fig. 3.13. 3D picture of the Proton Exchange Membrane Fuel Cell (PEMFC) system [16]

The general structure of the LTCC fuel cell system is shown in Fig. 3.13. The whole device contains the fuel cell system with the charging circuit and the voltage converter plus a metal hydride and/or a hydrogen pressure tank. The properties of the four cell system in series connection are shown in Fig. 3.14. At the USB terminal the DC/DC converter transforms the varying output voltage into a constant 5 V DC. The main parameters of the fuel cell system are summarized in Table 3.1 [16].

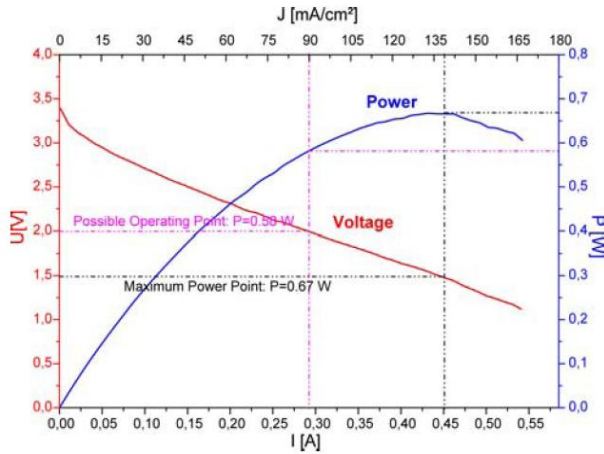


Fig. 3.14. U-I-P characteristics of PEMFC system [16]

Table. 3.1.

Characteristic points of the fuel cell system [16]

	Operating Point	Maximum Power Point
U[V]	2,0	1.5
I[A]	0.29	0.45
P[W]	0.58	0.68
J[mA/cm ²]	90	139

References

- [1] J.W. Gardner, *Microsensors*, Wiley, New York, 1995.
- [2] M. Prudenziati, *Thick film sensors*, Elsevier Science B. V., Amsterdam, 1994.
- [3] L.J. Golonka, A. Dziedzic, J. Kita, T. Zawada, LTCC in microsystems application, *Informacje MIDEM*, 4, 2002, 272-279.
- [4] L.J. Golonka, New application of LTCC technology, *Proc. 28th Int. Spring Seminar on Electronics Technology*, Wiener Neustadt (Austria), 2005, pp. 148-152.
- [5] L.J. Golonka, Technology and applications of Low Temperature Cofired Ceramic (LTCC) based sensors and microsystems, *Bulletin of the Polish Academy of Sciences*, Vol. 54 (2), 2006, pp. 223-233.
- [6] M. Schuenemann et al., MEMS modular packaging and interfaces, *Proc. 50th Electronic Com. & Technol. Conf.*, Las Vegas (USA), 2000, pp. 681-688.
- [7] L.J. Golonka, A. Dziedzic, J. Dziuban, J. Kita, T. Zawada, LTCC package for MEMS device, *Optoelectronic and Electronic Sensors V*, W. Kalita, Editor, *Proceedings of SPIE*, 5124, 2003, pp. 115-119.
- [8] E. Müller et al., Advanced LTCC-packaging for optical sensors, *Proc. 14th European Microel. and Pack. Conf.*, Friedrichshafen (Germany), 2003, pp. 19-24.
- [9] E. Müller et al., Development and processing of an anodic bondable LTCC tape, *Proc. 15th European IMAPS Conf. Brugge*, 2005, pp. 313-318
- [10] K. Kautio et al., Precision alignment and cooling structures for photonic packaging on LTCC, *Proc. IMAPS Cer. Interconnect Technology Conf.*, Denver 2004
- [11] P. Karioja et al., LTCC toolbox for photonic integration, *Proc. CICMT Conference*, Denver (USA) 2006.
- [12] J. Kita, Ph.D. Dissertation, Wrocław University of Technology, 2003.
- [13] T. Zawada, Ph.D. Dissertation, Wrocław University of Technology, 2004.
- [14] J. Kita, F. Rettig, R. Moos, K-H. Drúe, H. Thust, Hot-plate gas sensors – are ceramics better?, *Proc. 2005 IMAPS/AcerS 1st Int. Conf. and Exhib. on Ceramic Interconnect and Cer. Microsystem Technologies (CICMT)*, Baltimore (USA), 2005, pp. 343-348.

- [15] K. Keränen et al., Fiber pigtailed multimode laser module based on passive device alignment on an LTCC substrate. IEEE Tr Advanced Packaging 2006
- [16] A. Goldberg, U. Partsch, M. Stelter, A charging unit based on Micro-PEM-Fuel cells in LTCC technology, Proc. CICMT Conference, Denver 2007, pp. 338-343.
- [17] A. Michaelis, Application of ceramic technology for cost effective manufacturing of small fuel cell systems, Proc. CICMT Conference, Denver 2007, pp. 333-337

Chapter 4

LTCC and thick film physical sensors

4.1. Temperature sensors

Thermal sensors are used to measure various heat related quantities, such as temperature, heat flux and heat capacity. Temperature is perhaps the most important process parameter and about 40% of all solid-state sensors are thermal sensors [1]. Temperature is important in chemical processes where reaction-rate is usually exponentially temperature dependent according to the Arrhenius relationship. Temperature is a fundamental parameter in many processes and it may need to be measured, compensated for or even controlled in some manner. It is also exploited as a secondary sensing variable in non-thermal microsensors, for example a gas sensor or a flow sensor. The most important temperature sensors used in thick film and LTCC microsystems are thermocouples, Resistive Temperature Devices (RTD) and thermistors. There is a broad variety of temperature sensor applications:

- temperature measurements inside device,
- gas and fluid flow sensor,
- heater with temperature control sensors,
- heat flow sensor,
- ...

Thermocouples

An thermoelectric force is generated when a circuit consists of two different metals and the junctions are held at different temperatures. Fig. 4.1 shows the basic arrangement where a junction of two materials is held at a temperature T_A while a second reference junction is held at a temperature T_B . A thermoelectric potential ΔV is generated across the junctions. The device is referred to as a thermocouple and the thermoelectric effect is known as the Seebeck effect. The effect was discovered in 1821.

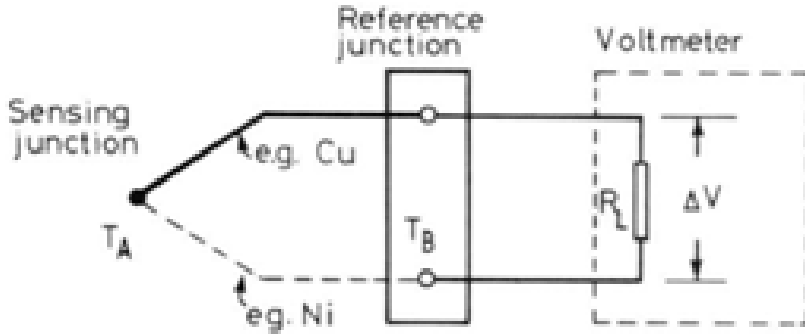


Fig. 4.1. Basic circuit of a thermocouple temperature sensor [1]

The Seebeck effect in metals (and alloys) is small. The thermoelectric e.m.f is normally associated with combined changes in the Fermi energy E_F and the diffusion potential. The Fermi level effect ΔV_F is given by [1]:

$$\Delta V_F = P_S \Delta T = \Delta E_F / q$$

where q is the electron charge. The Fermi level of a metal depends upon its temperature T and the density of states $N(E)$, and is given by

$$E_F(T) = E_F(0) - \pi^2 k^2 T^2 d(\ln N(E))/6dE$$

where $E_F(0)$ is the Fermi level of the metal at absolute zero and k is Boltzmann's constant.

$$P_A = \Delta V / \Delta T$$

$$P_S = P_B - P_A$$

$$\Delta V_T = (P_B - P_A) \Delta T$$

P_A, P_B – Seebeck coefficient of metal A and B

ΔV – thermoelectric potential (open circuit voltage)

ΔT – junction temperature (T_A) – reference temperature (T_B)

P_S – Seebeck coefficient measured by a thermocouple

ΔV_T – generated thermoelectric force (e.m.f)

E_F – Fermi level

$N(E)$ – density of states

Fig. 4.2 shows the typical thermoelectric e.m.f.'s E generated by standard wire thermocouples. Thick/thin film thermopiles made on the LTCC substrate is presented in Fig. 4.3 (a). They consist of a number of PdAg/TSG thermocouples deposited on DP 951 ceramics. The 0.25 mm wide PdAg tracks were screen printed and fired at 1123 K. Second arms were made by magnetron sputtering of tantalum-antimony-germanium alloy (TSG).

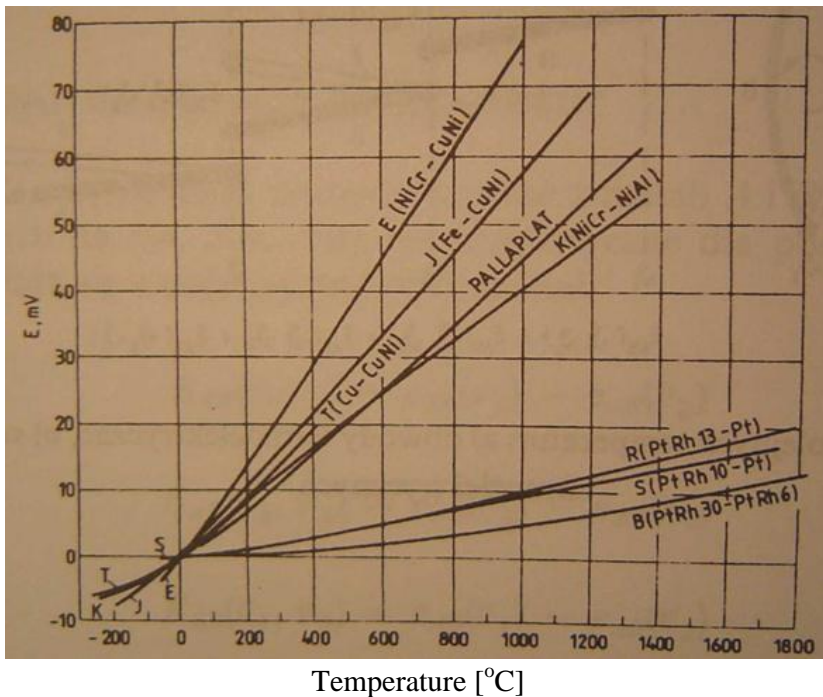
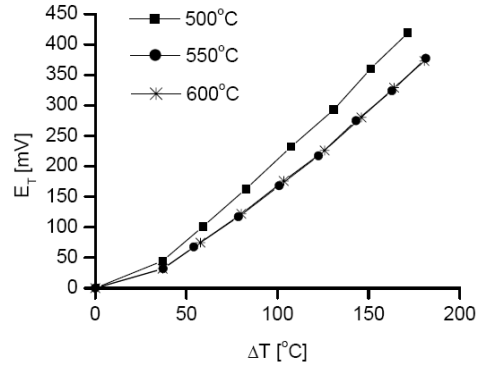
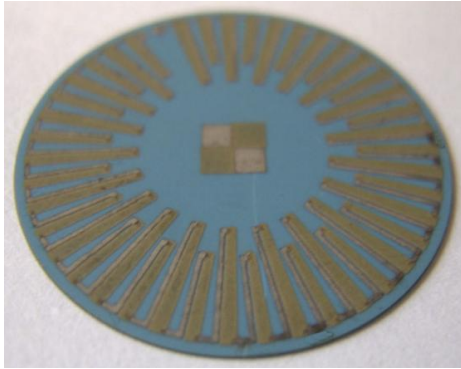


Fig. 4.2. Thermoelectric e.m.f.'s E generated by standard wire thermocouples [2]

RTD (Resistive Temperature Device) sensors

The resistive temperature detectors rely on the temperature dependence of metals and alloys. This phenomenon may be exploited in temperature sensors made of metal wires, thin and thick films. The RTD exhibits high positive temperature coefficients of resistance (TCR).



(a)

(b)

Fig. 4.3. Photograph of PdAg/TSG thermopile on LTCC (a) and its thermoelectric power versus temperature difference after burn-in process at 500°C, 550°C and 600°C (b) [3]

The largest TCR and the most reproducible one can be obtained with the materials free from impurities and defects [4]. Platinum thick film RTDs are mostly known. The TCR values of thick film resistive thermal detectors are lower and the resistivity higher than those observed in bulk and thin film materials. The properties of pure metals commonly used in RTDs are presented in Table 4.1 and Fig. 4.4. The dependence of sheet resistance of precious metal based thick films upon temperature is shown in Fig. 4.5. Among precious metal based RTDs Pt is the most interesting one, not only because of its high TCR, but also because it is a stable material which can be exposed to a variety of environments at high temperature without degradation. Nickel based RTD has been used for temperature sensors where the maximum temperature is lower than 150°C.

Table 4.1.

Characteristics of pure metals used in RTDs [4].

Metal	TCR (ppm/K)	Resistivity ($\mu\Omega$ cm)	TCE (ppm/K)	Melting point (°C)
Pt	3920	10.6	9.0	1774
Au	3900	2.3	14.1	1063
Ni	6810	6.84	13.3	1455
Cu	4300	1.67	17.0	1083

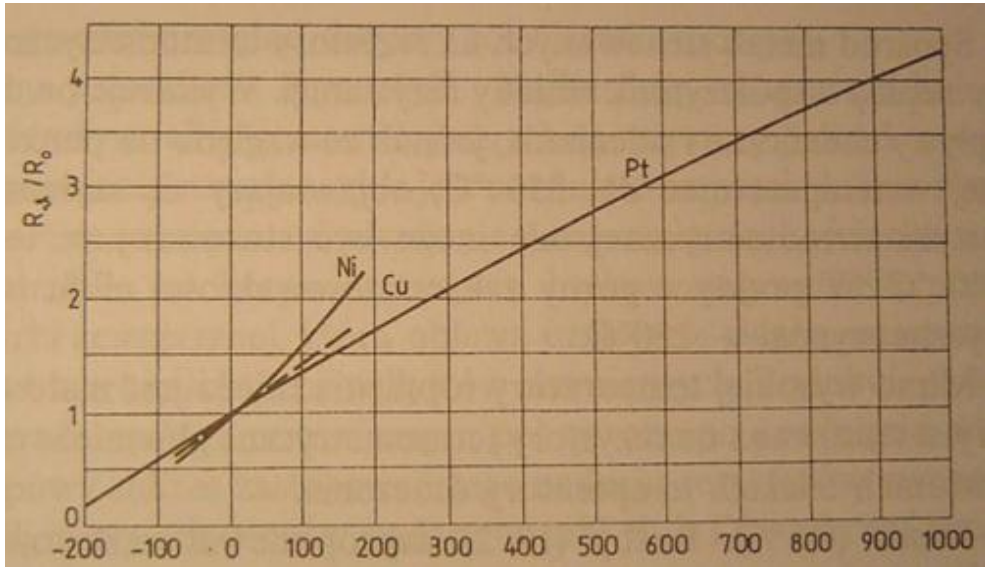


Fig. 4.4. Relative resistance changes of pure metals versus temperature [2]

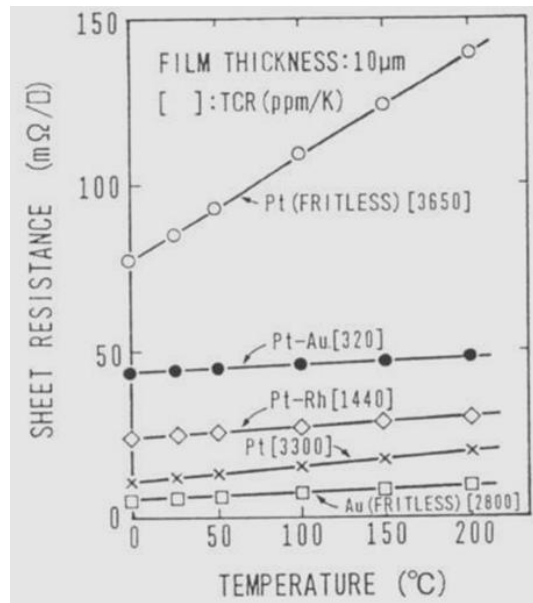


Fig. 4.5. Sheet resistance of precious metal based thick films [3]

The resistance dependence of Pt, PdAg and PtAu thick films RTDs buried in LTCC module upon temperature is shown in Fig. 4.6.

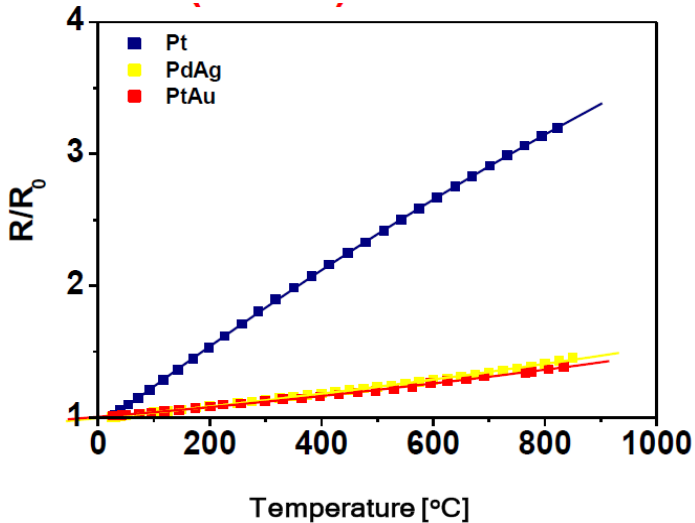


Fig. 4.6. Relative resistance changes versus temperature of RTD LTCC buried components: Pt (TCR = 2500 ppm/K), PdAg (TCR = 430 ppm/K), PtAu (TCR = 380 ppm/K) [5]

Thermistors

Thermistors (Fig. 4.7) are made from semiconducting ceramic materials (e.g. sulphides, selenides, oxides of Ni, Mn, Cu etc.). The resistivity of a typical thermistor is much higher than that of a metal thermoresistor. The TCR of NTC (Negative Temperature Coefficient) thermistor is negative and highly non-linear as shown in Fig. 4.8. The plot shows the material resistances relative to its ice-point resistance in order to normalize the values and compare them with platinum and nickel RTD [1]. The temperature characteristic of NTC thermistor can be described by equation:

$$R = A \exp (B/T)$$

where: A – constant
 B – thermistor constant

Some metal oxide materials possess a positive temperature coefficient of resistance. These PTC thermistors have very different current-voltage characteristics (Fig. 4.9).

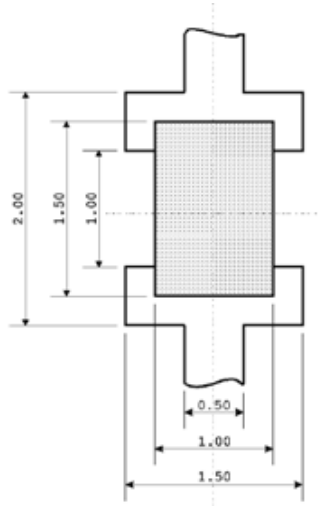


Fig. 4.7. Topology of single thermistor

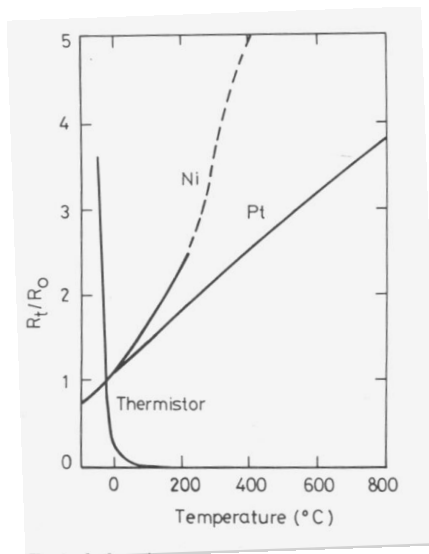


Fig. 4.8. Typical plot of resistance vs. temperature of a NTC thermistor and RTD elements (Ni and Pt) [1]

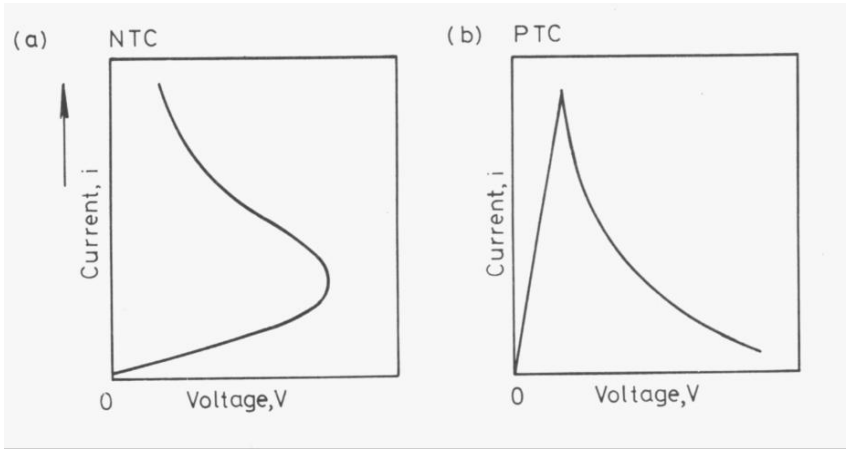


Fig. 4.9. Current-voltage characteristics of NTC and PTC thermistors [1]

The design of thick film thermistor determines the required values of the thermistor constant B and the resistance R . The temperature characteristic (constant B) is strictly related to the thermistor composition. The resistance depends on the resistivity of thermistor material and the thick film component design. The requirement of resistance can be met by an appropriate choice of the thermistor structure. It relies on three main configurations: planar, comb and sandwich (Fig. 4.10) [4]. For the same thermistor paste the planar type gives the highest resistance while the sandwich type the lowest one. The resistance R of the thermistor is related to the component design according to the following equations:

planar and comb types	$R = \rho L / (D W) = R_s L / W$	
sandwich type	$R = \rho D / S = R_s D^2 / S$	($D = L$)
	$R_s = \rho / D$	

where

- ρ - resistivity
- R_s - sheet resistance
- D - thickness
- W - electrode width
- L - distance between electrodes
- S - electrode area.

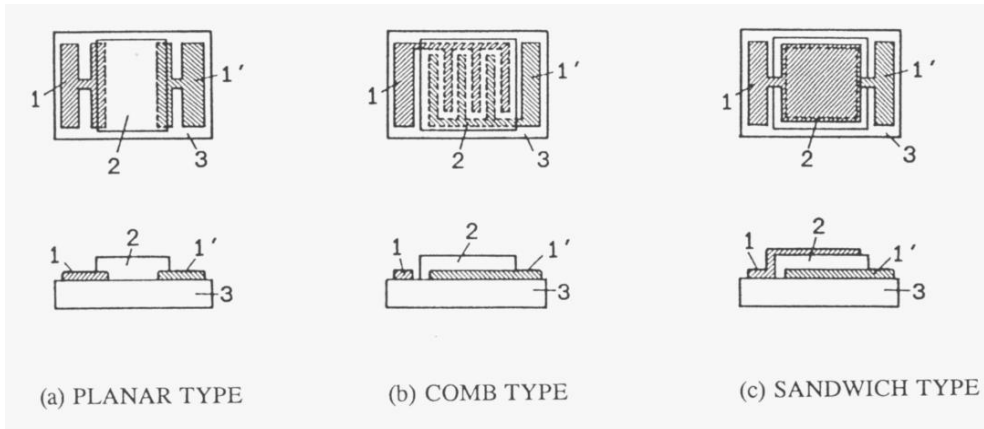


Fig. 4.10. Designs of thick film thermistors [4]

The properties of thick film thermistors manufactured by DuPont and ESL are presented in Tables 4.2 and 4.3, respectively.

Table 4.2.

Parameters of DuPont 5090D PTC thick film thermistors [6].

Typical PTC Thermistor Properties			
	5091D	5092D	5093D
Resistivity ^{1,2} (Ω /sq)	10	100	1000
Shipping Specification(%)	± 10	± 10	± 20
Temperature Coefficient of Resistance ³ (ppm/ $^{\circ}$ C)	3100 \pm 200	3000 \pm 200 (Hot) 3100 \pm 200 (Cold)	2750 \pm 250
Post Laser Trim Stability ⁴ (%)			
25 $^{\circ}$ C/1000 hours	<0.3	<0.2	<0.2
85%RH/85 $^{\circ}$ C/1000 hours	<0.2	<0.2	<0.2
150 $^{\circ}$ C/1000 hours	<0.3	<0.2	<0.2

¹ Terminations Ag/PD 7484. Substrate 90% alumina. Printing 200-mesh stainless steel screen (10 \pm μ m emulsion thickness) to a dried thickness of 25 \pm 2 μ m. Firing - recommended short firing profile to a peak temperature of 650 $^{\circ}$ C for 10 minutes.
² Resistor geometry for R, TCR, laser trim stability: 1.5 x 1.5 mm
³ TCR
 Cold TCR measured from -55 to +25 $^{\circ}$ C
 Hot TCR measured from +25 to +125 $^{\circ}$ C
⁴ Post Laser trim stability
 This data is based on tests of 1.5 x 1.5 mm resistor resistors trimmed to 1.5 x initial value with a single plunge out. All resistors were unencapsulated.

There are many applications of the temperature sensors, for example:

- heat flow sensors,
- gas and liquid flow sensors,
- heaters,

- temperature measurements inside a multilayer LTCC structure,
- solarimeters,
- measurements of laser power.

Some applications are described below.

Table 4.3.

Parameters of Electro-Science Laboratories PTC and NTC thick film thermistors [7].

PTC-2600 SERIES			
	<u>RESISTIVITY</u>	<u>HOT TCR, ppm/°C</u> (+25°C to +125°C)	<u>COLD TCR, ppm/°C</u> (-55°C to +25°C)
PTC-2650	5 Ω/sq.±10%	+4000±500	+4000±500
PTC-2611	10 Ω/sq.±10%	+4100±500	+4100±500

NTC-2100 SERIES			
Designation	Average Beta (β) -55°C to 125°C	Nominal Sheet Resistivity*	Resistance Range (Ω)**
NTC-2131	300	30	3 to 300
NTC-2112	725	100	10 to 1 k
NTC-2113	1700	1 k	100 to 10 k
NTC-2114	2125	10 k	1 k to 100 k
NTC-2115	2500	100 k	10 k to 1 M
NTC-2116	3100	1,000 k	100 k to 10 M

4.2. Flow sensors

The LTCC gas flow sensor is described by Gongora Rubio [8]. The basic sensor structure consists of a thick film resistive heater and two thermistors printed on a thermally isolated bridge in a cavity (Fig. 4.11). The sensor measures the temperature in the bridge using two thermistors. The temperature difference is related to the flow in the cavity. The thermistors are

screen-printed on the bridge together with the ruthenium-based resistor for the heater. Fig. 4.12 depicts various layers of the basic sensor schematically and Fig. 4.11 is a SEM micrograph of the device cross-section. Temperature difference vs. flow at different values of the heater current I_p , as a parameter is displayed in Fig. 4.13.

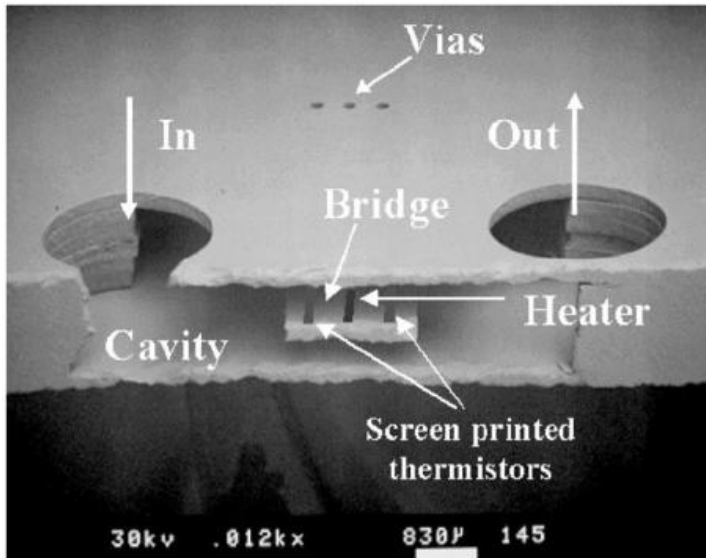


Fig. 4.11. Schematics: flow sensor layers and cross-section [8]

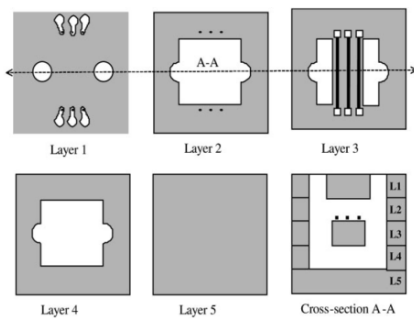


Fig. 4.12. Cross-section of a basic flow sensor [8]

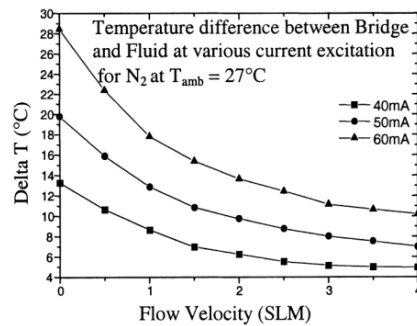


Fig. 4.13. Delta T vs. flow with parameter I_p [8]

A gas flow sensor made on the LTCC tube is described by Smetana [9]. The principle of work is similar to the case of Gongora Rubio flow sensor. The prototype of the calorimetric flow sensor and its temperature characteristics are shown in Fig. 4.14.

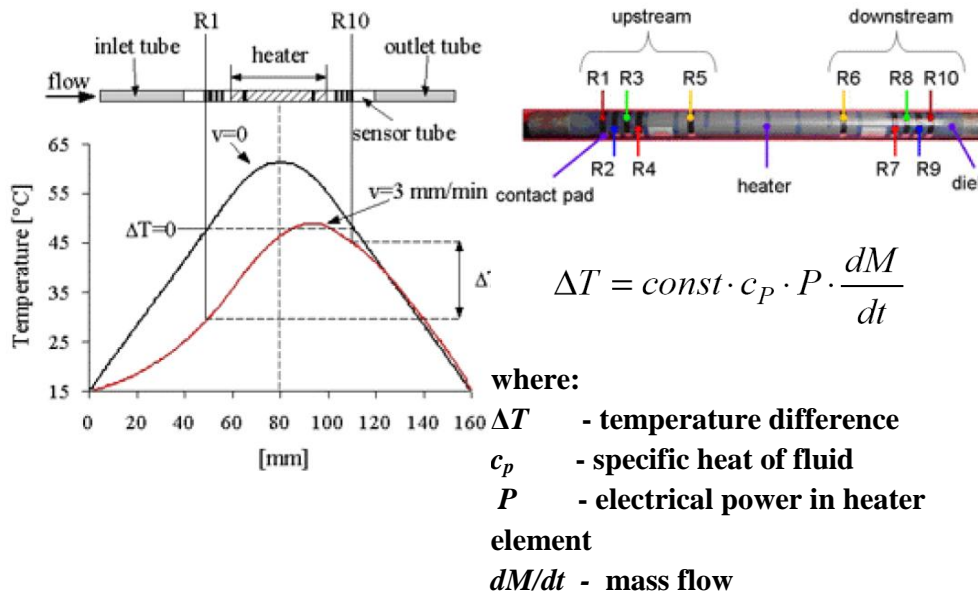


Fig. 4.14. Prototype of calorimetric flow sensor realized in thick film on tube technology [9]

Another construction of the LTCC gas flow detector is presented in Fig. 4.15 [10]. The detector consists of gas channel and a cavity with an axle and a turbine. The turbine and the axle are manufactured independently. The rotational speed of the moving turbine depends on the gas flow velocity. The speed is measured by the optical method. The gas flow can be calculated on the base of the frequency. The optical components are integrated with the LTCC module.

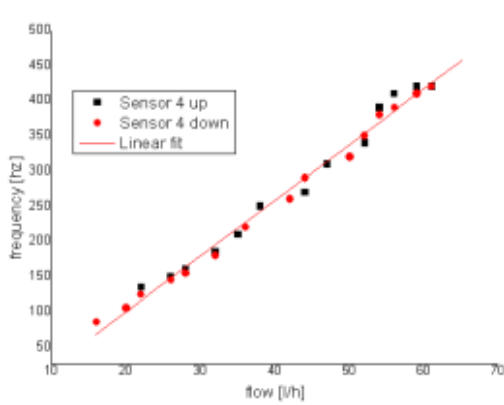


Fig. 4.15. LTCC gas flow detector

4.3. Pressure sensors

The first thick film pressure sensor presented in Fig. 4.16 was described in the 80-ties [11]. The piezoresistive effect in thick film resistors was utilised in the sensor.

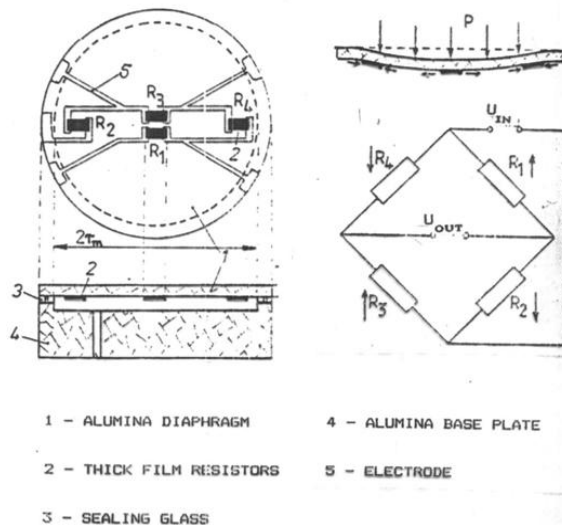


Fig. 4.16. Piezoresistive thick film pressure sensor [11]

The sensors were made on an alumina, which was the most common used substrate material in thick film technology. Due to the invention of Low Temperature Cofiring Ceramics (LTCC), the new possibilities appeared in the sensor's design and construction. The LTCC ceramics allows one to integrate both sensor and microelectronics transducer into one structure. The design of the LTCC pressure sensor is presented in [12].

The pressure sensor and the transducer are situated vertically, one over another. They form a 3D LTCC structure. The sensor consists of eight LTCC tapes (Fig. 4.17a). The three lowest tapes form the membrane. The thick film piezoresistors are made on the tape number 3. They are connected in a Wheatstone's bridge configuration. The central holes made in the tapes 4-6 determine the membrane diameter. Four vias are made in the tapes 4-8. They are filled with conduction ink. The vias provide the electric supply to the bridge input, and signal from the bridge output to the electronic transducer on the highest tape (Fig. 4.17b).

The pressure sensor was fabricated in LTCC DP951 tape with the thickness of 165 μm each (before cofiring process). The green tapes were cofired in the typical firing profile recommended by Du Pont for DP 951 tape.

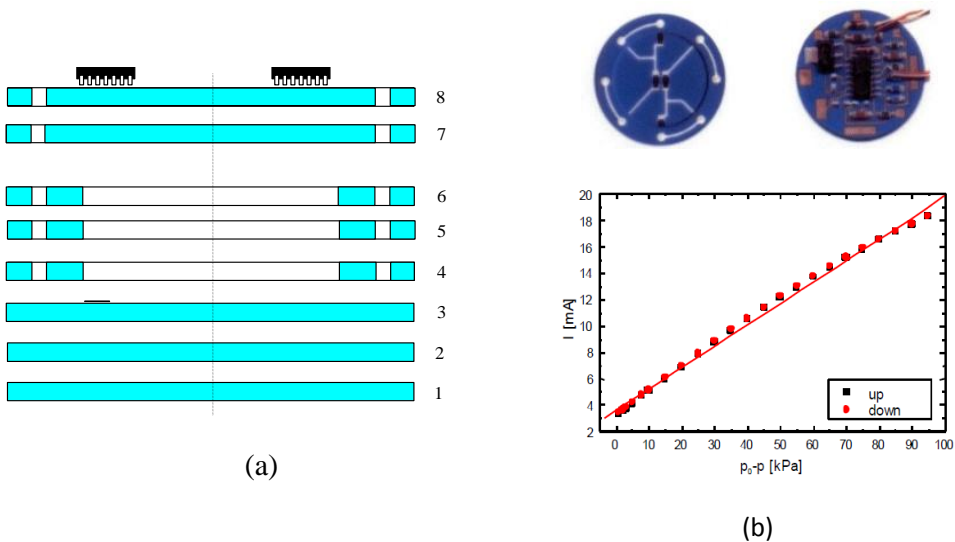


Fig. 4.17. Cross-section of 3D LTCC pressure sensor (a), output

characteristics of the pressure transducer (b) [12]

Another construction of the LTCC pressure sensor is presented in Fig. 4.18. The principle of work is the same as described before (piezoresistive effect). The sensor sensitivity depends on the diaphragm thickness (Fig. 4.19).

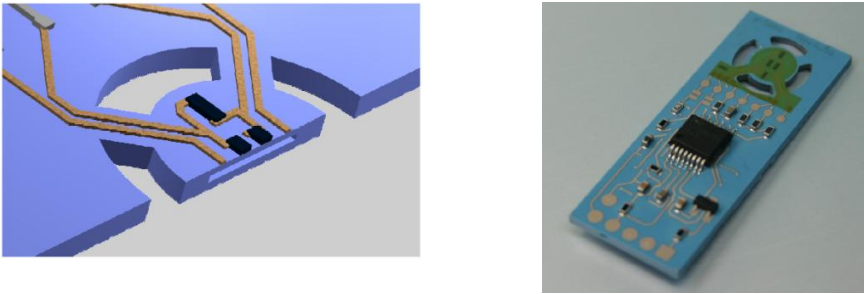


Fig. 4.18. LTCC-based pressure sensor (finally assembled) [13]

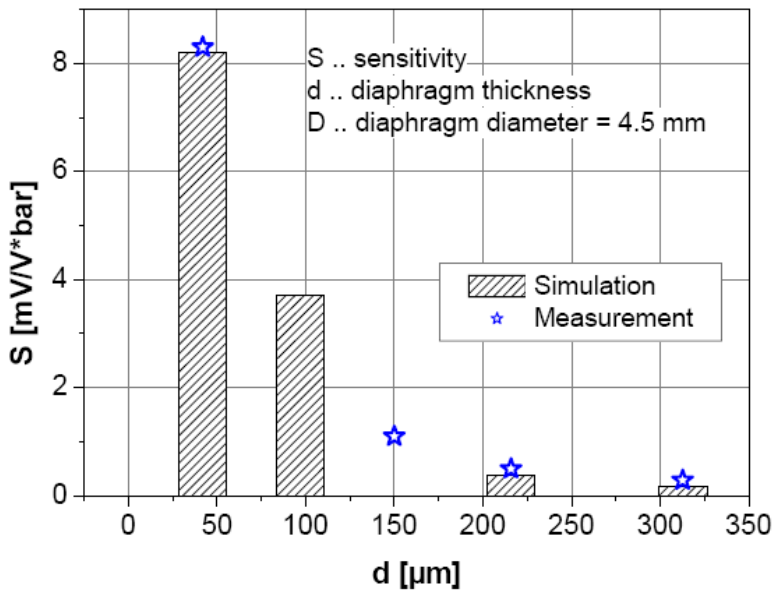


Fig. 4.19. Sensor sensitivity (calculated vs. measured values) depending on the diaphragm thickness [13]

The thick film pressure sensor can also work on the base of piezoelectric effect or changes of /in capacitance. Such sensors were presented by Belavic [14]. The cross-sections of the sensors are shown in Fig. 4.20 and Fig. 4.21, respectively.

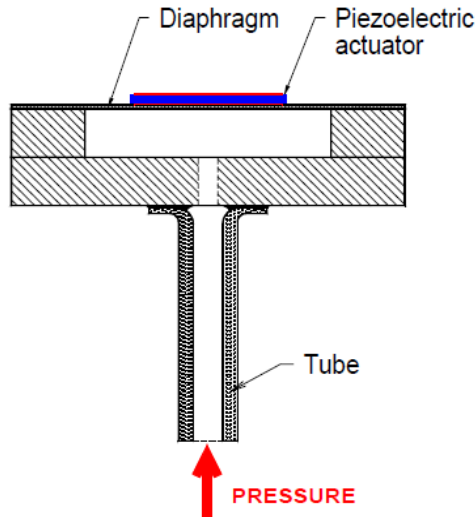


Fig. 4.20. Cross-section of the piezoelectric resonant pressure sensor (schematic - not to scale) [14]

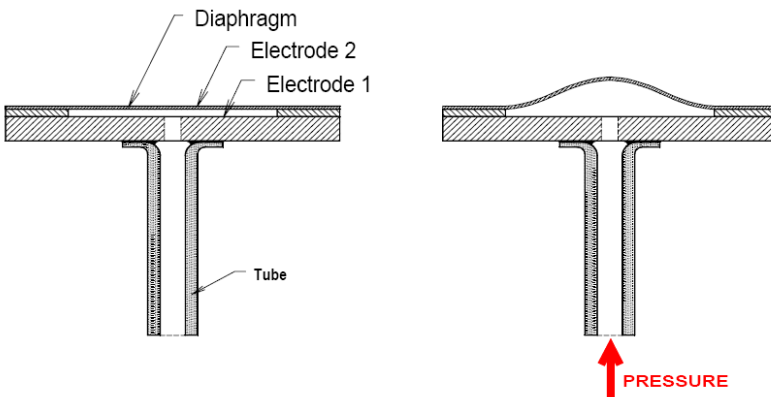


Fig. 4.21. A cross-section of a thick film capacitive pressure sensor (not to scale). The construction is on the left and the working condition is on the right [14]

4.4. Force sensors

The LTCC force sensor is described by Gongora Rubio [15]. The structure consists of several ceramic tapes, metal electrodes and embedded piezoresistive paste. The change in resistance of any resistor under applied force is due to the changes in dimensions of the resistor. The geometry of the piezoresistive sensors are shown in Fig. 4.22, (a) a planar structure, (b) a vertical structure, (c) a structure with surrounded dielectric and in (d) vertical structure suitable for z-axis force sensing.

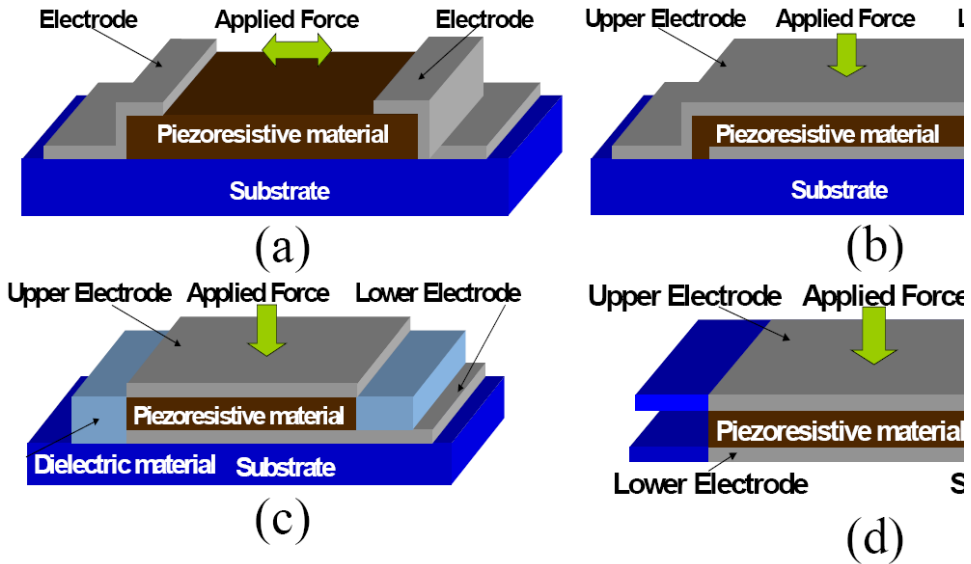


Fig. 4.22. LTCC thick film force sensors geometries [15]

4.5. Proximity sensor

The LTCC multilayer eddy current proximity sensor is presented in Fig. 4.23 and Fig. 4.24 [8,16]. Non-contact displacement sensors are generally grouped in three categories: eddy current, capacitive and optical.

Eddy current proximity sensors, in particular ceramic ones, could be used in many industrial applications due to their ability to work in harsh environments. The applications range are from metallic target positioning, detection of holes, rivets or screws, precise measurement of automobile wheel position in ABS braking systems. The eddy current proximity sensor has a multilayer coil incorporated into a LC oscillator as shown in Fig. 4.24. When this circuit is powered-up it creates a weak electromagnetic field near the coil. If metallic targets are introduced in this field, eddy currents are induced in the target changing the circuit output frequency by the modification of the coil inductance.. The fabricated proximity sensor exhibits the following properties: non-contact device, full scale of hundreds micrometers, could work at high temperature and with various materials (different dielectric constants) in the gap region. A multilayer square spiral coil of 1 cm x 1 cm with special geometry was designed in order to reduce the quantity of interconnection vias. A single layer was designed to make silver conductors of 80 μm lines and 10 μm thickness with 80 μm space between the lines, forming a 20-turn single layer coil. A five-layer proximity sensor coil was fabricated using DuPont 951 LTCC ceramic system following a typical process sequence, using interconnecting vias of 250 μm . 3D planar non-contact proximity sensors with low internal capacitance allow to use higher frequency in the associated oscillator. In addition it allows reduced dimensions for better target tracking, 3 mm full-scale measurements, operation at moderate temperature and it is fully compatible with all hybrid electronics. The proximity sensor characteristics are shown in Fig. 4.25.

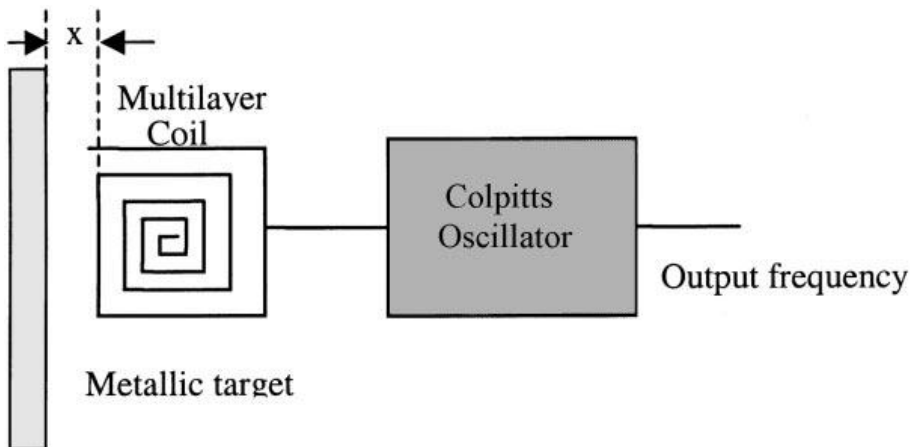


Fig. 4.23Block diagram of a proximity sensor [8]

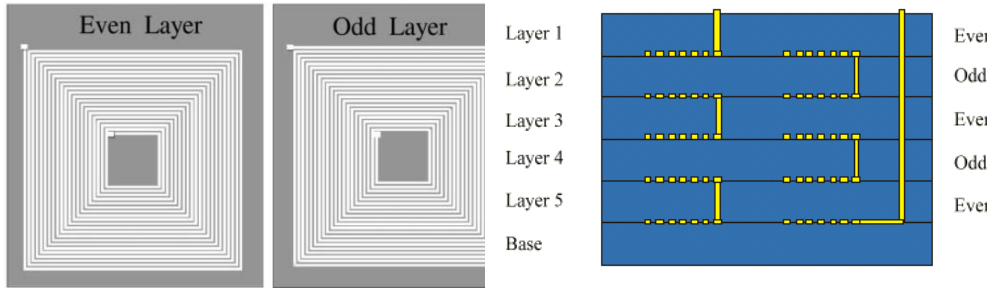


Fig. 4.24. Coil geometry and interconnection for a proximity sensor [8]

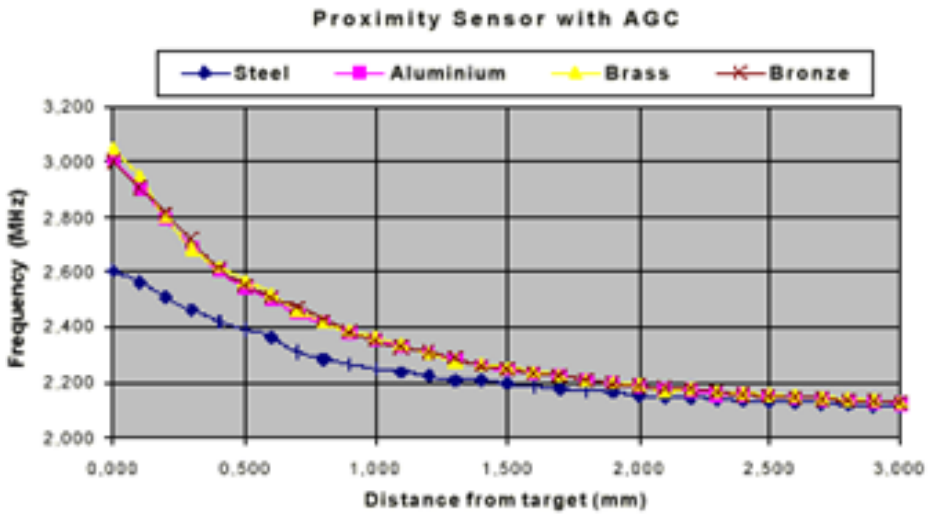


Fig. 4.25. A proximity sensor characteristics [16]

References

- [1] J.W. Gardner, *Microsensors*, Wiley, New York, 1995.
- [2] L. Michalski, K. Eckersdorf, J. Kucharski, *Termometria przyrządy i metody*, Politechnika Łódzka, 1998.

- [3] P. Markowski, A. Dziedzic, E. Prociów, Thick/thin film thermocouples as Power Source for autonomous Microsystems - preliminary results, Proc. Conf. IMAPS Poland Chapter, Wroclaw 2004.
- [4] M. Prudenziati, Thick film sensors, Elsevier Science B. V., Amsterdam, 1994.
- [5] J. Kita, Ph.D. Dissertation, Wroclaw University of Technology, 2003.
- [6] <http://www2.dupont.com/MCM/>
- [7] <http://www.electroscience.com/>
- [8] M.R. Gongora-Rubio, P. Espinoza-Vallejos, L. Sola-Laguna, J.J. Santiago-Aviles, Overview of low temperature co-fired ceramics tape technology for meso-system technology (MsST), Sensors & Actuators A89, 222-241 (2001).
- [9] D. Güteryüz, W. Smetana, Mass Flow Sensor Realized in LTCC-Technology, Proc. Conf. IMAPS Poland Chapter, Koszalin-Darłówko 2005, pp. 373-376.
- [10] D. Jurków, L. Golonka, H. Roguszczyk, LTCC gas flow detector, Proc. 16th European Microelectronics and Packaging Conf., Oulu (Finland), 2007, pp. 204-207.
- [11] A. Cattaneo, R. Dell'Acqua, G. Dell'Orto, L. Pirozzi, C. Canali, A practical utilization of the piezoresistive effect in thick film resistors: a low cost pressure sensor, Proc. IMS (ISHM-USA), 1980, pp. 221-228.
- [12] L.J. Golonka, A. Dziedzic, H. Roguszczyk, S. Tankiewicz, D. Terech, Novel technological and constructional solutions of pressure sensors made in LTCC technology, Optoelectronic and Electronic Sensors IV, Jerzy Frączek, Editor, Proceedings of SPIE, 2000, vol. 4516, pp.10-14.
- [13] U. Partsch, D. Arndt, H. Georgi, A new concept for LTCC based pressure sensors, Proc. CICMT Conference, Denver 2007, pp. 367-372.
- [14] D. Belavic et al., Benchmarking different types of thick-film pressure sensors, Proc. CICMT Conference, Denver 2007, pp. 278-285.
- [15] M.R. Gongora-Rubio et al, LTCC post load cell, Proc. CICMT Conference, Denver 2006.
- [16] M.R. Gongora-Rubio, L.M. Sola-Laguna, M. Smith, J.J. Santiago Aviles, LTCC technology multilayer eddy current proximity sensor for harsh environments, Proc. of the 32nd Int. Symp. on Microelectronics, IMAPS'99, 1999, Chicago, pp. 676-681.

Chapter 5

LTCC and thick film chemical sensors

5.1. Humidity sensors

There are many methods of measuring humidity. Some of them are presented in Table 5.1.

Table 5.1.

Methods of humidity measurement

Principle	Operating mechanism
Capacitance water	dielectric constant of material varies with absorbed
Dew point	temperature corresponding to condensation-evaporation equilibrium at a cooled surface varies with H ₂ O
Resistance	conductivity depends on H ₂ O absorbed
Piezoelectric	hygroscopic coating changes crystal frequency
Gravimetric	a volume of moist air is exposed to a drying agent, subsequently weighted
Hygroscopic	length of fibre varies with H ₂ O
Infrared	absorption from 1.5 to 1.93 μm
. . . .	

Two groups of materials are commercially used as resistance or capacitance humidity sensors: organic polymers and ceramics. Polymer sensors exhibit the disadvantages of hysteresis, slow response time, long-term drift and degradation upon exposure to some solvents. Moreover, they cannot operate at high temperature and humidity. Ceramic sensors have advantages over the polymer sensors in terms of better thermal stability and resistance to chemicals. However, ceramic sensors need periodic thermal regeneration to recover their humidity-sensitive properties. Thick film technology enables reproducible production of ceramic sensors with a defined microstructure, determined porosity and proper structure of grains and grain boundaries. These factors are vital for the development of humidity sensors with good parameters. Moreover, both the humidity sensor and the heater used for

periodic regeneration can be made on a single substrate in the same technological process. Integration of the sensor and the electronic conditioning system is also possible. Most thick film humidity sensors work on the principle of impedance variation. The change in impedance, resistance or capacitance measured at a constant frequency, with relative humidity changes is widely used in practice. Thick film humidity sensor characteristics depend on the bulk and surface properties of the ceramic material. The properties are determined by the pore size distribution, average particle size and additives [1].

The humidity sensor requirements:

- high sensitivity in a wide humidity range,
- short response time,
- reproducibility (no hysteresis),
- long life time,
- resistance to impurity,
- no influence of temperature,
- simple construction,
- low cost.

Disadvantages of the humidity sensors:

- long-term drift,
- limited operating temperature range,
- slow response time and hysteresis.

There are many fields of humidity sensors applications:

- industrial processes,
- human health and comfort,
- home appliances,
- electronic equipment,
- medical equipment,
- agriculture,

The mechanisms of water adsorption are very important in case of ceramic sensors. Water can be adsorbed in three various ways. There are:

- chemical adsorption,
- physical adsorption,
- free water (macropores).

The strongest adsorption force is in the case of the chemical adsorption, where the first monolayer of water is formed on the material surface. The successive water layers are adsorbed by physical forces. The weakest connection of water to the material occurs in macropores where free water is adsorbed. Very important for proper designing of ceramic humidity sensors is the knowledge of the adsorption – sorption curves. The dependence of such curves upon temperature and the kind of material is shown in Fig. 5.1.

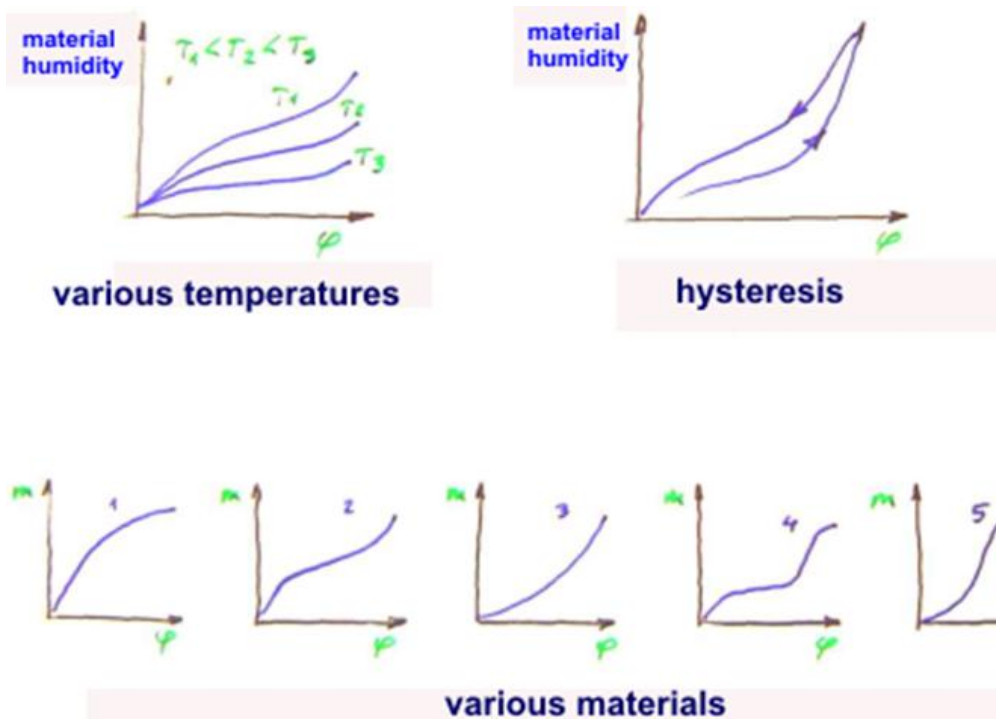


Fig. 5.1. H₂O adsorption – sorption curves (T - temperature, φ - relative humidity, m - mass of adsorbed water)

There are many parameters describing the level of humidity in the air. The most popular one is the relative humidity, marked by RH, R_H or φ . The definition of the relative humidity is shown in Fig. 5.2.

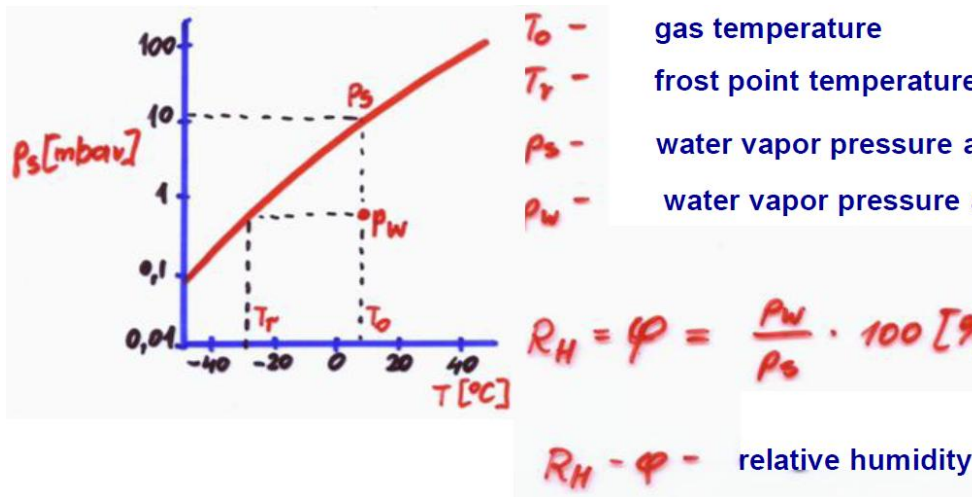


Fig. 5.2. Curve p_s versus T with marked parameters used for definition of the relative humidity in air

Ceramic humidity sensors

Humidity sensing principle of porous oxide semiconductors ($MgCr_2O_4-TiO_2$, $MnWO_4$, etc.) is based on electrical conductivity measurements. Bulk resistivity is measured as impedance. The sensitivity of "porous" oxide semiconductors is satisfactory. Dopants added to the mixture play a role of catalyst. They promote the dissociation of adsorbed water into hydrogen and hydroxyl ions. The hydroxyl ions reduce the bulk resistivity. Electrical properties of the ceramic humidity sensor depend on:

- surface properties (hydrophobic, hydrophilic),
- microstructure (pore sizes distribution),
- electrical properties of the material.

The ceramic sensors exhibit some disadvantages. Humidity sensing mechanism is based on the adsorption of water vapour and therefore there is a degradation by surface contamination.

The structure of thick film ceramic humidity sensor is presented in Fig. 5.3. Schematic illustration of water adsorption at various level of relative humidity in the air is shown in Fig. 5.4.

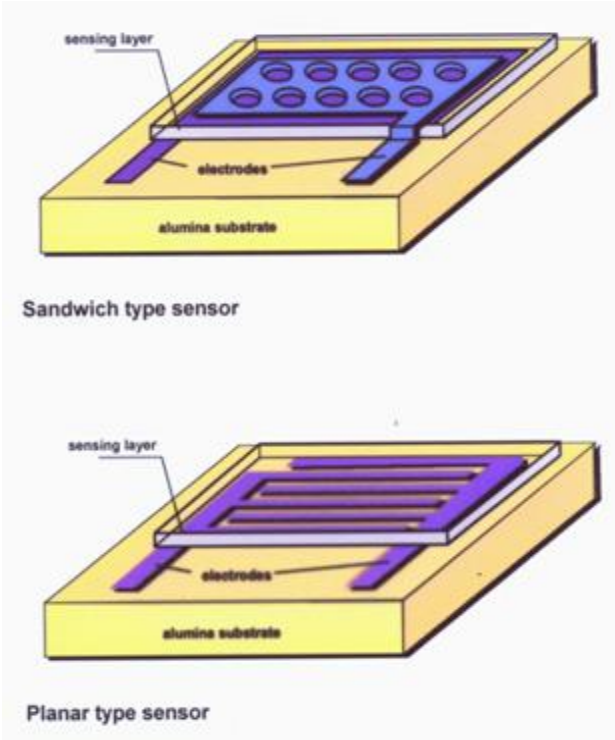


Fig. 5.3. The structure of thick film ceramic humidity sensor [2]

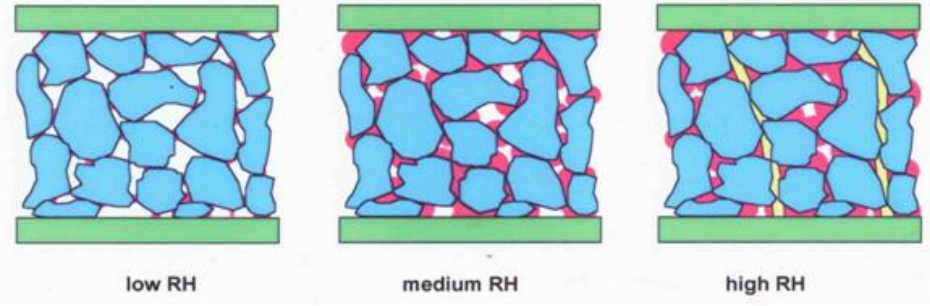


Fig. 5.4. Schematic illustration of water adsorption [2]

The RH dependence of resistance $\log R = f(\text{RH})$ for the $\text{ZnCr}_2\text{O}_4\text{-TiO}_2$ thick film sensor is presented in Fig. 5.5 [1]. The characteristics were measured at the optimal working frequency (maximum of sensitivity). The changes of resistance with humidity encompass four orders of magnitude. The characteristics can be approximated by a straight line. The relationship between the logarithm of resistance and relative humidity follows an almost perfect straight line.

The response time to the variation of RH is influenced by the microstructure, which depends on the micropores formation and the sintering conditions due to the thermal treatment. A fast response time is obtained in the case of large pores. The easy adsorption and desorption of water molecules are the dominating processes [1].

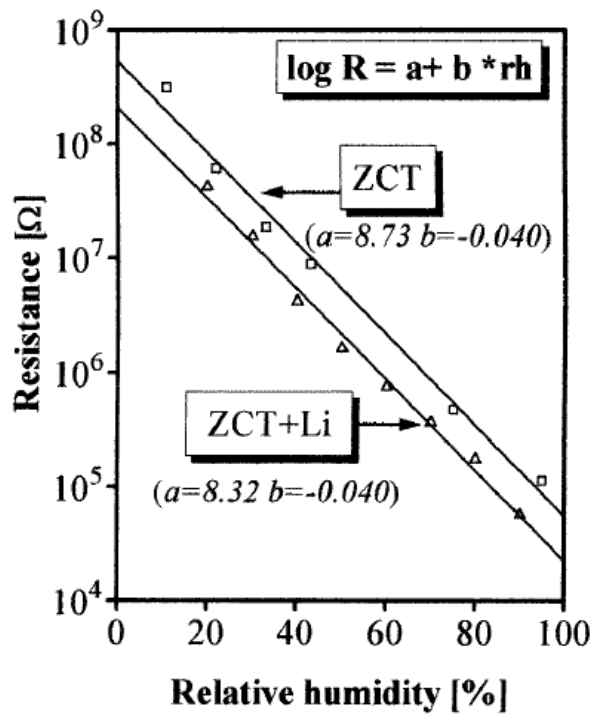


Fig. 5.5. The RH dependence of resistance for the $\text{ZnCr}_2\text{O}_4\text{-TiO}_2$ sensor [1]

5.2. Gas sensors

Semiconductor gas sensors

Two types of thick film gas sensors are mainly used: semiconductor and electrochemical. The semiconductor ones are based mostly on Sn and Zn oxides as gas sensitive material. The resistance of the sensor depends on the gas concentration. Poor sensitivity is the main disadvantage of such sensors. To overcome this problem the gas sensor array is made on one substrate. The sensors in the array are made from various gas sensitive materials and work at different temperatures. The response of each sensor to various gases is different. The selectivity can be improved by collecting the data from all sensors. The array of thick film sensors made from gas sensitive semiconductors ZnO, SnO₂ and WO₃ with various dopants is presented in Fig. 5.6 [3]. The sensitivity of these sensor materials to various gases is shown in Fig. 5.7. The height of the energetic barrier between semiconductor oxide grains depends on the gas concentration (Fig. 5.8). It explains the dependence of sensor resistance versus gas concentration. Thick film gas sensor structure is shown in Fig. 5.9.

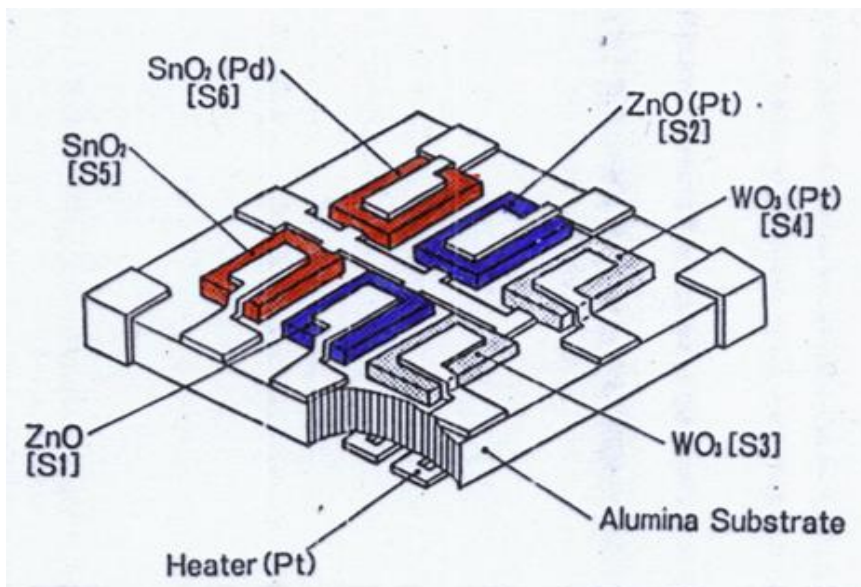


Fig. 5.6. Array of thick film gas sensors [3].

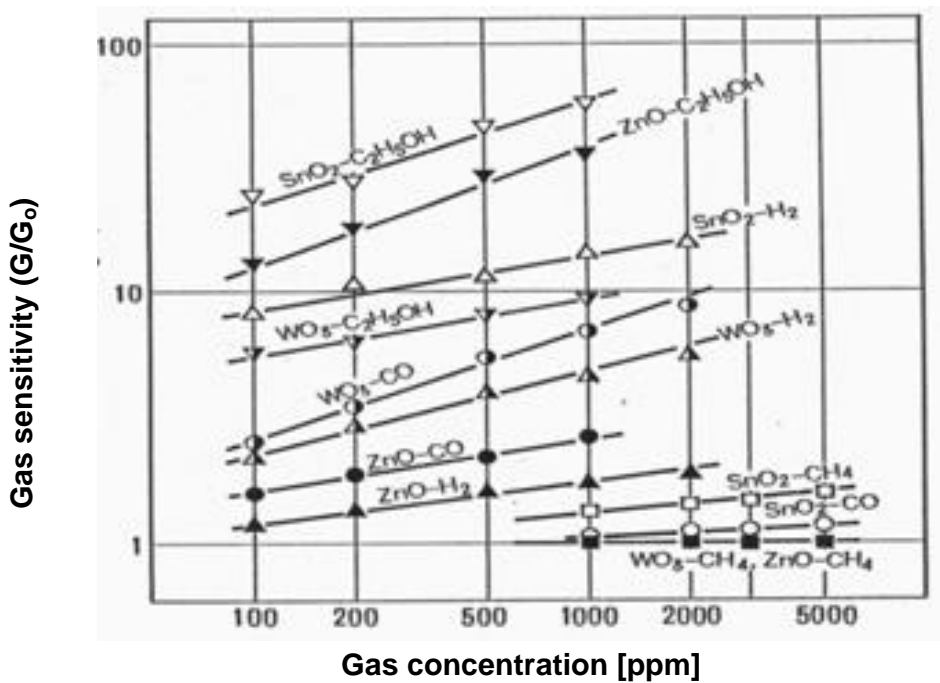
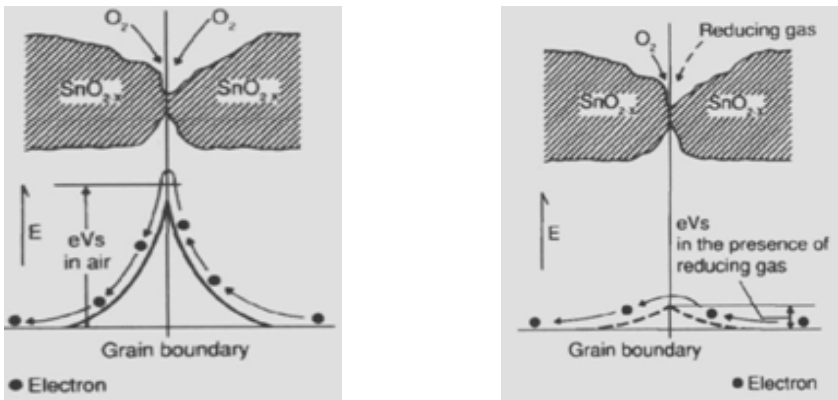


Fig. 5.7. Gas sensitivity versus different gases concentration for the sensors made from various gas sensitive thick film semiconductor oxides shown in Fig. 5.6 [3]



(a)

(b)

Fig. 5.8. The model of inter-grain potential barrier: in absence of gases (a), in presence of reducing gases (b) [4]

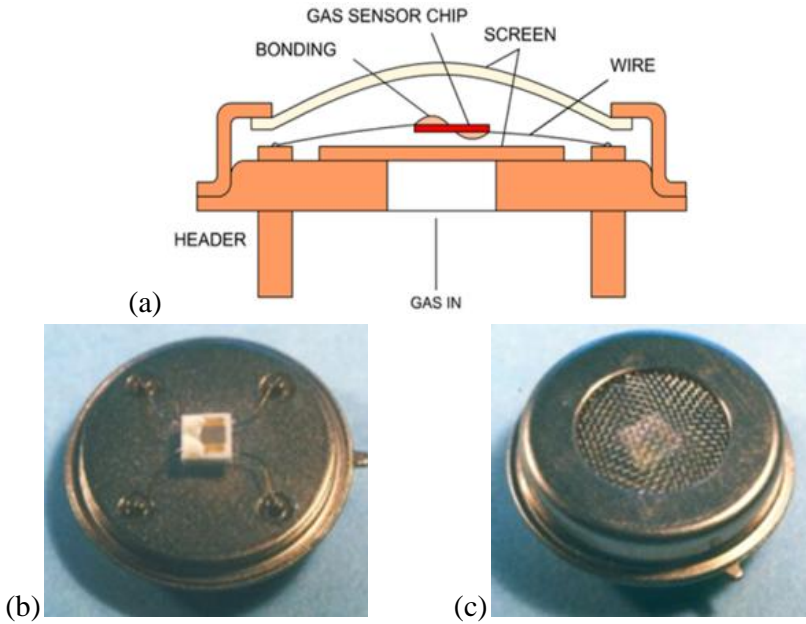


Fig. 5.9. Thick film gas sensor: schematic draw (a), thick film substrate with gas sensitive material (b), sensor with a metal cover (c) [5]

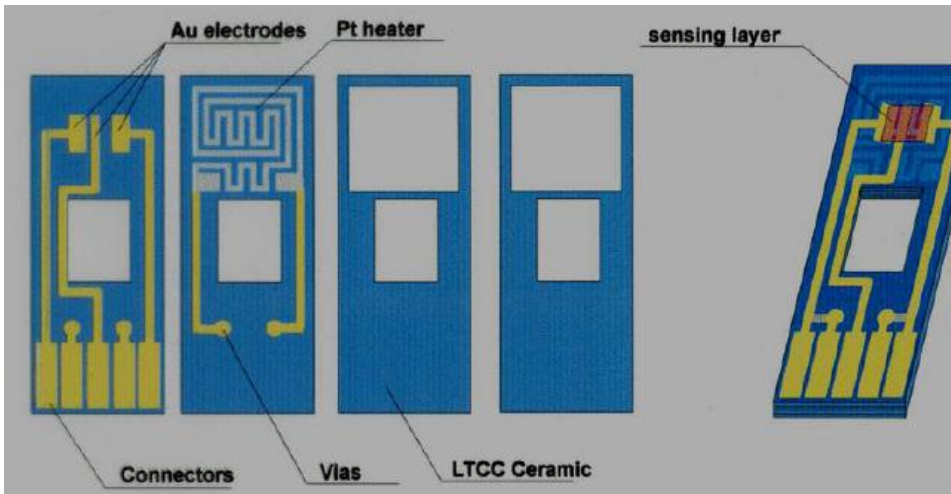


Fig. 5.10. Design of LTCC multilayer gas sensor [6]

The design of thick film gas sensor made on LTCC multilayer is presented in Fig. 5.10. Characteristics of the LTCC gas sensor embedded heater and the sensor response to CH_4 and CO are presented in Fig. 5.11 and 5.12, respectively.

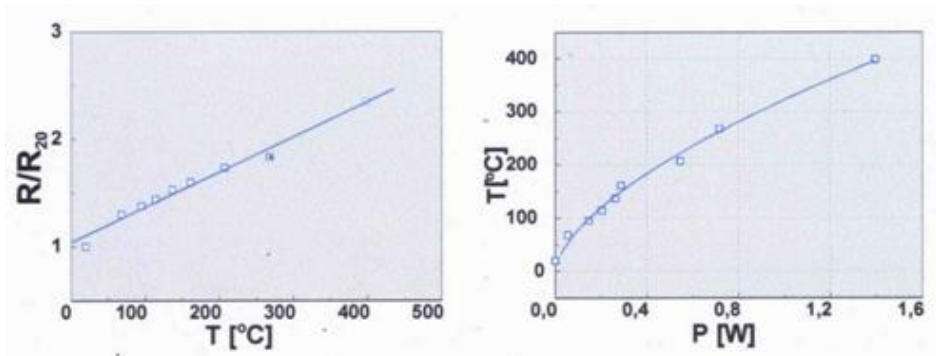


Fig. 5.11. Characteristics of LTCC gas sensor heater [7]

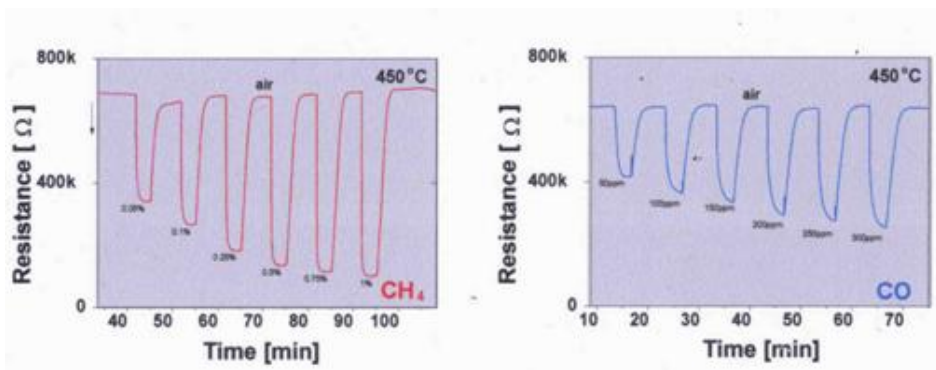


Fig. 5.12. LTCC gas sensor response [7]

Electrochemical gas sensors

Thick film and LTCC electrochemical gas sensors are made from solid state electrolyte. There is only ion conductivity in such electrolytes. The sensors work at high temperature so as to ensure appropriate level of electrical conductivity. There are two modes of the sensors work: potentiometric (the electromotive force generated on the sensor electrodes depends on the difference in the gas concentration on the both sides of the thick film electrolyte - Fig. 5.13) and amperometric (electrical current depends on the gas concentration - Fig. 5.14).

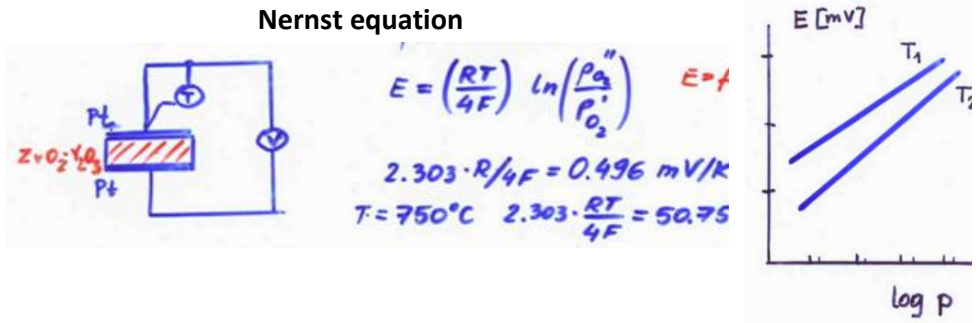


Fig. 5.13. Potentiometric gas sensor - schematic draw and basic characteristics

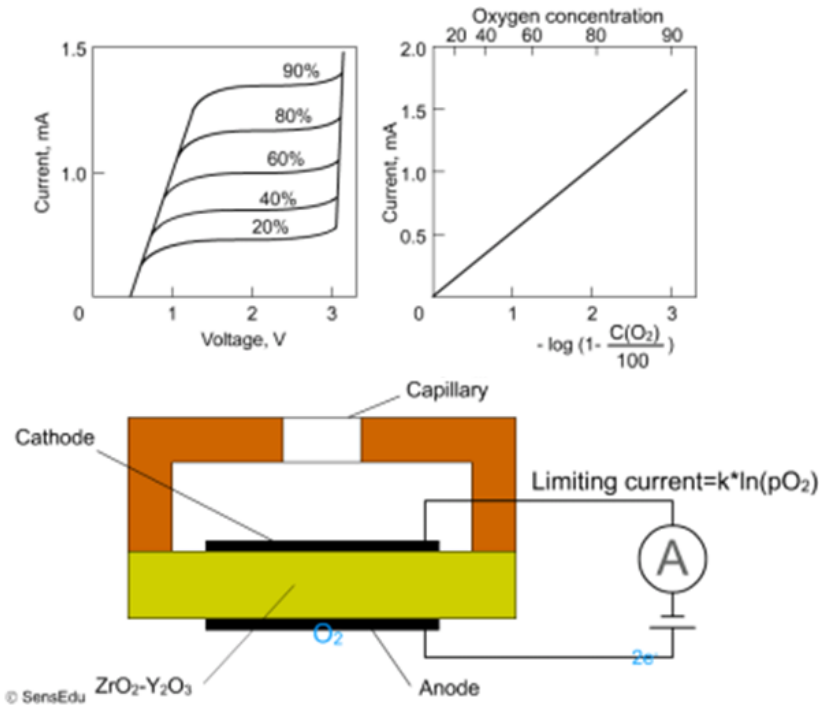


Fig. 5.14. Electrochemical amperometric O_2 sensor [5]

There are many advantages of electrochemical gas sensors:

- simple measurement of the generated voltage,
- gas partial pressure directly converted to electrical signal,
- generated voltage does not depend upon the sensor dimension,
- good selectivity,
- generated voltage depends logarithmically upon gas,

- concentration measurements in very wide range,
- calibration not required,
- very good mechanical properties (vibration, acceleration resistant),
- chemical inertness,
- long life time,
- stability in wide temperature range,
- low power,
- easy management,
- low cost.

Disadvantages of the electrochemical gas sensors:

- long response time,
- low accuracy in measurements of small concentration changes (logarithmic scale),

References

- [1] L. Golonka, B.W. Licznerski, K. Nitsch, H. Teterycz, Thick-film humidity sensors, *Meas. Sci. Technol.* 8, 1997, pp. 92–98.
- [2] L. Golonka, B.W. Licznerski, K. Nitsch, H. Teterycz, Thick film humidity sensors based on different materials, *Int. Symposium on Microelectronics ISHM, Los Angeles (USA), 1995, Proc. pp. 107-112.*
- [3] M. Kaneyasu, M. Ikegami, A. Arima, H. Iwanaga, S., Smell Identification using a thick-film hybrid gas sensor, *IEEE Transactions on Components, Hybrids, and Manufacturing Technology* vol. 10 (2), 1987, pp. 267-273.
- [4] Figaro gas sensors - data sheet.
- [5] www.ett.bme.hu
- [6] H. Teterycz, J. Kita, R. Bauer, L. Golonka, B.W. Licznerski, K. Nitsch, K. Wiśniewski, New design of SnO₂ gas sensor on Low Temperature Cofiring Ceramics, *Sensors and Actuators B*, vol.47/1-3, 1998, pp. 100-103.
- [7] H. Teterycz, J. Kita, R. Bauer, L. Golonka, B.W. Licznerski, K. Nitsch, K. Wiśniewski, New design of SnO₂ gas sensor on Low Temperature Cofiring Ceramics, *Eurosensors Conf.*, Warsaw, 1997.

Chapter 6

Foundation of microfluidics

6.1. Introduction

Microfluidics is the term that is used to describe flow in miniature devices having characteristic dimensions ranging from single millimetres to hundreds of nanometers. The microfluidic devices thanks to their very small size are capable of handling volume of fluid (gas or liquid) in range of nano- and microliters ($10^{-9} - 10^{-6} l$) [1,2]. In the last two decades there has been an explosion of scientific papers in this area. There are several reasons for this interest. One of the reasons is rapid development of the microelectronic technologies (e.g. silicon micromachining). The progress which has been made in nano- and microtechnology enables fabrication of various precise and complex spatial structures (channels, cavities, chambers, cantilevers, membranes etc.) with characteristic dimensions up to hundreds of nanometers. Another aspect is the number of possible areas of microfluidic system applications: analytical chemistry, medical diagnosis, DNA sequencing, cell separation, microbiological analysis, high-throughput synthesis, environmental monitoring and others. Analytical procedures which are applied in modern chemistry, biology and medicine consists of several steps: sample collection, carrying out an appropriate (bio)chemical reaction, separation of reaction products and detection of the analyte. Classical laboratory equipment is characterized by relatively long time of detection, lack or poor process control, considerable reagents consumption and large amount of wastes. All these disadvantages can be eliminated by use of the microfluidic devices. Thanks to the fact that these microsystems work with liquid or gas samples in the micro- or nanoliter scale, they are characterized by short response time, high sensitivity and good selectivity. Moreover,

microfluidic system produces less wastes and is much safer (especially when it works with a toxic, poisonous or explosive substance) in comparison with classical laboratory equipment used in analytical chemistry, biology or medicine.

6.2. Basic terms and equations of fluid dynamics

Reynolds number

According to chemical and process engineering there are generally two patterns of fluid flow:


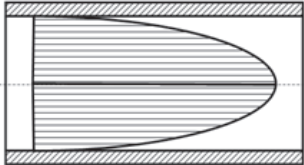
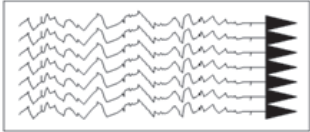
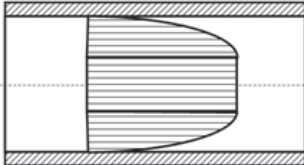
- (1) Laminar flow
- (2) Turbulent flow

For laminar flow, the forces connected with fluid viscosity dominate. As a result of this, the laminar flow is a calm flow of the fluid that moves orderly along the streamlines. Turbulent flow, on the other hand, is much more violent. In this case, inertia forces exceed viscous effects. As a consequence the fluid particles move chaotically in all directions without any traceable pattern. The transition from laminar to turbulent flow pattern is determined by the Reynolds number:

$$Re = \frac{\rho UL}{\mu} \quad (6.1)$$

where ρ is a fluid density (kg/m^3), U is a mean fluid velocity (m/s), L is a characteristic dimension (m) and μ is a fluid viscosity (Pa·s). The transition from laminar to turbulent flow occurs for $Re > 2300$. In this case, the inertia forces dominate over the viscous effects and as a result fluid recirculations and vortices are generated. However, due to very small dimensions, of almost all microfluidic systems, the fluid flow is nearly always in the laminar flow regime. A comparison between a laminar and turbulent flow of a fluid in a circular tube is given in Table 6.1.

Table 6.1. Comparison of laminar and turbulent flow of fluid in a circular tube.

Laminar flow	Turbulent flow
<div style="display: flex; align-items: center; justify-content: center;">  <div style="margin-left: 20px;"> $u_x \neq 0$ $u_y = 0$ </div> </div> <p>Fluid flows in parallel layers along streamlines. There is no distribution between the layers.</p> <div style="display: flex; align-items: center; justify-content: center;">  </div> <p>Parabolic flow pattern:</p> $\frac{u_x(s)}{u_{\max}} = \left[1 - \left(\frac{s}{r}\right)^2\right]$	<div style="display: flex; align-items: center; justify-content: center;">  <div style="margin-left: 20px;"> $u_x \neq 0$ $u_y \neq 0$ </div> </div> <p>Fluid flows chaotically in all directions without any traceable pattern.</p> <div style="display: flex; align-items: center; justify-content: center;">  </div> <p>Flatten flow pattern</p> $\frac{u_x(s)}{u_{\max}} = \left[1 - \left(\frac{s}{r}\right)^{\frac{1}{7}}\right]$

In practice, a conduit geometry can significantly influence the value of the Reynolds number at which the transition from laminar to turbulent flow occurs. Therefore, the parameter L given in equation (6.1) is very often replaced by a hydraulic diameter D_h . It is a commonly used term when handling the fluid flow in non-circular channels. The hydraulic diameter is defined as:

$$D_h = \frac{4A}{O} \tag{6.2}$$

where A is a cross sectional area of the conduit (m^2) and O is the “wet perimeter”. It is the conduit’s perimeter that is in contact with the fluid. It can

be noticed that hydraulic diameter from the equation (6.2) for a circular tube stands for its diameter d :

$$D_h = \frac{4A}{o} = \frac{4 \frac{\pi d^2}{4}}{\pi d} = d \quad (6.3)$$

However, in case of microfluidic structures the channels are not circular. The hydraulic diameter for a rectangular conduit with the width w and height h is equal to:

$$D_h = \frac{4wh}{2(w+h)} = \frac{2wh}{w+h} \quad (6.4)$$

for $w = h$ (square channel):

$$D_h = w \quad (6.5)$$

The second parameter from equation (6.1) which should be defined more precisely is the mean fluid velocity U . According to chemical engineering it can be defined as:

$$U = \frac{Q}{A} \quad (6.6)$$

where Q is a fluid volumetric flow (m^3/s).

The continuity equation

During the flow of a fluid through a conduit, the mass flow is constant in every place of the channel. The continuity equation of fluid flow is used to determine the volumetric flow rates. Fig. 6.1 illustrates a control volume of the fluid enclosed between two surfaces A_1 and A_2 which are separated by an

infinitesimally small distance dl . The mean velocity and density of the fluid at the surface A_2 are equal to:

$$u_2 = u_1 + \frac{\partial u}{\partial l} dl \quad (6.7)$$

$$\rho_2 = \rho_1 + \frac{\partial \rho}{\partial l} dl \quad (6.8)$$

$$A_2 = A_1 + \frac{\partial A}{\partial l} dl \quad (6.9)$$

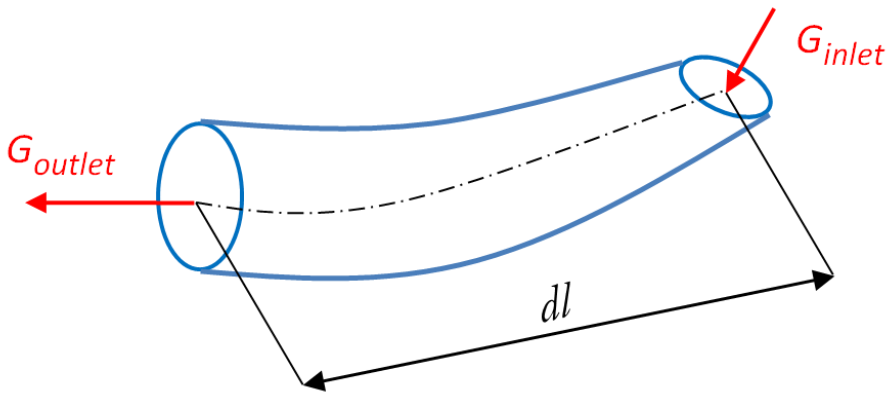


Fig. 6.1. Continuous fluid flow in a conduit.

The mass flow rate at the inlet and outlet is equal to:

$$G_{inlet} = u_1 \rho_1 A_1 \quad (6.10)$$

$$G_{outlet} = \left(u_1 + \frac{\partial u}{\partial l} dl \right) \left(\rho_1 + \frac{\partial \rho}{\partial l} dl \right) \left(A_1 + \frac{\partial A}{\partial l} dl \right) \quad (6.11)$$

By the law of mass conservation, we should obtain the following relation:

$$G_{inlet} = G_{outlet} \quad (6.12)$$

therefore, the rate of the mass flow in the steady-state flow condition with $\frac{d}{dt}(u\rho A) = 0$, or:

$$G = u_1\rho_1A_1 = u_2\rho_2A_2 \quad (6.13)$$

For incompressible fluids (e.g. liquids) equation (6.13) can be used to determine the volumetric flow rate:

$$Q = u_1A_1 = u_2A_2 \quad (6.14)$$

The fluidic dynamic continuity equation is analogous to Kirchoff's Current law known from electronic circuits. The rate at which mass enters is equal to the rate at which it leaves the system (Fig. 6.2).

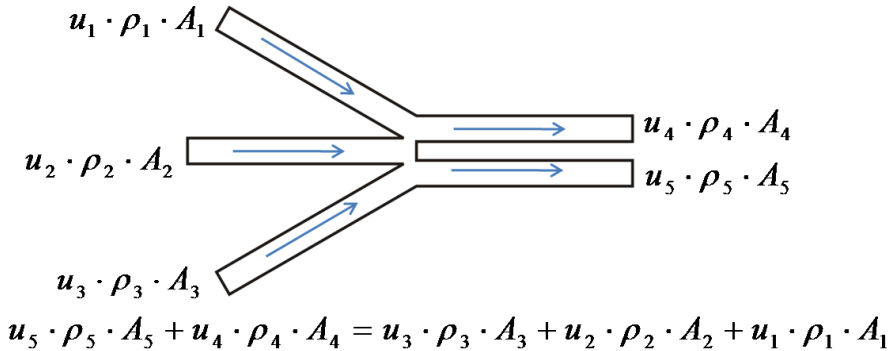


Fig. 6.2. Illustration of the fluidic continuity equation.

Navier-Stokes equation

Mathematical description of fluid flow is based on momentum conservation law which is represented by the Navier-Stokes equation. Derivation of the equation is beyond the scope of this book. It can be find in fluid dynamics

books [e.g. 3,4]. For a general case the equation can be presented in the following form:

$$\frac{\partial(\rho u)}{\partial t} + u\nabla(\rho u) = -\nabla p + \mu\nabla^2 u + F \quad (6.15)$$

It is a partial differential equation in which $u = (u, v, w)$ is the fluid velocity vector with (m/s) unit, p is a pressure (Pa) and F is an external driving force (N).

The presented Navier-Stokes equations are partial differential equations which have analytical solutions only for a few very simple cases. Therefore, more sophisticated cases have to be solved using CFD (Computational Fluid Dynamic) methods. Although equation (6.15) describes the incompressible flow, it is valid for the flows with spatially varying density $\rho = \rho(x, y, z)$ and viscosity $\mu = \mu(x, y, z)$ as well. For the flows with constant density and viscosity (e.g. liquids), the Navier-Stokes equation can be simplified to:

$$\rho \left(\frac{\partial u}{\partial t} + u\nabla u \right) = -\nabla p + \mu\nabla^2 u + F \quad (6.16)$$

In case of microfluidic systems, it is common that the Reynolds number is very low and the fluid flow can be approximated as a creeping flow (Stokes flow). In a consequence, the convection term $u\nabla u$ in equation (6.16) can be neglected and the Navier-Stokes equation simplifies to:

$$\rho \frac{\partial u}{\partial t} = -\nabla p + \mu\nabla^2 u + F \quad (6.17)$$

The Stokes flow can be regarded as a quasi-steady flow, therefore, the time derivative term from equation (6.17) can be also neglected and the fluid flow in a microscale can be described by equation:

$$\nabla p = \mu \nabla^2 u + F \quad (6.18)$$

Pressure drop

During a fluid flow through a conduit losses of energy occur. This lost energy is returned to the surroundings in form of heat. Fluid energy losses are caused by a hydraulic resistance which can be indentified by pressure drop along the fluidic conduit. The pressure drop occurs as a result of changes of the fluidic channel configuration (broadening or contraction of the cross-sectional area) and due to friction between the fluid and contacting conduit's walls (viscous losses). The pressure drop caused by broadening of the channel's cross-sectional area (Fig. 6.3) can be described by the equation:

$$\Delta P = \xi \frac{\rho u_1}{2} \quad (6.19)$$

$$\xi = \left(1 - \frac{A_1 \rho_1}{A_2 \rho_2}\right)^2 \quad (6.20)$$

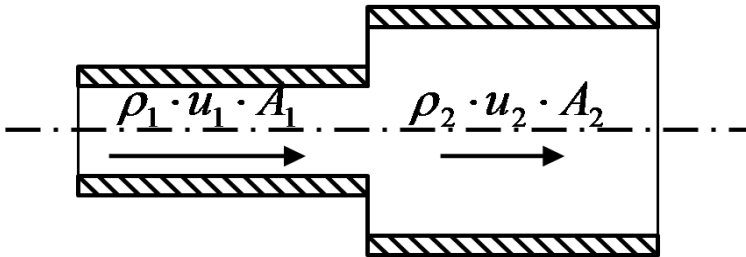


Fig. 6.3. Broadening of the conduit's cross-sectional area.

where ΔP is a pressure drop (Pa) and ξ is a coefficient of local resistance.

The pressure drop takes place during contracting of the conduit's cross-sectional area, as well (Fig. 6.4). Inertia of the fluid stream causes an increase of fluid velocity and contraction of the flow area. However, the increase of

fluid velocity and reduction of the flow area are higher than it results from the continuity equation (6.14). In consequence, the *contraction area* is generated. The fluid stream which flows out from the *contraction area* adjust its velocity to the real channel's cross-sectional area. The equivalent pressure drop due to the contraction of the channel's cross-sectional area is given by the following equation:

$$\Delta P = \xi \frac{\rho u_2^2}{2} \quad (6.21)$$

$$\xi = \left(\frac{1-C_1}{C_1} \right)^2, C = \frac{A_1}{A_2} \quad (6.22)$$

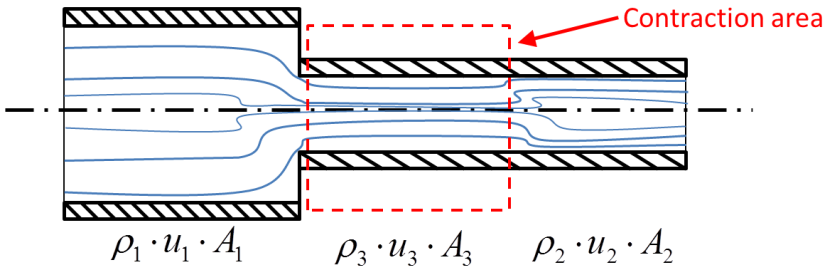


Fig. 6.4. Contracting of the conduit's cross-sectional area.

Where C_l is a coefficient of contraction and typically is ranging from 0.6 to 1. The second reason of pressure drop inside the fluidic conduit is a friction between the fluid and the contacting wall. The friction results in additional pressure drop which can be calculated using the Darcy-Weisbach equation:

$$\Delta P = f \frac{l}{D_h} \frac{\rho u^2}{2} \quad (6.23)$$

where f is the Darcy friction factor. For a laminar flow, which is characteristic for the microfluidic systems, the Darcy friction factor is equal to:

$$f = \frac{C_2}{Re} \quad (6.24)$$

where Re is the Reynolds number and C_2 is a friction coefficient which depends on the conduit's geometry. Exemplary values of the friction coefficient are presented in table 6.2.

Table 6.2. Friction coefficient for various configurations of the fluidic channel.

Configuration	D_h	D
Circular	d	64
Square	$w=h$	57
Rectangular	$2wh/(w+h)$	96

Scaling laws in microfluidics

When the characteristic dimensions of the system decrease from macroscopic to the microscopic scale, some effects that are negligible at macroscale become significant at microscale, and vice versa. For example the effects of gravity become negligible in comparison with the adhesive and friction effects [5]. Surface tension and viscous forces of the fluid have a significant impact on a fluid flow in microscale. They can drastically and rapidly damp any motion. At high velocities, the hydrodynamics is unstable, and the turbulent flow occurs. According to the description given in the previous section of this book, the transition from laminar to turbulent flow takes place when $Re > 2300$. One phenomenon which can be deduced from equation (6.1) is that the Reynolds number is directly proportional to the second power of the conduit characteristic dimension:

$$Re \sim L^2 \quad (u \sim L) \quad (6.25)$$

This means that the turbulence disappears in the microsystems in which fluid flows.

Similar observation can be made for the pressure drop in the fluid over the channel length. The relation between the pressure drop and characteristic dimension of the conduit can be derived from the Darcy-Weisbach formula (6.23) and equation (6.1) and (6.24) as:

$$\Delta P = C_2 \frac{\mu l U}{2D_h^2} \quad (6.26)$$

One interesting phenomenon can be concluded from equation (6.26). For a circular tube the pressure drop is inversely proportional to the fourth power of the tube radius r :

$$\Delta P = \frac{8\mu l Q}{\pi r^4} \quad (6.27)$$

$$\Delta P \sim r^{-4} \quad (6.28)$$

A similar calculations can be made for other configurations of the fluidic channel:

for a square channel:

$$\Delta P \sim w^{-4} \quad (6.29)$$

for a rectangular channel:

$$\Delta P \sim w^{-1}h^{-3} \quad (6.30)$$

The conclusion which comes from equations (6.28), (6.29) and (6.30) is that the 16 times higher pumping power would be required to pump the same

amount of volumetric flow of fluid with the conduit dimensions reduced by half.

Another important aspect which has to be taken into account is the influence of surface tension. The surface tension in liquids relates to the cohesion forces of the molecules. As can be seen in Fig. 6.5, for the molecules in the liquid there is a balance of the cohesive forces. However, the molecules which are closer to the liquid-gas or liquid-solid interface are not bonded in the same way. When the cohesive forces between the molecules located inside the liquid are larger than interaction with gas/solid molecules, the contact area becomes concave upward. The surface tension F_s in a liquid can be expressed as:

$$F_s = S \cdot \gamma \quad (6.31)$$

where S is a wet perimeter (m) and γ is a coefficient of surface tension (N/m).

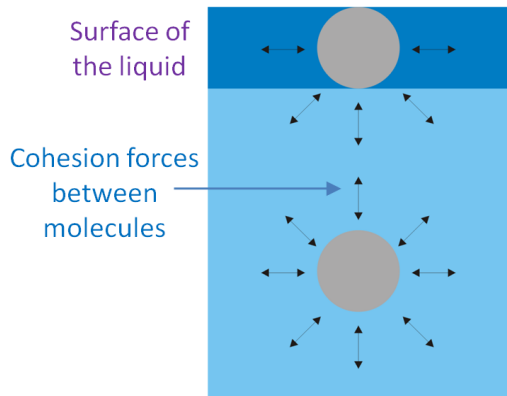


Fig. 6.5. Superficial tension forces at the interface between a liquid and air.

The influence of surface tension becomes significant in the case of fluid flow in microchannels, as an additional pressure has to be overcome to move the liquid [6]. The relation between the surface tension and pressure is given by the Laplace equation:

$$\Delta P = \gamma C_3 \quad (6.32)$$

where C is the curvature of the fluid surface. The curvature depends on geometry of the microconduit and can be defined as:

for a circular tubes:

$$C_3 = \frac{2}{r} \quad (6.33)$$

for a non-circular tubes:

$$C_3 = \frac{1}{r_1} + \frac{1}{r_2} \quad (6.34)$$

where r is the curvature radius for the fluid in a circular tube and r_1 and r_2 are the curvatures of a non-circular conduit.

One can notice that reducing of the channel dimensions leads to an increase in pressure drop due to fluid surface tension. For example, the total pressure change in a free-standing liquid inside a circular conduit with a diameter $d = 2r$, as shown in Fig. 6.6, can be estimated as a sum of the pressure changes in the liquid cylinder and liquid sphere [7]:

$$\Delta P = \Delta P_{cylinder} + \frac{1}{2} \Delta P_{sphere} \quad (6.35)$$

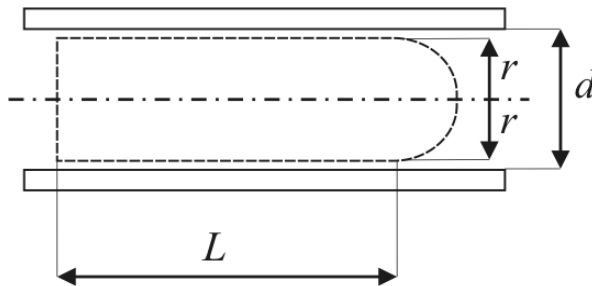


Fig. 6.6. Fluid volume in a circular tube.

For a liquid cylinder, as presented in Fig. 6.7, the pressure change due to surface tension can be calculated by dividing the surface tension F_s by the lateral area of the cylinder ($2rL$).

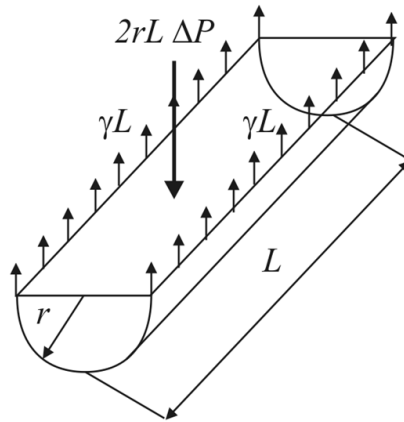


Fig. 6.7. Pressure change due to surface tension across the liquid cylinder [7].

According to equation (6.31) surface tension is equal to wet perimeter ($2L$) times the coefficient of surface tension (γ). Therefore, the pressure change in the liquid cylinder due to the surface tension is equal to:

$$\Delta P_{cylinder} = \frac{\gamma}{r} \quad (6.36)$$

The pressure change due to surface tension for a liquid sphere, as presented in Fig. 6.8, can be calculated using analogous procedure, from which we have:

$$\Delta P_{sphere} = \frac{2\gamma}{r} \quad (6.37)$$

Therefore, according to equations (6.35), (6.36) and (6.37) the total pressure change in a free-standing liquid inside a circular conduit is equal to:

$$\Delta P = \frac{\gamma}{r} + \frac{1}{2} \left(\frac{2\gamma}{r} \right) = \frac{2\gamma}{r} \quad (6.38)$$

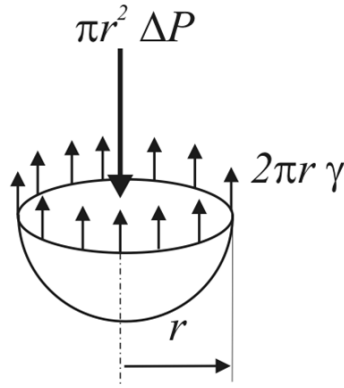


Fig. 6.8. Pressure change due to surface tension across the liquid sphere [7].

The coefficient of surface tension depends on the contact angle between the liquid and the solid. For a hydrophobic materials the contact angle is high while for hydrophilic materials are characterized by good wettability (low contact angle). Therefore, the use of hydrophobic material increases the pressure which is required to move the fluid inside the microchannel. As can be seen in Fig. 6.9 the pressure required to move the liquid (ΔP_1) is higher when the liquid–air interface reaches the region of increased hydrophobicity (ΔP_2) [6].

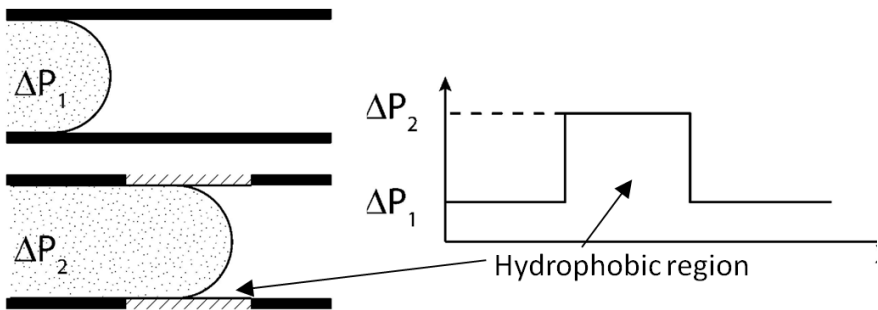


Fig. 6.9. Influence of the hydrophobic material upon pressure drop [6].

References

- [1] Ottino JM, Wiggins S, Introduction: mixing in microfluidics, Royal Society of London Transactions Series A, 362 (2004) 923-935.
- [2] Gravassen P, Branebjerg J, Jansen OS, Microfluidics – a review, Journal of Micromechanics and Microengineering, 3 (1993) 168-182.
- [3] Shaughnessy EJ, Katz IM, Schaffer JP, Introduction to fluid mechanics, Oxford University Press, 2005.
- [4] Batchelor GK. Introduction to Fluid Dynamics, Cambridge University Press, 1967.
- [5] Wautelet M, Scaling laws in the macro-, micro- and nanoworlds. European Journal of Physics, 22 (2001) 601-611.
- [6] Li D (ed.), Encyclopedia of microfluidics and nanofluidics, Springer, 2008.
- [7] Hsu TR, MEMS and microsystems design and manufacture, McGraw Hill, 2002.

Chapter 7

Technology of the LTCC-based microfluidic systems

7.1. Introduction

The chapter presents the basic method of three-dimensional (3D) structuration of the LTCC material for the applications in microfluidics. The low temperature co-fired ceramics has been used in microelectronics since the end of the 1980's. It has been applied to the fabrication of hybrid electronic circuits and ceramic multilayer structures. A typical LTCC module consists of several dielectric (alumina filled glasses or glass-ceramic) tapes, connecting vias, surface and buried thick films (conductors and passives). The conductive lines and passive components (resistors, capacitors and inductors) are deposited using standard printing technologies (screen-printing, ink-jet printing). After the deposition of thick films, all LTCC tapes are stacked together in proper order and bonded during/in a lamination process. Finally, the multilayer laminate is co-fired at the temperature of 850-900°C. Additional active and passive components can be added on the top or the bottom surface of the fired structure using wire-bonding, flip-chip or surface mounting technique (SMT). Nowadays, the LTCC technology is mainly used for automotive and telecommunication applications. However, there has been a growing interest in the developing of fluidic structures using LTCC technology in recent years. The ceramic-glass material is increasingly used for microfluidic application thanks to its outstanding physical and chemical properties. The sintered LTCC is chemically inactive and resistant to water, saline solutions, organic substances, solvents and some of acids and bases. Low temperature co-fired ceramics is characterized by a good thermal conductivity, high temperature and pressure stability. Moreover the complex and precise three-dimensional (3D) structures can be made inside the LTCC

substrate using various micromachining techniques. Quite recently, microfluidic systems have been manufactured mainly using silicon technology. However, according to the newest trends, cheaper technologies and materials are applied. The modern microfluidic devices are fabricated using relatively cheap polymeric, PCB (printed circuit board) and ceramic technologies. The advantages of the LTCC technique, in comparison with the silicon one, are lower price and shorter time of the new microsystem development. Moreover, the fabrication process of the LTCC microfluidic systems is much simpler. In comparison with PCB technology, the advantages of LTCC technology are following: chemical inactivity, chemical resistance, biocompatibility and high temperature stability. Moreover, the LTCC tapes can be easily cut into desired form in the way to accomplish both mechanical and electrical function in a single ceramic microsystem. The possibility of integration of fluidic channels, active and passive electronic components, sensors, actuators, MEMS (Micro Electro-Mechanical Systems) devices and package into a one module is the main benefit of the LTCC over the polymer technology. Moreover, the low temperature co-fired ceramics can be bonded with other materials using anodic bonding (LTCC-silicon), microwave plasma (LTCC-polymer) or low temperature glass (LTCC-glass, LTCC-ceramics). Due to all above-mentioned advantages, the LTCC has found practical application in microfluidics as flow sensors, micromixers, micropumps, microvalves, microreactors, microanalyzers, electrochemical sensors, cell sorting and DNA sequencing devices.

In this chapter, the challenges and issues connected with the fabrication process of precise microfluidic components in a multilayer LTCC substrate are discussed. Subsequently, an overview of the techniques for micromachining ~~the~~ of 3D structures in the green (unfired) and fired ceramic material is provided. Low and higher pressure lamination methods, laser

structuration, mechanical punching, hot embossing, photolithographic techniques, sacrificial volume materials are briefly described.

7.2. Laser processing of green ceramic tapes

Laser systems are used in thick-film and LTCC technology mainly for trimming of the passive components, patterning of conductors and cutting of green ceramic material [1-3]. The laser structuring of green ceramic tapes and laminates is commonly used for the fabrication of:

- (1) via holes with the diameter from 50 μm to 300 μm for electrical and thermal interconnections,
- (2) cavities (rectangular openings) for chip integration,
- (3) shapes other than rectangular openings (cantilevers, bridges, seismic masses, thin membranes etc.).

The laser processing of the green ceramic material is a complex subject. The process relies on an interaction between a laser beam and LTCC tape. Such parameters as laser wavelength, beam power, cut speed and frequency play an important role in the laser processing. Practically, the process parameters can vary a lot with the type of green ceramic material, its chemical composition, physical structure and absorption coefficient. Green LTCC tape is a mixture of ceramic particles, glass and organic binder. During processing the ceramic tape is locally heated by a laser beam. In a consequence, the organic binder is ablated from the unfired LTCC material. Simultaneously the not bound ceramic and glass grains are removed [4]. As a result of the laser beam and processed material interaction, the laser output energy is divided into three parts: (i) energy which is transmitted through the material, (ii) energy reflected and (iii) absorbed by the material. The absorbed energy can cause various effects in the material e.g. ionization, lattice vibration, melting, vaporization, thermal and photochemical ablation. Moreover, during the laser processing some by-

products (vapour, debris) are generated which can influence the process. The laser ablation of a material is dependent on absorption and thus (dependent) on the wavelength of the laser radiation. Common wavelengths of industrial lasers are 10600 nm (IR), 1064 nm (NIR), 532 nm (VIS, green), 355 nm (UV). The absorption of laser radiation is furthermore dependent on other factors e.g. temperature, laser pulse width.

Generally laser systems can operate in two modes: continuous wave (CW) and pulsed. The modes of operation describe the laser energy distribution in time (Fig. 7.1). For the CW mode the energy of laser beam is relatively low while for the pulse mode energy of the beam depends on repetition rate, pulse width (duration) and pulse power. All these parameters have a very strong influence on the laser ablation of the green LTCC tape.

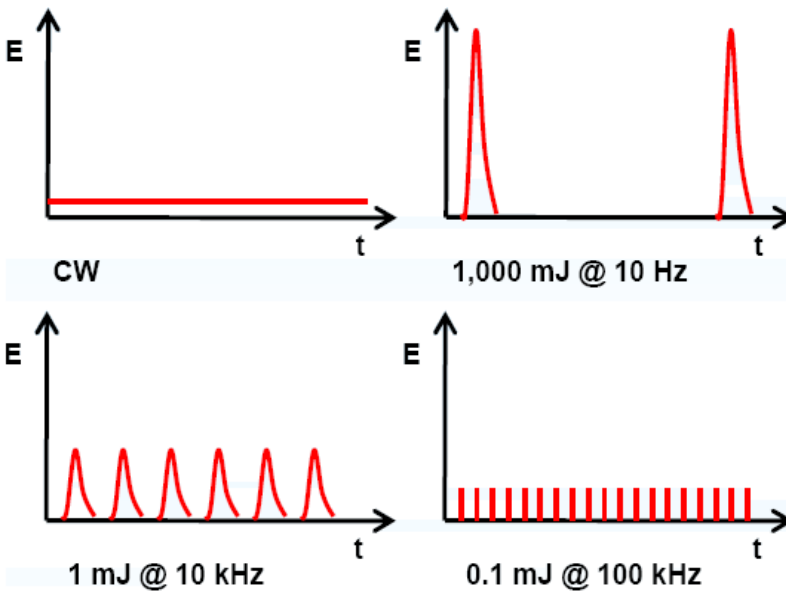


Fig. 7.1. The energy distribution in time for different modes of operation [5].

There are three basic laser structuring techniques: laser cutting, engraving (ablation) and drilling. In the laser cutting method a single or multiple pass

approach can be used. The single pass approach consists in a single cutting cycle at high energy. The laser beam energy should be sufficient to cut the green ceramic tape through. In opposite to the single pass approach the multiple pass approach consists in repeated cutting cycles at lower energy (higher laser beam speed). Each approach leads to different results. On a one hand the single cutting cycle is a bit faster. On the other hand the multi-pass approach leads to thinner cutting kerfs and better cutting quality. However, the heat accumulated during the multiple cutting cycles can caused melting of the glass phase in the LTCC tape. This phenomenon is especially visible for thicker tapes. Exemplary kerfs made with the use of a single and a multiple pass approach are presented in Fig. 7.2.

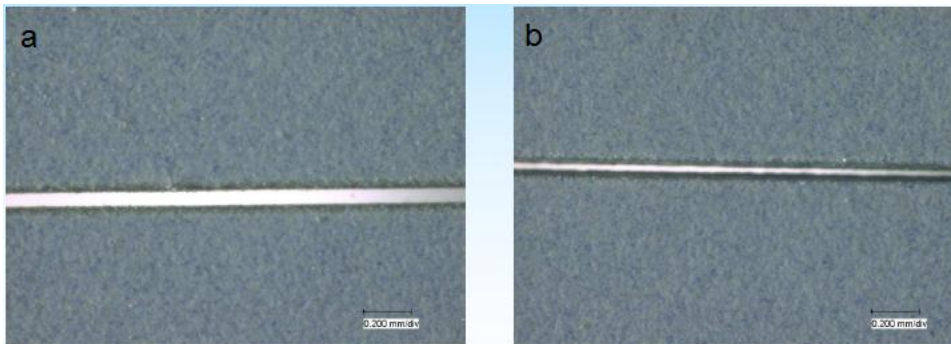


Fig. 7.2. LTCC kerfs obtained by (a) single cutting cycle (1 x 100 mm/s) and (b) multiple cutting cycles (4 x 500 mm/s) [5].

The laser engraving is used for the fabrication of channels, cavities or other structures within a single ceramic tape or a laminate. Energy of the laser beam is adjusted to ablate some of tape material but not to cut it through. The ablation depth depends on the laser energy. Therefore, variations of laser beam scanning speed which results in different energy density absorbed by the engraved material can caused not uniform depth profile of the final

structure. Exemplary channels made in green LTCC tape using the laser engraving technique is presented in Fig. 7.3.

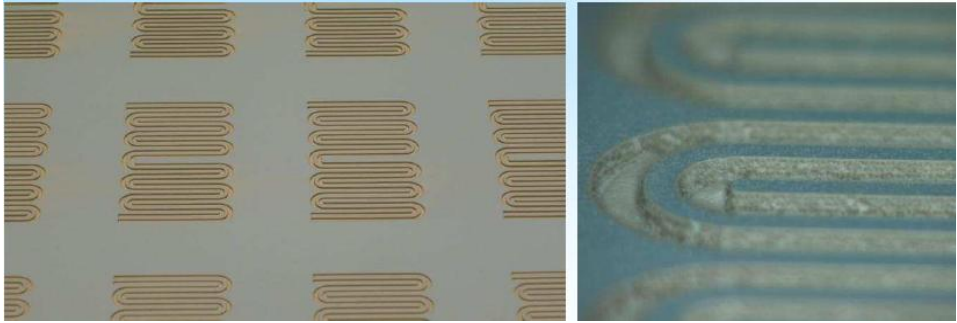


Fig. 7.3. Fluidic channel made in green LTCC tape by laser engraving [5].

The laser drilling is mainly used to fabricate via holes in green ceramic tape for electric and thermal interconnections. The holes can be drilled using two dimensional (trepanning) or three dimensional (helical trepanning) laser beam movement (Fig. 7.4).

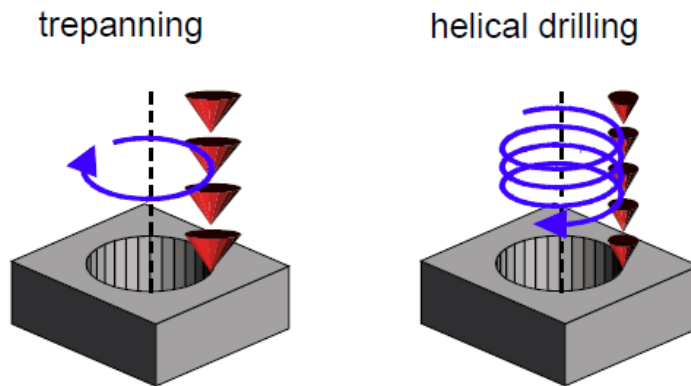


Fig. 7.4. Techniques of vias drilling using laser system.

The laser energy vaporizes the material layer by layer and ultimately creates a through hole. The shape of the drilled hole is defined by the profile of the laser beam. Therefore, the percussion drilled holes are somewhat tapered

(Fig. 7.5). As can be seen in Fig. 7.6 the tapering phenomenon increases with the tape thickness [6].

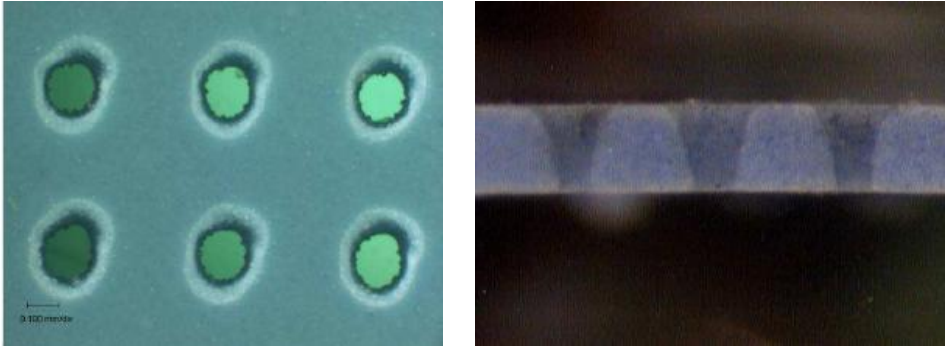


Fig. 7.5. Tapered via holes drilled in a green LTCC tape using CO₂ laser [5].

7.3. Mechanical machining of green ceramic tapes

The mechanical machining methods are used in order to obtain cavities, channels (milling) or vias for electrical and thermal connection (punching) between ceramic layers. The principles of mechanical milling and punching are presented in Figs. 7.7a and 7.7b, respectively.

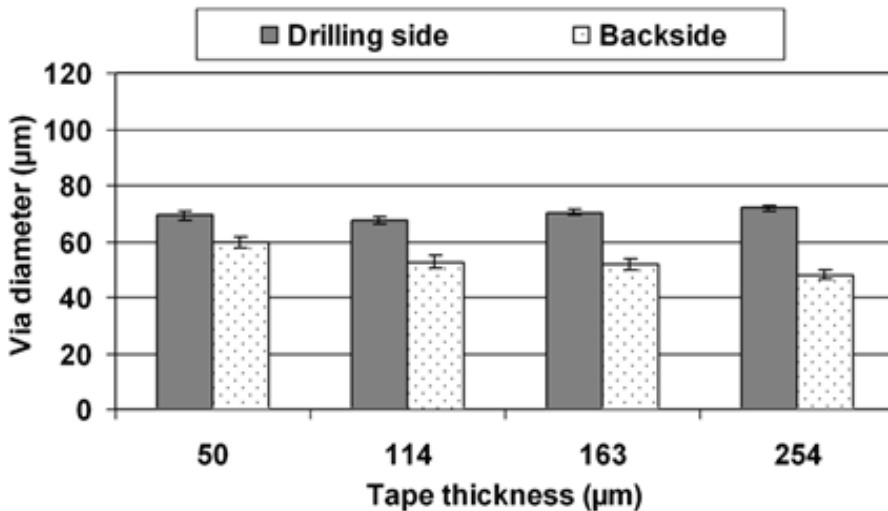


Fig. 7.6. Difference in dimensions of laser-drilled vias [6].

Both mechanical patterning techniques are similar to laser machining. The only difference between mechanical and laser machining is the way of removing the unfired ceramic material. In the case of mechanical milling/punching a piece of LTCC tape is removed due to mechanical interaction between a milling/punching tool and green ceramic material. In the case of mechanical milling it is possible to achieve complex geometries with feature size of 100 μm .

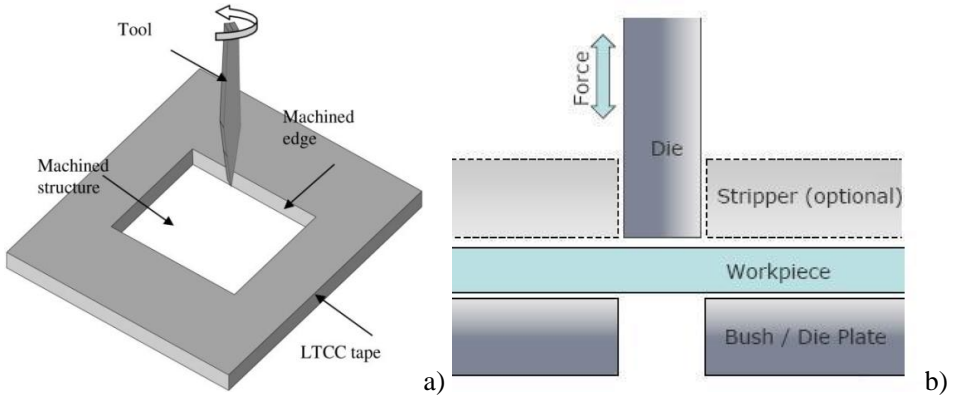


Fig. 7.7. Principles of mechanical milling (a) and punching (b) [7,8].

The quality and size of the final milled feature strongly depends on the applied tool. Mechanical punching is usually carried out with a tool with desired size and a die with an opening typically 12.5 mm larger in diameter than the punch. Exemplary punching tool is presented in Fig. 7.8. An automated punching machine can make from 5 to 500 holes per second, depending on the complexity of the machine. The quality of vias produced by mechanical punching depends on the proper alignment between the punch and the die. If these two components are not well aligned then the via quality decreases and the punching die is likely to be damaged. The advantage of the mechanically punched vias in comparison with the laser drilled ones, is the

lack of the tapering phenomenon. The variation of the via diameter on the punch and back side of the tape is presented in Fig. 7.9.

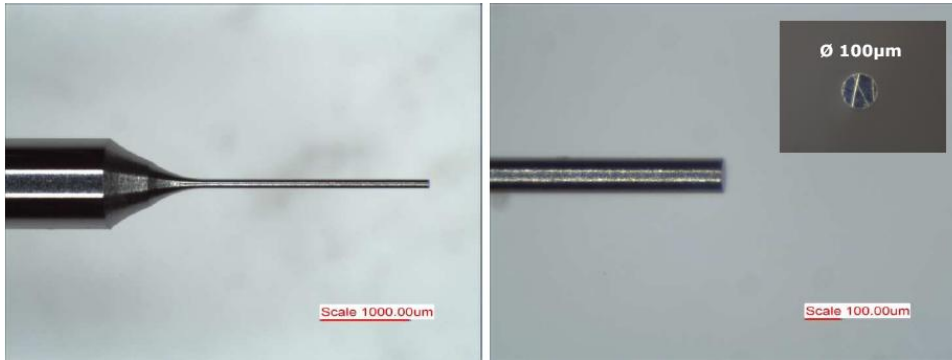


Fig. 7.8. Punching tool [8].

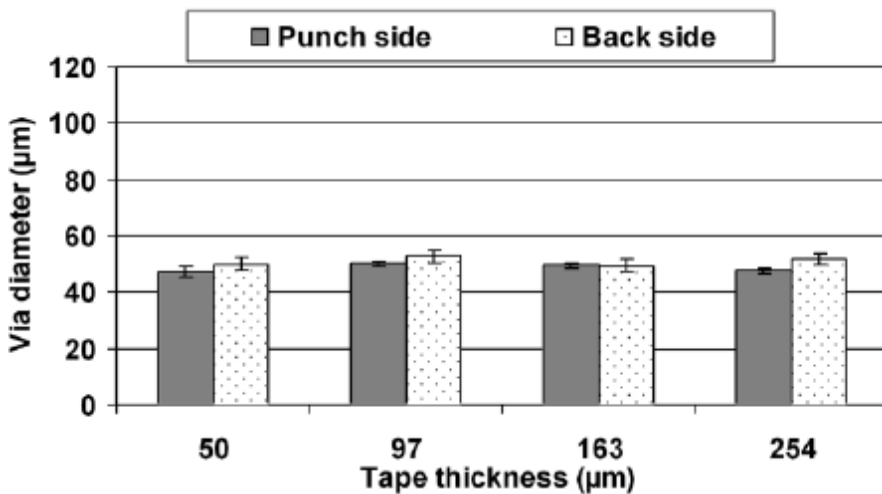


Fig. 7.9. Difference in dimensions of mechanically punched vias [6].

7.4. Hot embossing

The hot embossing is an alternative method for fluidic structures fabrication in unfired ceramic substrate. Originally this method was applied to form complex spatial structures in polymeric materials. In this technique the

pattern which consists of various geometries is transferred to the surface of the green ceramic laminate. A flow-chart of the LTCC module three-dimensional structuration using hot embossing is presented in Fig. 7.10.

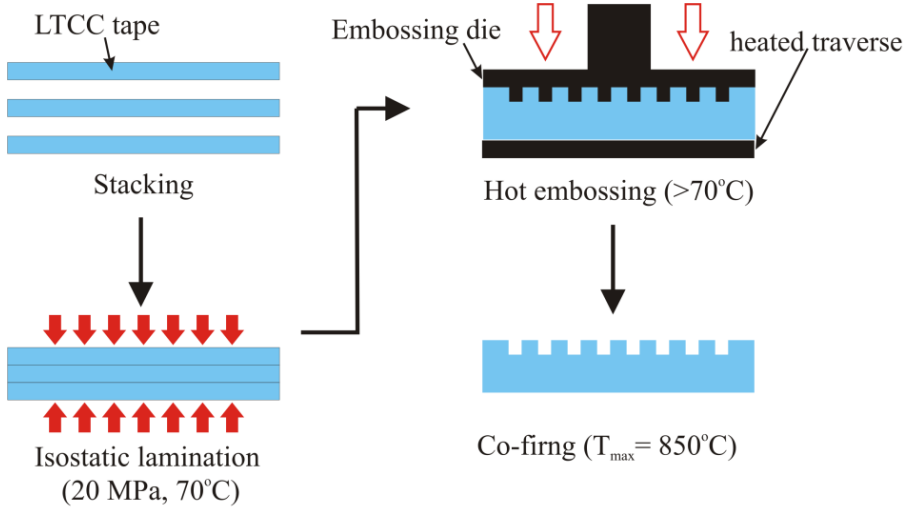


Fig. 7.10. Three-dimensional structuration of LTCC substrate using hot embossing.

In the first step, few ceramic sheets are laminated using an isostatic or uniaxial press in order to form a ceramic substrate. Then the LTCC laminate is put on a heated traverse. The ceramic module and embossing die are heated above glass transition temperature of the organic binder (typically $> 70^{\circ}\text{C}$). In the next step, the embossing die is driven down, impressing the pattern into ceramic laminate. Hot embossing dies can be made of various materials such as: polymers (PMMA), rubber, nickel, brass. The pattern is manufactured using lithography, electroplating, LIGA (ger. Lithographie, Galvanoformung, Abformung) technology, ultra-precision milling or laser ablation techniques [9, 10]. Exemplary embossing dies are presented in Fig. 7.11.

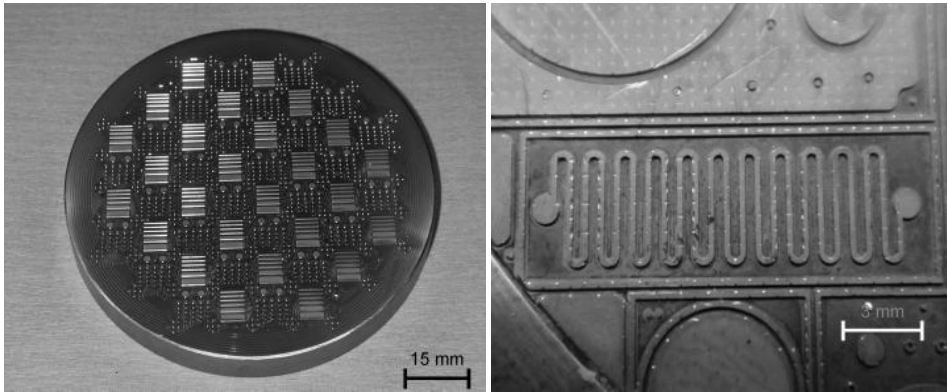


Fig. 7.11. Embossing die made of brass [9].

The crucial parameters of an embossing process are: temperature, pressure, time and material of the mould pattern. The depth of the impressed shape can be increased by rising pressure and temperature of the process. However, too high embossing temperature can cause sticking of the "green" ceramic material to the die, whereas too low temperature may result in cracking. Moreover, high embossing pressure may induce cracks and fractures in the ceramic substrate. Therefore, embossing parameters feed rate, pressure, maximum temperature, and dwell time have to be optimized depending on the properties of the specific LTCC tape [10]. A green ceramic laminate with a structured surface with embossing die is presented in Fig. 7.12. Buried fluidic structures can be fabricated using hot embossing method, as well. However, uniaxial or isostatic lamination cannot be applied to bond structured laminate and ceramic cover tape. Therefore, a low pressure lamination method has to be used. The LTCC substrate with embossed structures can be joined with ceramic cover tape using special adhesive layer (Fig. 7.13). The ceramic laminate is covered by a mixture of polypropylene-glycol (PPG) and ethanol. After that, the embossed laminate and the covering LTCC tape are stacked together and pressed with a steel roller, followed by a storage for 24 h at a/ the temperature of 80°C. The applied solvent dissolves the surface of the

laminate and ceramic cover tape and bond them together. Since then the LTCC layers cannot be separated. In the last step, the ceramic module is co-fired in air in a typical two step thermal profile. During the co-firing process the applied solvent is vaporizing completely leaving no residue.

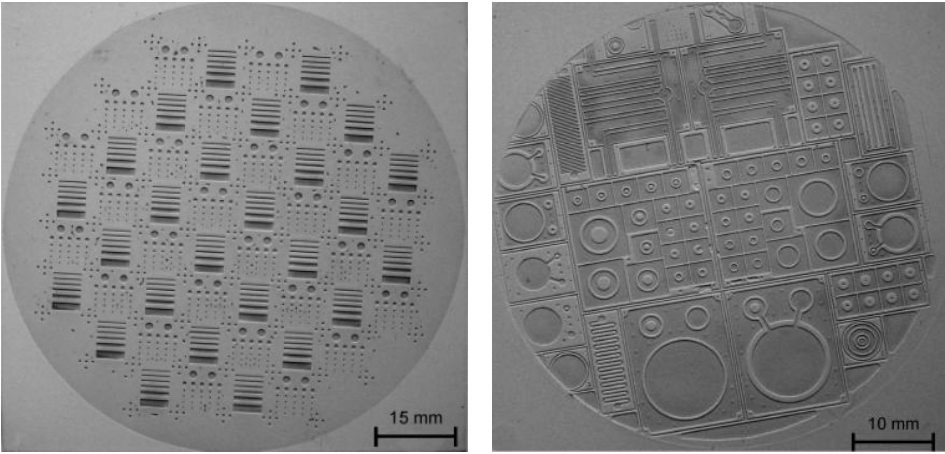


Fig. 7.12. Green laminates with a structured surface produced by hot embossing [9].

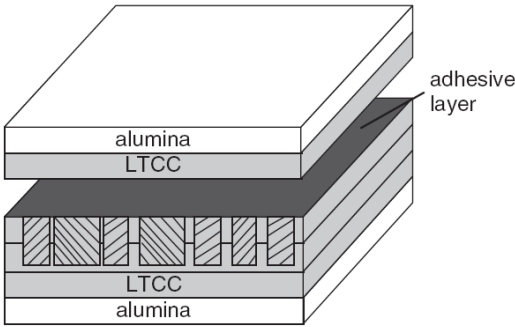


Fig. 7.13. Laminate assembly for preparation of LTCC module with buried cavities [9].

7.5. Jet vapor etching

This method relies on chemical machining of green ceramic tapes. The LTCC material is etched in acetone. Solvent vapor is ejected using collimated jet

through the unfired LTCC layer. The acetone dissolves the organic material and using the fluid flow momentum, simultaneously removes ceramic and glass particles. Using jet vapor etching technique it is possible to achieve fairly rounded holes with a diameter equal to about 25 μm . The processed ceramic tape is undamaged by acetone vapor and can be laminated and co-fired using standard LTCC processing. The system which is used for a jet vapor etching is shown in Fig. 7.14. The tank containing solvent is placed on a hot plate. As a result of solvent heating the vapor pressure is increased. By pumping an inert gas (nitrogen) the solvent is atomized and ejected through a nozzle in the direction of green LTCC sheet. The ejected acetone droplets dissolve the organic binder of the LTCC tape. Simultaneously, the filler grains are removed by the gas mixture momentum. The main disadvantage of this technique is small repeatability of structure dimensions due to poor control of material removal rate [7, 10]. Fig. 7.15 shows the vias fabricated using chemical machining of the LTCC material.

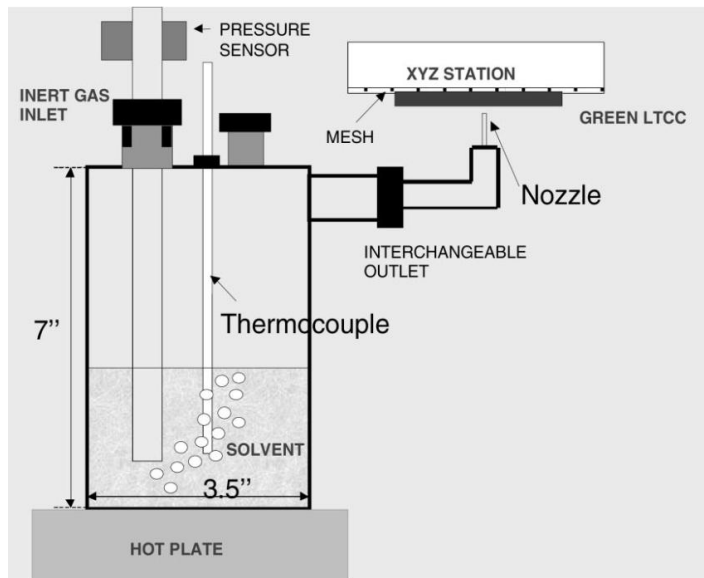


Fig. 7.14. Schematic diagram of the atomized acetone jet reactor [7].

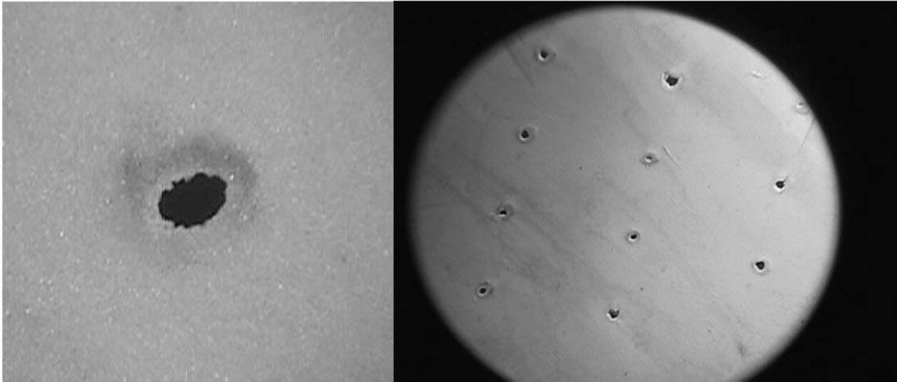


Fig. 7.15. Photograph of LTCC tapes machined with the atomized acetone jet [7].

7.6. Photolithographic patterning

This technique takes advantage of well known silicon lithography. The flow-chart of the photolithographic patterning technique is presented in Fig. 7.16.

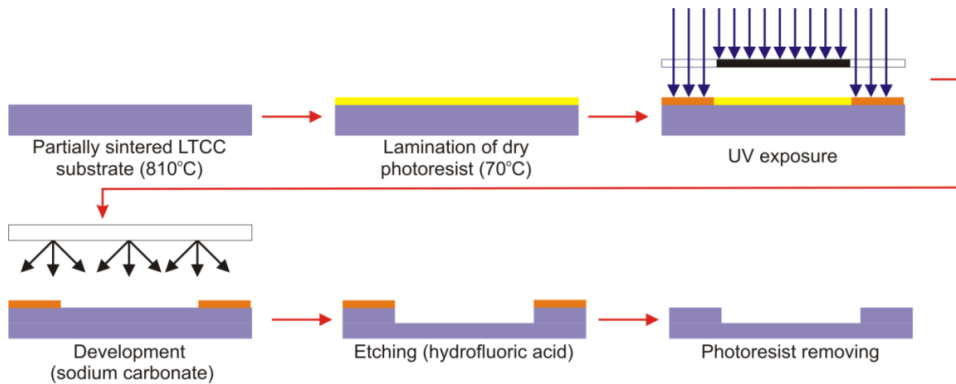


Fig. 7.16. Flow-chart of the photolithographic patterning process.

The process consists of few steps. First, the ceramic laminate is prepared according to the standard technological process, however, the laminate is sintered at a temperature lower than the peak firing temperature (810°C). In the next step, a dry negative photoresist is laminated at 70°C with a partially

co-fired ceramic substrate. With the contact UV photolithography a/the pattern is transferred from the mask to the surface of the LTCC module. The photoresist is developed using sodium carbonate. After the developing the non-masked area of partially sintered ceramics is etched using hydrofluoric acid (HF). The etching rate of the partially sintered LTCC material in diluted HF and ammonium fluoride : HF buffer mixture is presented in Fig. 7.17. The etching rate in diluted hydrofluoric acid is larger than that of buffer mixture even when temperature and concentration of HF in the buffer mixture are higher. A partially sintered LTCC contains open pores into which the etching agent diffuses and etches glass grains. Examples of patterns fabricated using photolithographic method are presented in Fig. 7.18. The photolithographic patterning gives the possibility to achieve features smaller than 10 μm.

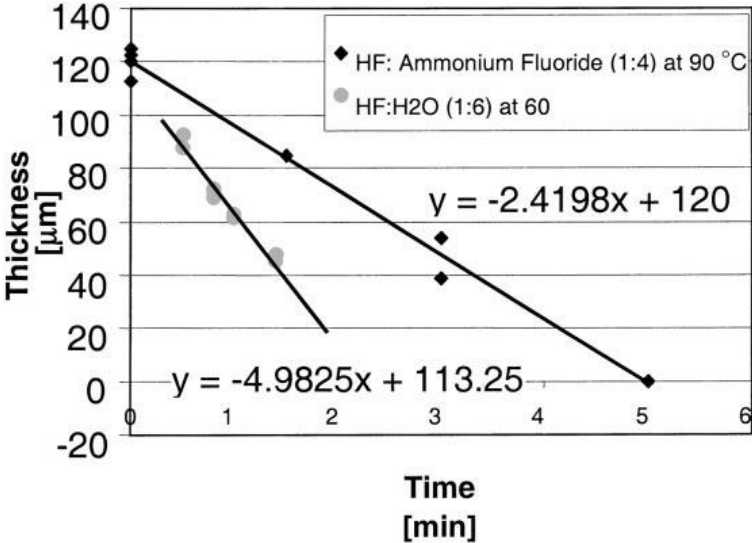


Fig. 7.17. Etching rate of partially sintered LTCC tape [7].

7.7. Photoformable LTCC tapes

Photosensitive ceramic tapes can be used as an alternative for photolithographic patterning. This technique utilizes specially prepared

LTCC tape. Composition of the photoformable ceramic tape is similar to a standard LTCC tape, however, the photoformable ceramics incorporates, besides the plasticizers and anifloculants, a photopolymer in the organic binder. The processing sequence for the photoformable ceramic tape is depicted in Fig. 7.19.

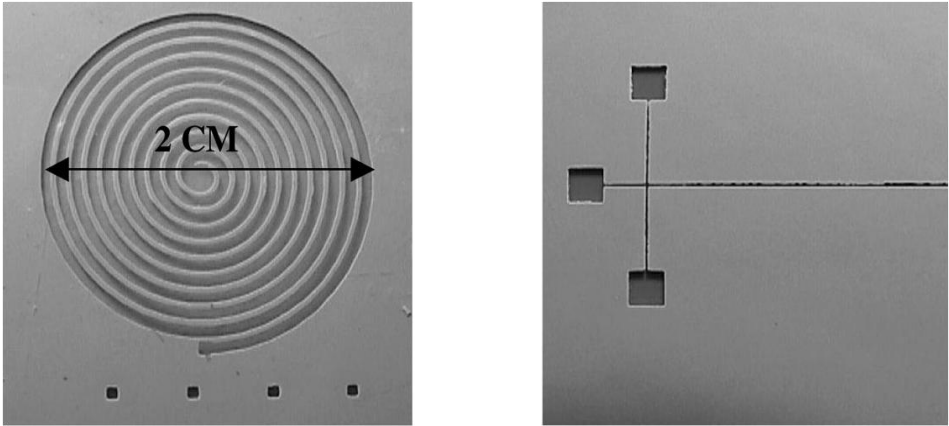


Fig. 7.18. Patterns fabricated using a/the photolithographic method [7].

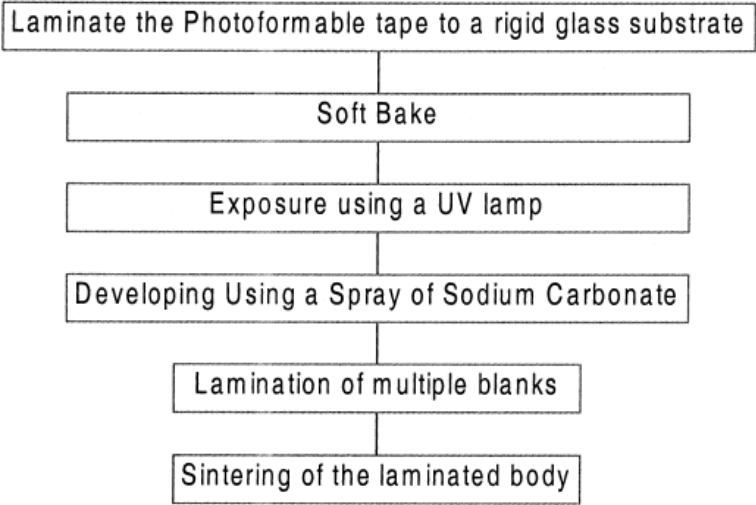


Fig. 7.19. Process sequence for photosensitive LTCC tape [7].

It consists of few steps. First the photosensitive LTCC tape is laminated to a rigid glass substrate and baked. Next the tape is exposed to UV light using contact photolithography. After exposure to UV light, a sodium carbonate solution is used to remove the unexposed surface area. The depth of etching can be easily controlled by modifying the development process parameters like sodium carbonate jet pressure and developing time. The influence of the sodium carbonate jet pressure and development time on the etching rate of the photoformable LTCC tape is presented in Fig. 7.20.

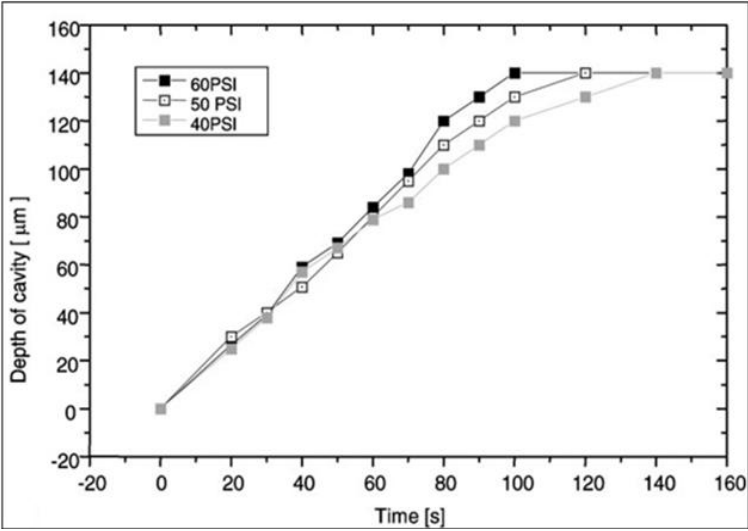


Fig. 7.20. Depth of cavity vs. development time and sodium carbonate jet pressure (PSI -Pound per square inch, 1 PSI = 6894 Pa) [7].

After etching the ceramic tape can be laminated and co-fired. This techniques allows one to achieve feature sizes smaller than 30 µm. Exemplary pattern made in photosensitive LTCC tape is presented in Fig. 7.21.

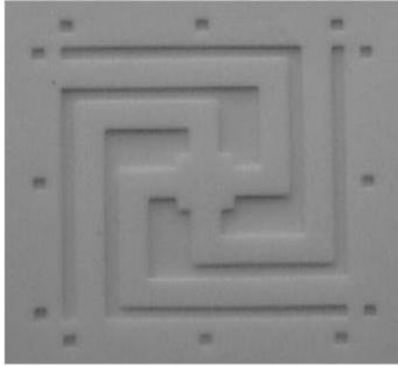


Fig. 7.21. Exemplary pattern fabricated in photoformable LTCC tape [7].

7.8. Sacrificial volume material

Enclosed unfilled volumes (chambers, cavities, channels etc.) can be fabricated in a single green LTCC tape or laminate using one of the above-mentioned structuration techniques. However, the conventional high pressure lamination methods (thermo-compression) pose some problems for defining such volumes. High pressure and temperature of the isostatic or uniaxial lamination strongly affect the geometry of the final spatial structure and preclude realization of complex three-dimensional features such as: channels, cavities, membranes etc. Deformations of the spatial structures can be reduced by applying conventional thermo-compression lamination in conjunction with a special filler material (sacrificial volume material, SVM). This material is a temporary insert which supports and/or defines spatial structure during high pressure lamination process. As the SVMs different types of substances can be applied: wax, graphite-based layers, polymers and mineral materials. Depending on the applied sacrificial volume material its elimination from the LTCC module takes place either by dissociation during burnout and sintering (polymers, graphite-based layers) or by etching or pouring out after firing (mineral materials). In the methods which are based on the applying of SVM inserts, the fluidic structures are fabricated using two

common techniques: "define and fill" and "collate and laminate". A flow-chart of the "define and fill" technique is presented in Fig. 7.22. In a "define and fill" [12, 13] technique a microchannel is first created by laser cutting or mechanical milling in the middle layer. The cutting process is followed by an initial lamination of the middle and bottom layers in an isostatic or uniaxial press at a relatively low pressure of about 1 MPa, at room temperature. In the next step, the created microchannel is filled with a sacrificial volume material and can be sealed by the upper layer (Fig. 7.22b).

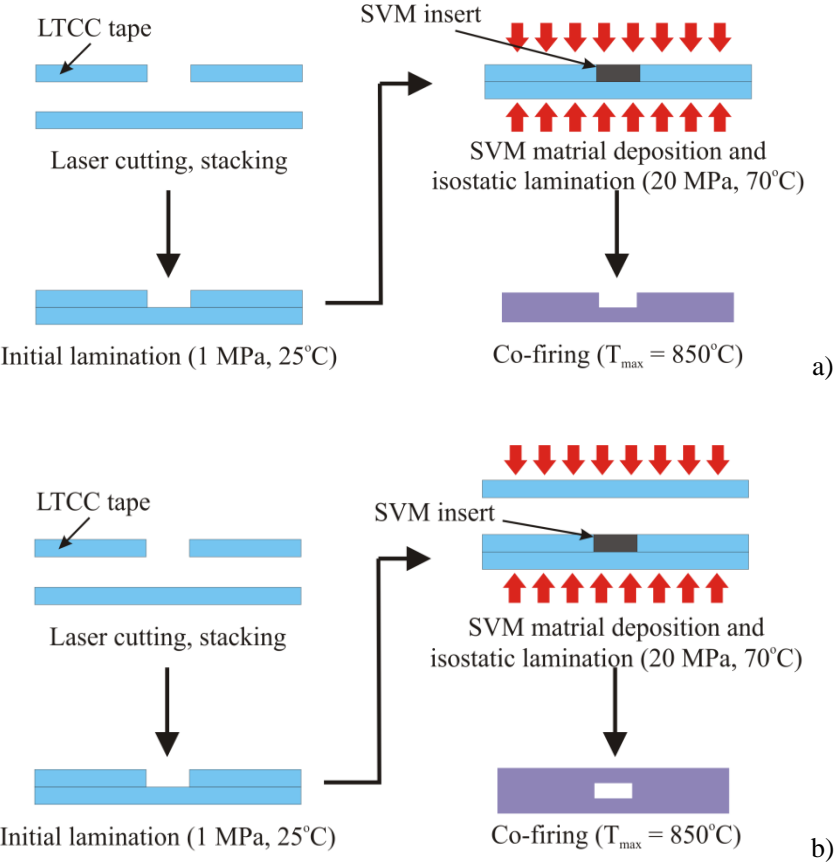


Fig. 7.22. Fabrication of (a) surface and (b) buried channels in LTCC module using "define and fill" process.

The SVM is a discrete layer matching with the opening in the middle tape. The channel is filled in by screen-printing of the SVM paste through mask made in the backing polymer. The sacrificial volume material deposition process is referred to in the literature as a screeding. The SVM paste screeding process is presented in Fig. 7.23.

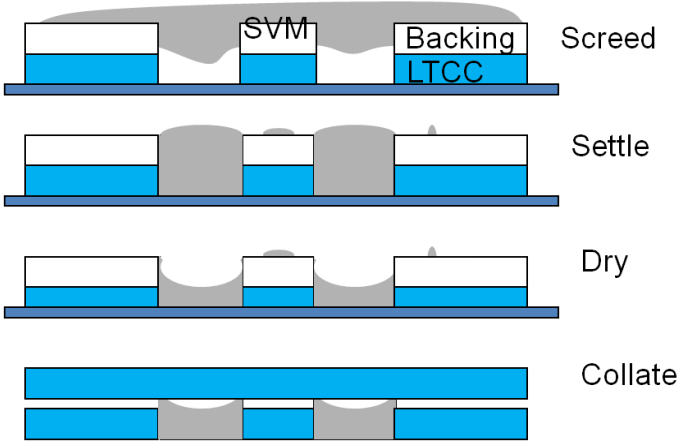


Fig. 7.23. Screeding process of the SVM paste [14].

The backing polymer with punched or cut openings is used as a mask and a screen-printer’s squeegee fills the channel with SVM paste. Application of the backing polymer as a form decreases the number of the process steps because there is no need to make a stencil or pattern on the screen. Moreover, the SVM paste shrinkage after drying and backing the polymer ensures proper thickness of the dried sacrificial insert. Finally, the LTCC module is laminated second time in an isostatic or uniaxial press with standard thermo-compression lamination process parameters. After the lamination the ceramic laminate is co-fired in air. It is recommended to modify the burnout cycle to insure a complete burnout of the applied temporary insert. Commercially available sacrificial volume materials are made of graphite because of its inherent features. Graphite is known to burn away in air above about 600°C,

which is intermediate between the debinding and sintering temperatures of LTCC. It does not react with LTCC and can be easily applied as a thick-film paste or tape. During firing the graphite is removed according to the reaction (7.1):



Ideally, a graphite-based sacrificial volume material should be completely removed below the temperature where the open porosity of LTCC is closed by densification (about 800°C). Therefore, the co-firing thermal profile should be modified by applying a slower ramp rate to 850°C or additional isothermal heating stage for carbon burnout. Misfit thermal profile may lead to swelling or cracking of the LTCC material. Top and cross-sectional views of an embedded cavity fabricated using standard co-firing profile and a co-firing profile with an additional iso-thermal heating for carbon burnout is presented in Fig. 7.24.

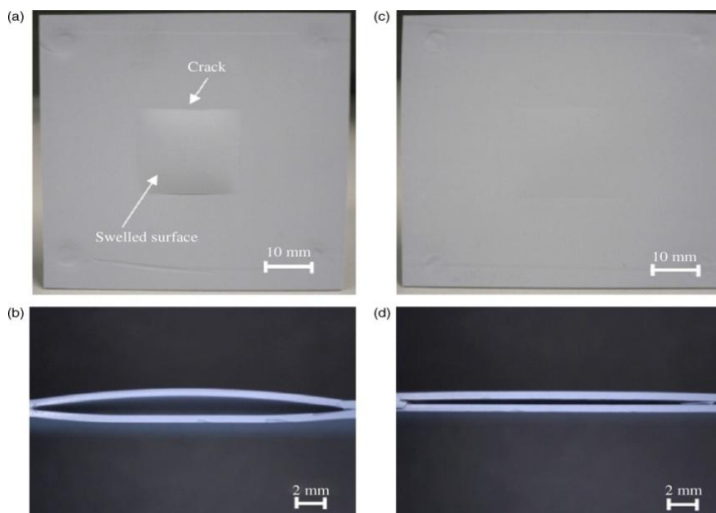


Fig. 7.24. Top and cross-sectional views of an embedded cavity fabricated using: (a, b) a standard co-firing profile and (c, d) a co-firing profile with an additional isothermal heating cycle [10].

Scanning electron microscope (SEM) image of the channels fabricated using "define and fill" method are presented in Fig. 7.25.

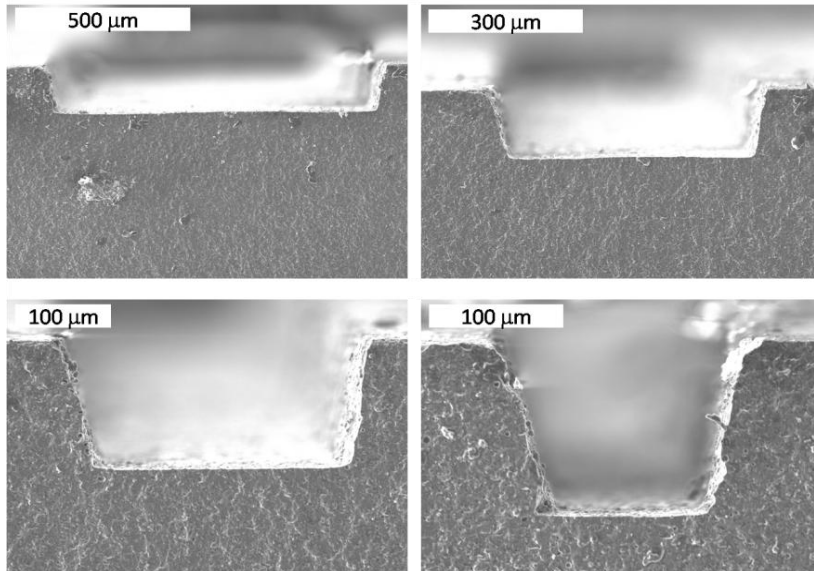


Fig. 7.25. Channels made in LTCC substrate using "define and fill" technique [15].

Alternative "collate and laminate" technique for the fluidic structures fabrication in LTCC substrates using SVM is presented in Fig. 7.26. First, a sacrificial insert is placed on the surface of an unfired ceramic tape. Then, an LTCC sheet with deposited SVM is collated with another ceramic layer by isostatic or uniaxial lamination. In this method the microchannel is formed during high pressure lamination by deformation of the "green" ceramic tape around the sacrificial material and the resulting bonding of compatible areas without the use of pre-existing cavity [16]. Scanning electron microscope image of the channels fabricated using the "collate and laminate" method is presented in Fig. 7.27.

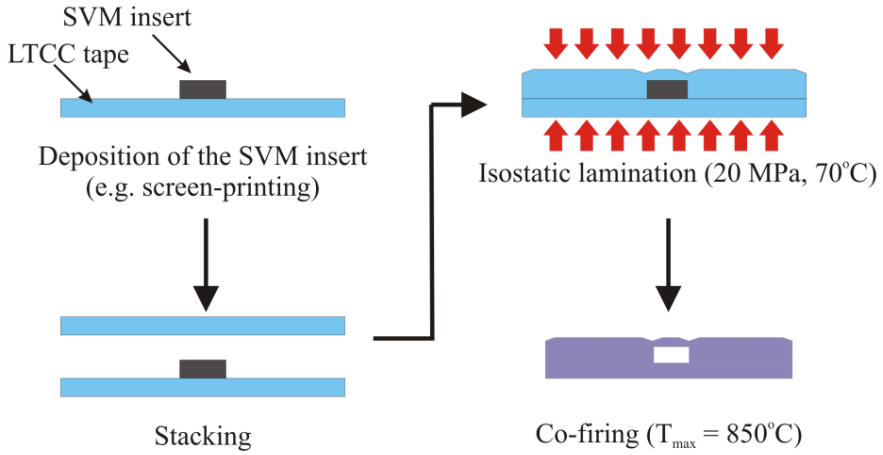


Fig. 7.26. A flow-chart of the "collate and laminate" technique.

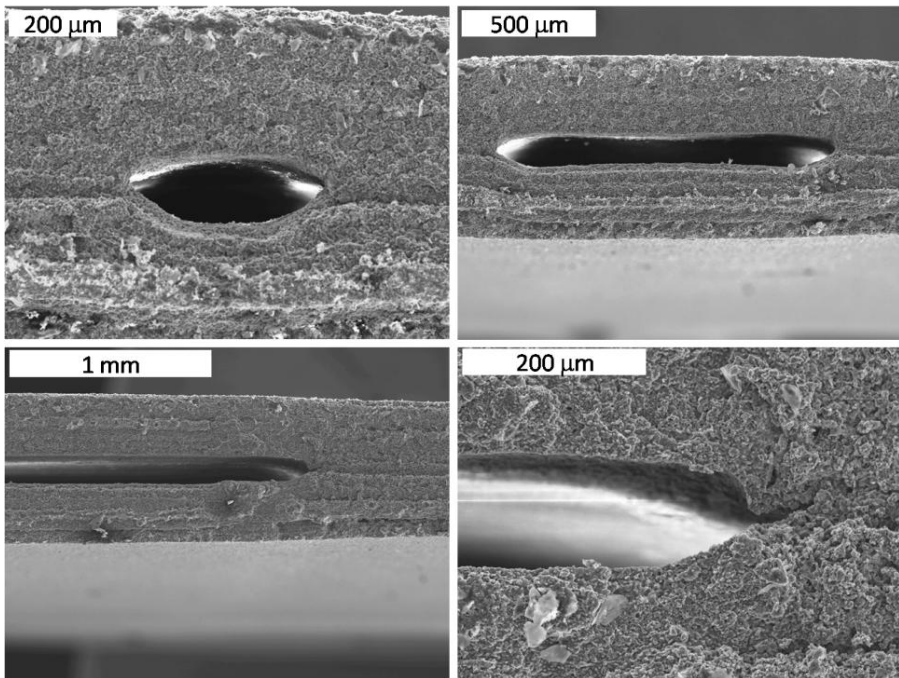


Fig. 7.27. Channels made in LTCC substrate using "collate and laminate" technique [15].

Other structures that can be made using a combination of unfired LTCC tape, sacrificial volume material and high pressure lamination are presented in Fig. 7.28.

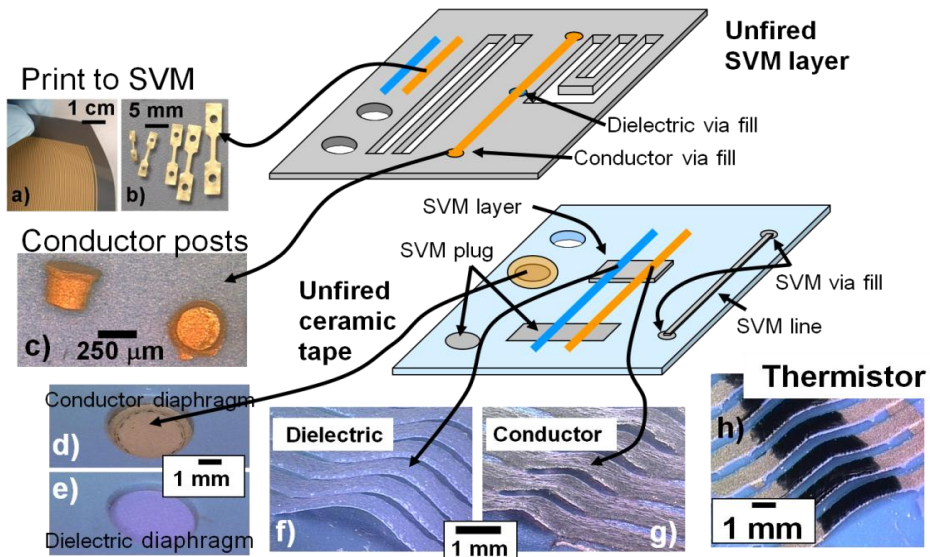


Fig. 7.28. Structures resulting from SVM incorporation in LTCC [14].

By printing thick film pastes onto SVM which is removed during firing it is possible to manufacture tensile bars (Fig. 7.28a and 7.28b), conductors posts (Fig. 7.28c), membranes (Fig. 7.28d and 7.28e) and suspended thick film features (Fig. 7.28f-h). "Define and fill" and "collate and laminate" techniques allow one to fabricate spatial structures with the feature size from 100 μm to a few centimetres in a LTCC substrate.

7.9. Low pressure lamination methods

The thermo-compression is commonly used for laminating "green" ceramic tapes. In this technique ceramic layers are stacked and pressed with a high pressure (5 –30 MPa) at elevated temperature (25–90°C) for 1–20 minutes.

The temperature of the process should be set above glass transition point of the ceramic tape's organic binder. In order to achieve a homogeneous junction between "green" ceramic sheets it is crucial to ensure good interpenetration of the glass/ceramic particles. Appropriate ratio of glass/ceramic particles to organic binder facilitate interpenetration of the particles between ceramic tapes, leading to defect-free homogeneous body [17]. The thermo-compression lamination results in strong bonding, allowing good encapsulation of LTCC structures. However, the high pressure and temperature may affect the geometry of the fluidic structures and damage the final device. In order to avoid deformations of the spatial structures a special low pressure lamination methods have been developed. In contrast to a standard thermo-compression lamination process in a progressive lamination process each ceramic layer is individually laminated with an isostaic or uniaxial press to the previous layer to assure a good bond between the individual LTCC tapes (Fig. 7.29). Thanks to applying the progressive lamination it is possible to reduce pressure of the process (below 7 MPa). It was proven that this value of pressure is adequate to bond ceramic tapes together, prevent layers separation and avoid the deformation of the spatial structures that could occur at standard lamination pressure [18].

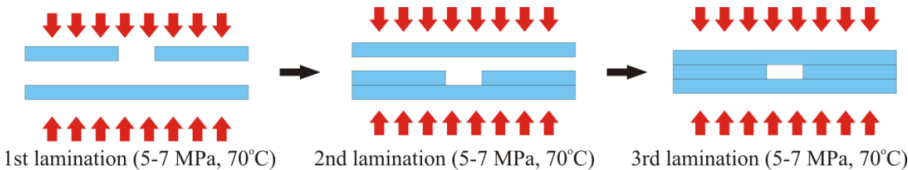


Fig. 7.29. Principle of the progressive lamination process.

Cold low pressure lamination (CLPL) is an advanced method of green ceramic tapes joining. In contrast to previously described thermo-compression technique, in which the junction is produced at elevated

temperature and pressure, the CLPL method allows bonding the ceramic sheets at room temperature under very low pressure [17, 19]. In this technique the green ceramic tapes are joined together using a special double-sided adhesive tape. The adhesive tape is composed of acrylate adhesive and a carrier film made of polyethyleneterephthalate (PET). The CLPL lamination procedure is presented in Fig. 7.30.

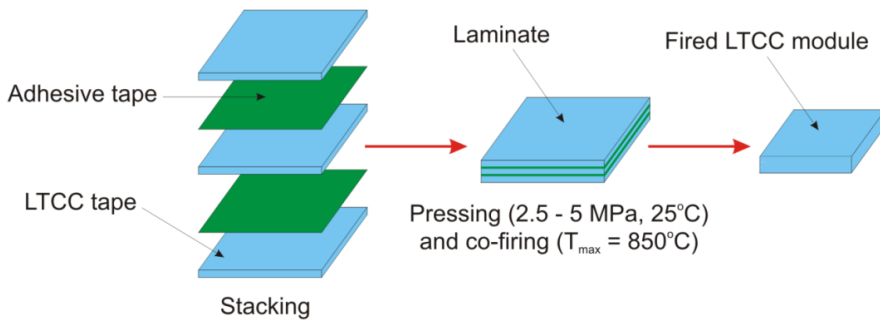


Fig. 7.30. Fabrication of a three layer laminate using CLPL lamination method.

In the first step, the double adhesive layer is applied on the surface of the ceramic tapes. The adhesive tape stripes are rolled onto the sample with a rubber roll. Next, the ceramic tapes and adhesive layers are stacked together and pressed with the pressure of 2.5 – 5 MPa at room temperature. In the last step, the ceramic laminate is co-fired. During the co-firing process the adhesive tape melts and diffuses into the pores of the ceramic material. The melt flow through the smallest pores is driven by capillary forces. Due to the capillary actions the melt flow creates a drag on ceramic tapes, causing interpenetration and homogeneous body. Fig. 7.31 presents a model of this process proposed by Roosen *et al.* The cold low pressure lamination technique is suitable to join non-metalized and metalized ceramic tapes. Comparison between the LTCC structures laminated with and without the adhesive tapes is presented in Fig. 7.32.

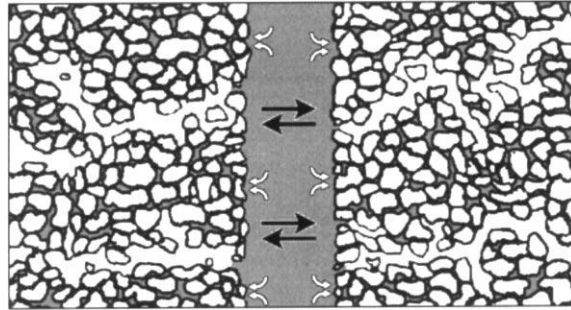


Fig. 7.31. A model of the melt flow through the smallest pores causing the LTCC layers to approach each other. The white arrows indicate the flux of the PET melt, while the black arrows represent the approach of the LTCC layers towards each other [17].

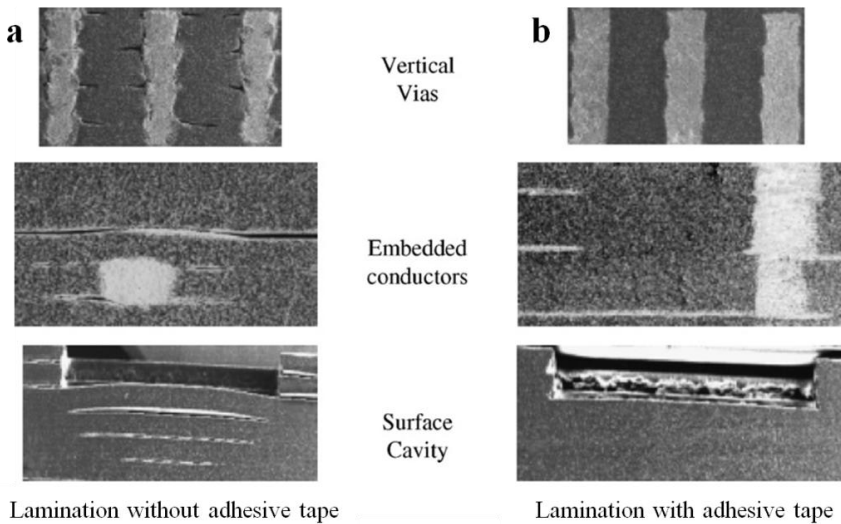


Fig. 7.32. Comparison between multilayer LTCC structures laminated (a) with and (b) without adhesive tapes [20].

Cold chemical lamination (CCL) is a solvent-based method of green ceramic layers joining [21]. The CCL lamination procedure is presented in Fig. 7.33. The CCL technique is similar to previously presented CLPL lamination

method. The difference between the cold chemical lamination and cold low pressure lamination is that the ceramic tape is covered by a thin film of a solvent instead of an adhesive layer. The solvent is deposited on the surface of the LTCC tape using a paint brush or standard screen-printing method. After deposition of the solvent the ceramic sheets are stacked together and pressed with a very low pressure of 0.5 MPa at room temperature.

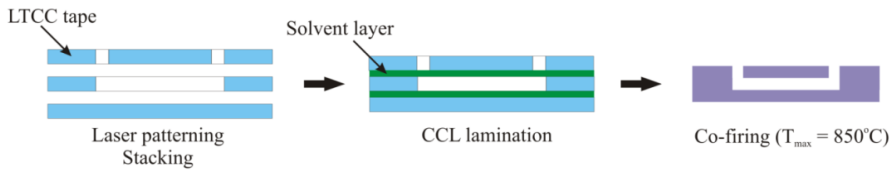


Fig. 7.33. Fabrication of a LTCC-based fluidic structure using CCL lamination method

The applied solvent dissolves the surface of the two adjacent ceramic tapes and bonds them together. Since then the LTCC layers cannot be separated. In the last step, the ceramic module is co-fired in air in a typical two step thermal profile. During the co-firing process the applied solvent is vaporising completely leaving no residue. In comparison with the standard thermo-compression method the CCL technique causes less deformation during the lamination process. It permits us to achieve fine fluidic structures (channels, cavities etc.). Exemplary channels fabricated in LTCC substrate using the CCL methods are presented in Fig. 7.34.

However, this method has three main disadvantages [22]: (i) it cannot be applied to fabrication of precise spatial structures ($\sim 50 \mu\text{m}$) due to the etching of green ceramic tapes during lamination, (ii) solvent that works for one particular LTCC system might not be suitable for another LTCC material,

(iii) the applied solvent may affect the final electrical properties of the screen-printed conductors and passives [23].

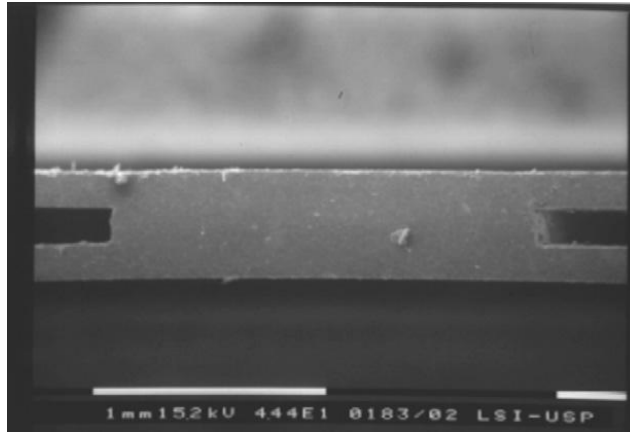


Fig. 7.34. Embedded channels fabricated in LTCC module using CCL method [21].

References

- [1] Smetana W, Balluch B, Stangl G, Lüftl S, Seidler S, Processing procedures for the realization of fine structured channel arrays and bridging elements by LTCC-technology, *Microelectronics Reliability*, 49 (2009) 592-599.
- [2] Nowak KM, Baker HJ, Hall DR, Cold processing of green state LTCC with CO₂ laser, *Applied Physics A, Material Science and Processing*, 84 (2006) 267-270.
- [3] Nowak D, Miś E, Dziedzic A, Kita J, Fabrication and electrical properties of laser-shaped thick-film and LTCC microresistors, *Microelectronics Reliability*, 49 (2009) 600-606.
- [4] Kita J, Dziedzic A, Golonka LJ, Zawada T, Laser treatment of LTCC for 3D structures and elements fabrication, *Microelectronics International*, 19 (2002) 14-18.

- [5] Hagen G, Laser processing of ceramic green tape, Workshop on tape 3D structuring, Orbassano-Turin (Italy), November 2010.
- [6] Wang G, Folk EC, Barlow F, Elshabini A, Fabrication of microvias for multilayer LTCC substrates, *IEEE Transactions on Electronics Packaging Manufacturing*, 29 (2006) 32-41.
- [7] Gongora-Rubio MR, Espinoza-Vallejos P, Sola-Laguna L, Santiago-Avilés JJ, Overview of low temperature co-fired ceramics tape technology for meso-system technology (MsST), *Sensors and Actuators A: Physical*, 89 (2001) 222-241.
- [8] Zeilmann C, Punching technology, Workshop on tape 3D structuring, Orbassano-Turin (Italy), November 2010.
- [9] Rabe T, Kuchenbecker P, Schulz B, Schmidt M, Hot embossing: an alternative method to produce cavities in ceramic multilayer, *International Journal of Applied Ceramic Technology*, 4 (2007), 38-46.
- [10] Khoong LE, Tan YM, Lam YC, Overview on fabrication of three-dimensional structures in multi-layer ceramic substrate, *Journal of the European Ceramic Society*, (30) 2010 1973-1987.
- [11] Andrijasevic D, Smetana W, Zehetner J, Zoppel S, Brenner W, Aspects of micro structuring low temperature co-fired ceramic (LTCC) for realisation complex 3D objects by embossing. *Microelectronic engineering*, 84 (2007) 1198-1201.
- [12] Malecha K, Golonka LJ, Microchannel fabrication process in LTCC ceramics. *Microelectronics Reliability*, 48 (2008) 866-871.
- [13] Malecha K, Golonka LJ, Three-dimensional structuration of zero-shrinkage LTCC ceramics for microfluidic applications, *Microelectronics Reliability*, 49 (2009) 585-591.
- [14] Peterson KA, Knudson RT, Garcia EJ, Patel KD, Okandan M, Ho CK, James CD, Rohde SB, Rohrer BR, Smith F, Zawicki LR, Wroblewski

- BD, LTCC in microelectronics, microsystems and sensors, Proc. 15th IEEE International Conference MIXDES, Poznań (Poland), June 2008, 23-37.
- [15] Malecha K, Maeder T, Jacq C, Ryser P, Structuration of the low temperature co-fired ceramics (LTCC) using novel sacrificial paste with PVA-propylene glycol-glycerol-water vehicle, *Microelectronics Reliability*, 51 (2011) 805-811.
- [16] Peterson KA, Patel KD, Ho CK, Rohde SB, Nordquist CD, Walker CA, Wroblewski BD, Okandan M, Novel microsystem applications with new techniques in low-temperature co-fired ceramics, *International Journal of Applied Ceramic Technology*, 2 (2005) 345-363.
- [17] Piwonski M, Roosen A, Low pressure lamination of ceramic green tapes by gluing at room temperature, *Journal of the European Ceramic Society*, 19 (1999) 263-270.
- [18] Barlow F, Wood J, Elshabini A, Stephens EF, Feeler R, Kenner G, Junghans, Fabrication of precise fluidic structures in LTCC, *International Journal of Applied Ceramic Technology*, 6 (2009) 18-23.
- [19] Roosen A, New lamination technique to join ceramic green tapes for the manufacturing of multilayer devices, *Journal of the European Ceramic Society*, 21 (2001) 1993-1996.
- [20] Schindler K, Roosen A, Manufacture of 3D structures by cold low pressure lamination of ceramic green tapes, *Journal of the European Ceramic Society*, 29 (2009) 899-904.
- [21] Jurków D, Roguszczyk H, Golonka L, Cold chemical lamination of ceramic green tapes, *Journal of the European Ceramic Society*, 29 (2009) 703-709.
- [22] Malecha K, Jurków D, Golonka LJ, Comparison of solvent and sacrificial volume material based lamination processes of low

temperature co-fired ceramics (LTCC) tapes, *Journal of Micromechanics and Microengineering*, 19 (2009) 065022.1-065022.10.

- [23] Jurków D, Golonka LJ, Novel cold chemical lamination bonding technique – a simple LTCC thermistor-based flow sensor, *Journal of the European Ceramic Society*, 29 (2009) 1971-1976.

Chapter 8

Bonding techniques of the LTCC with different materials

8.1. Introduction

Low temperature co-fired ceramic technology is hybrid in nature. The LTCC material can be easily bonded with different materials. Developing of the LTCC-silicon [1, 2], LTCC-glass [3, 4], LTCC-polymer (PDMS, polydimethylsiloxane) [5] and LTCC-ceramics bonding technologies has expanded the frontiers of LTCC appliances.

8.2. LTCC-Si

The LTCC ceramics can be bonded with silicon structures using an anodic bonding [6]. The main advantages of the application of LTCC technology for the fabrication of anodic bondable substrates are:

- multi-functionality with 3D interconnected multilayer substrate,
- ceramic multilayer packaging structure with hermetic packaging between Si chip and LTCC,
- reduction of packaging size with direct interconnections between a chip and a package
- use of standard thick film technology,
- possibility of local bonded areas: the size of the bonded area can be controlled by structuring of LTCC surface in green or sintered state,
- Possibility of passive components integration (to move passives from expensive chip area into the LTCC area).

Anodic bonding is a well known process of sealing Si substrate to a plain glass wafer (Pyrex 7740). The process takes place in the voltage range of 400 – 1000 V and at elevated temperature (about 400°C). The anodic bonding process is shown in Fig. 8.1.

A glass wafer is biased negatively while silicon is polarized positively. Sodium cations within, move through the glass wafer to the cathode. In a consequence of the sodium ions transport a depletion layer is forming in the vicinity of the anode. The generated electric field causes the motion of the oxygen anions, which leads to the formation of an oxide layer at the metallic interface. In order to obtain the bonding between silicon and LTCC material three main conditions have to be fulfill:

1. the coefficient of thermal expansion (CTE) of the LTCC substrate must be matched to the CTE of silicon (CTE difference between both materials in the temperature range from 25°C to 400°C should be less than ± 0.2 ppm/K),
2. the LTCC substrate should contain appropriate concentration of the sodium ions (1-2 wt %),
3. the LTCC surface roughness should be less than 100 nm.

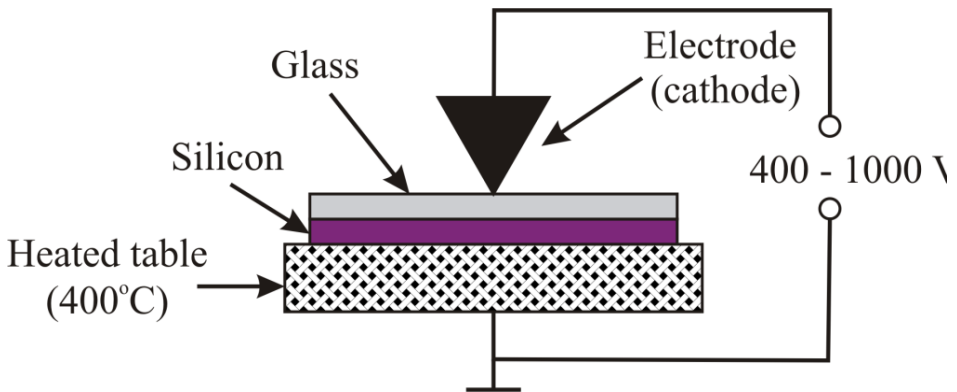


Fig. 8.1. Anodic bonding process.

The commercially available LTCC does not contain the alkali ions necessary for anodic bonding that are indispensable to realize the ionic migration between a silicon wafer and ceramic substrate. However, LTCC can be anodic bonded to silicon through a thin film of bondable screen-printed

glass [1]. The LTCC to Si bonding process through the layer of bondable glass is presented in Fig. 8.2. The main drawback of the applying of screen-printable glass is CTE mismatch between the LTCC and silicon which may cause cracking during the cooling down.

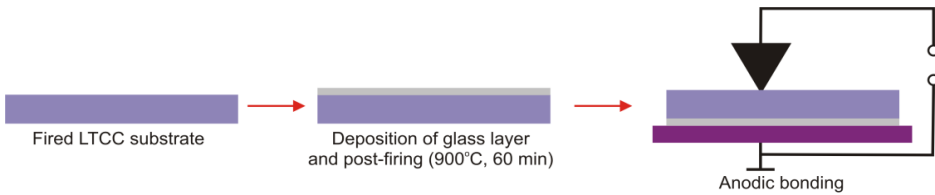


Fig. 8.2. LTCC to silicon bonding process using a bondable glass layer.

Another approach was proposed by German company *VIA Electronics GmbH* [7]. They have developed anodic bondable LTCC green tape system (BGK79). The new LTCC tape is composed of borosilicate glass, alumina and cordierite. This composition has a Na^+ ions content of 1.7 wt%. The CTE of the anodic bondable LTCC material is matched with silicon (Fig. 8.3).

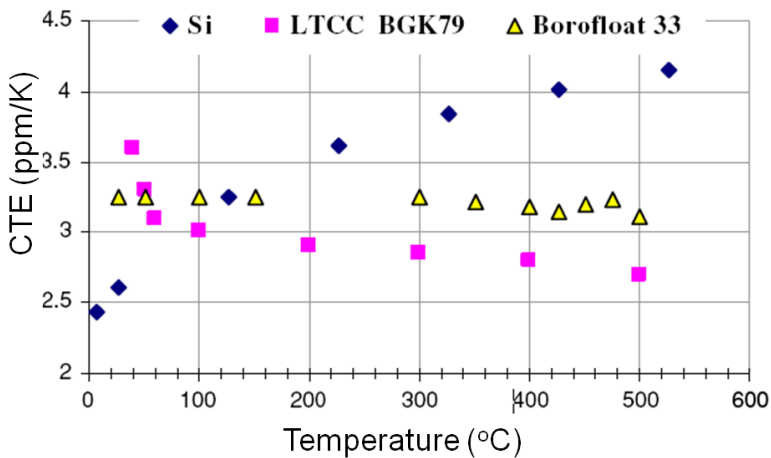


Fig. 8.3. Comparison of CTE for silicon, anodic bondable LTCC (BGK79) and Borofloat glass [7].

However, the LTCC material requires additional polishing step in order to achieve appropriate surface roughness ($< 100 \text{ nm}$) and flatness ($< 5 \mu\text{m}/10 \text{ mm}$). The ceramic tape system developed by *VIA Electronics GmbH* is compatible with Au metallization. Scanning electron microscope image of the LTCC/Si interface is presented in Fig. 8.4. A comparison between both LTCC-Si anodic bonding procedures is given in Table 8.1.

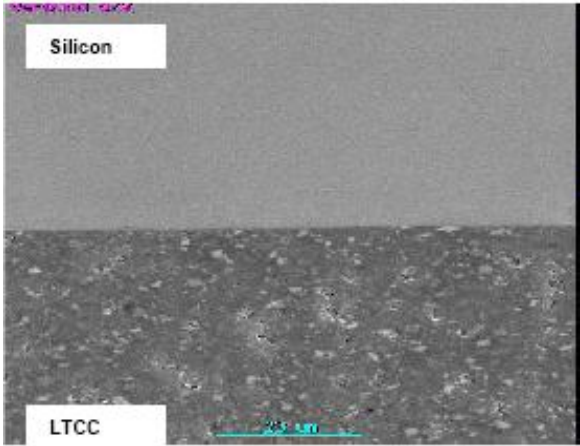


Fig. 8.4. Cross-section of anodically bonded LTCC with silicon (SEM image) [7].

Table 8.1. Comparison between Si-LTCC bonding methods.

Technique	Advantages:	Disadvantages:
LTCC covered with anodic bondable thick-film glass	Compatible with standard thick-film pastes No polishing is required (Ra ~ 20 nm)	Additional screen-printing and post-firing steps LTCC/Si structure may crack during cooling down step (CTE mismatch)
Anodic bondable LTCC material	Compatible with thick-film (Au) metallization system CTE of the LTCC tape matched to CTE of Si No additional printing and firing is required	Additional polishing is required Not compatible with all thick-film metallization systems

8.3. LTCC-glass

A serious limitation of the LTCC-based microsystems is non-transparency of the ceramic material. In many cases it is necessary to observe the phenomena that take place inside the microfluidic system during the operation (such as mixing, colour changing, fluorescence, transport of the particles suspended in the flowing medium). The non-transparent ceramic cover makes this type of investigation impossible. A sapphire glass can be easily integrated with a ceramic structure using the standard LTCC technology [8]. Flow-chart of a sapphire glass to LTCC ceramic bonding process is presented in Fig. 8.5.

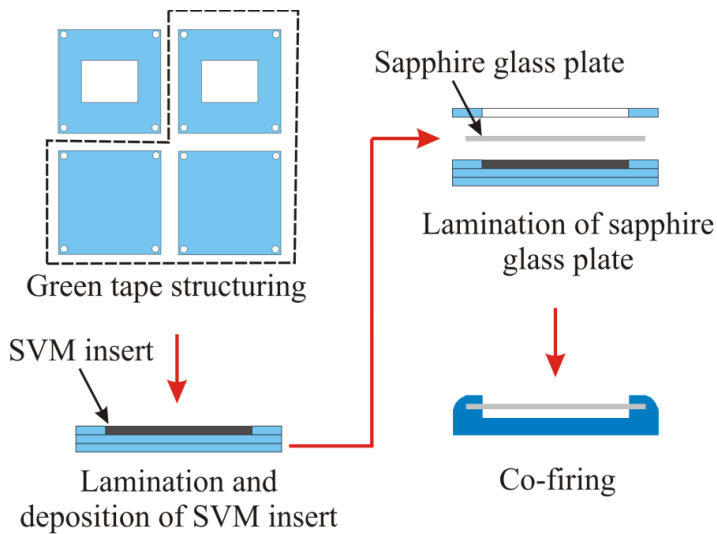


Fig. 8.5. A flow-chart of sapphire glass to LTCC ceramic bonding process.

A glass plate is laminated with LTCC tapes during an isostatic or uniaxial lamination process. The channel placed below the sapphire glass is defined by a SVM insert. After lamination the structure is co-fired in air according to the typical two-step thermal profile. Thanks to matching of the coefficient of thermal expansion of LTCC and sapphire glass the stress induced during the

co-firing process is negligible. The sapphire glass/LTCC based structure is hermetic, it is characterized by helium leakproofness. Exemplary hybrid glass-LTCC structures fabricated using the sapphire glass are presented in Fig. 8.6.

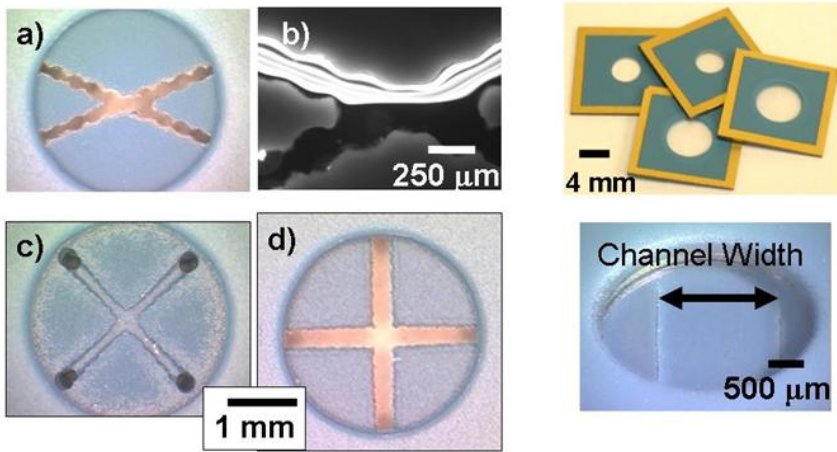


Fig. 8.6. Sapphire glass-LTCC hybrid structures [3].

A slightly different approach was proposed by Bemnowicz *et al* [4]. The technological process flow, presented in Fig. 8.7, is similar to sapphire glass to LTCC ceramic bonding Process, however, the technique does not allow the application of high pressure. The LTCC tapes and glass window have to be initially bonded using a cold low pressure lamination or cold chemical lamination process. A key in this method lies in the application of glass with the softening temperature in the range of 670-720°C. Thanks to this, the glass plate becomes soft during the co-firing process before the LTCC shrinkage starts. The surface tension of the liquid glass membrane is sufficient to balance the gravity force. The surface tension force holds the soft glass membrane spread over the fluidic structure. As the temperature decreases the glass membrane vitrification is initiated and a dense and transparent material

arises. It was shown that this method enables fabrication of transparent windows in LTCC modules with the diameter up to 15 mm. The main drawback of this method is sagging of the glass window. The sagging phenomenon rises with increasing the window diameter (Fig. 8.8). Exemplary LTCC structures with an integrated sodium glass window is presented in Fig. 8.9.

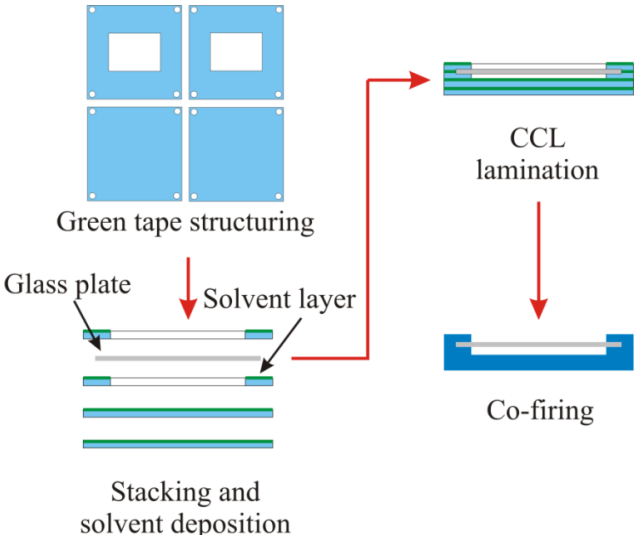


Fig. 8.7. A flow-chart of glass to LTCC ceramic bonding process using CCL method.

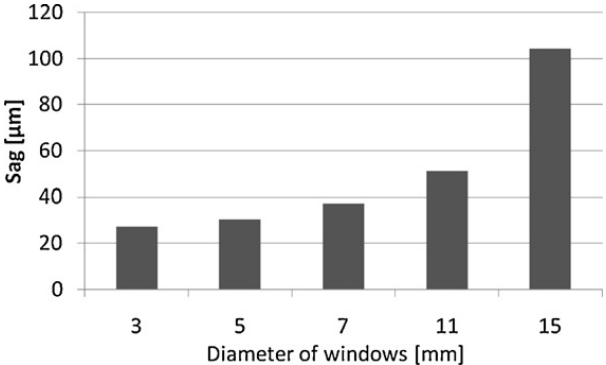


Fig. 8.8. Sagging effect vs. windows diameter [4].

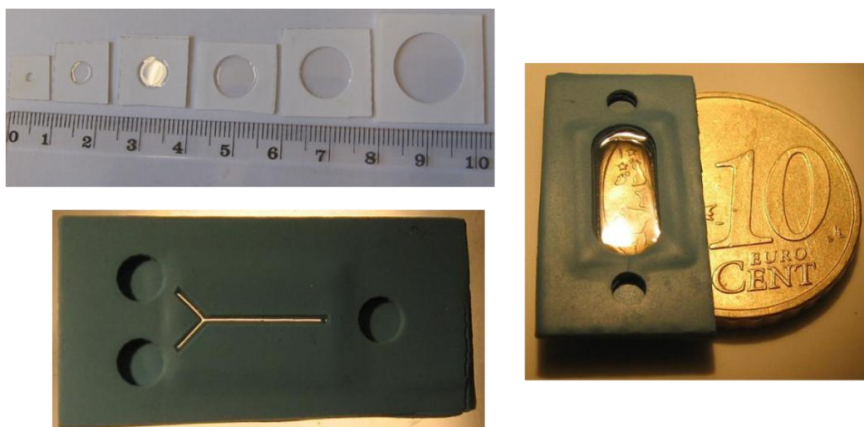


Fig. 8.9. LTCC structures integrated with sodium glass window [4].

8.4. LTCC-PDMS

The microsystems made by the hybrid glass/LTCC technique exhibit some technological limitations. Because of very high ($> 850^{\circ}\text{C}$) encapsulation temperature of the glass-ceramic modules it is impossible to place temperature-sensitive (bio)chemical agents (e.g. catalytic bed, enzyme carrier or polymeric receptor layer) inside the LTCC-based microfluidic device. A solution of this problem can be the technique using plasma assisted bonding of LTCC to transparent polymer (PDMS). A hybrid PDMS/LTCC microsystem takes advantage of the both materials. On one hand, fine fluidic structures can be made in a transparent polymer lid using laser micromachining, hot embossing or soft lithography. On the other hand, a ceramic substrate with integrated conductors, passives, MEMS devices, actuators, optoelectronics components and fluidic structure can be fabricated using the LTCC technology. The general manufacturing process of the hybrid polymeric/ceramic microsystem is presented in Fig. 8.10. In the first step, a PDMS plate is prepared using two-component mixture (prepolymer and cross-linking agent).

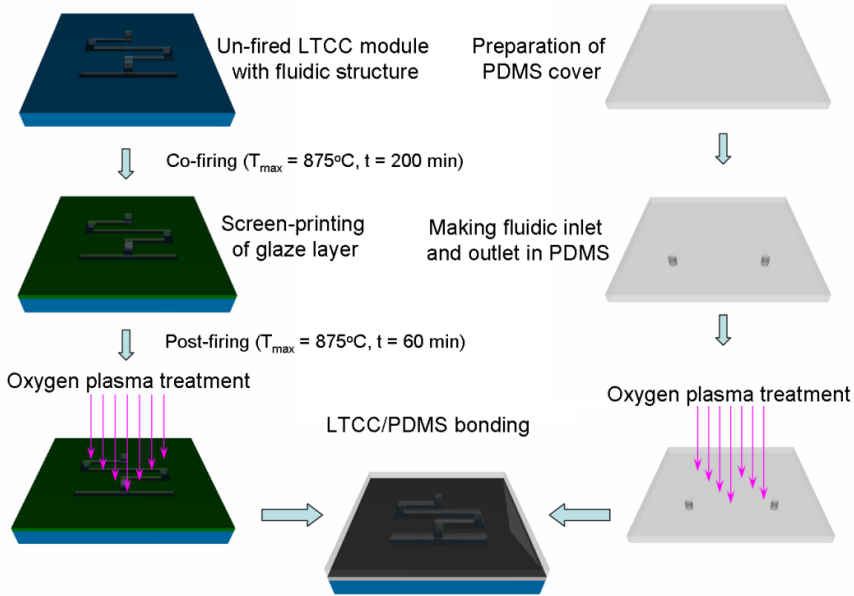


Fig. 8.10. A flow-chart of LTCC-PDMS bonding process [9].

After cross-linking process the fluidic structures can be fabricated in the polymeric substrate. Simultaneously, the LTCC multilayer substrate is manufactured according to a standard technological process. After co-firing the ceramic structure is covered by a thin glaze film using the screen-printing method. Then the glass-covered LTCC module is post-fired in air at temperature the of 875°C for 60 minutes. The glaze layer is applied to eliminate microporosity of the fired LTCC material. In the next step, the surfaces of both materials are activated using microwave oxygen [9] or argon [10] plasma. The plasma generates free radicals and causes formation of silanol groups (Si-OH) on the PDMS surface as it is presented in Fig. 8.11. On the glass surface there are some hydroxyl and other oxygen-containing groups that are created during the glass firing process. During the cooling down the melted glass absorbs water from the surroundings. The energy of

the plasma is big enough to break the hydrogen bonds between the water molecules. The applied microwave plasma divides the O-OH bond into atomic oxygen and additional hydroxyl radicals as shown in Fig. 8.12.

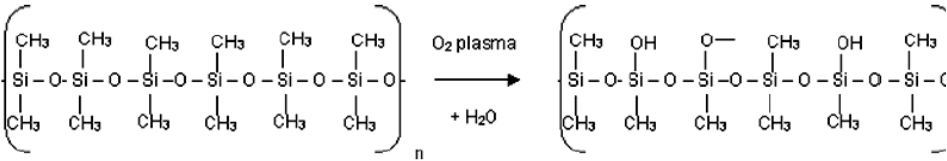


Fig. 8.11. Change in the molecular structures of the PDMS surface after plasma treatment [11].

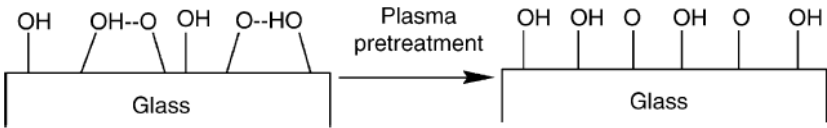


Fig. 8.12. Change in the molecular structures of the glass surface after plasma treatment [12].

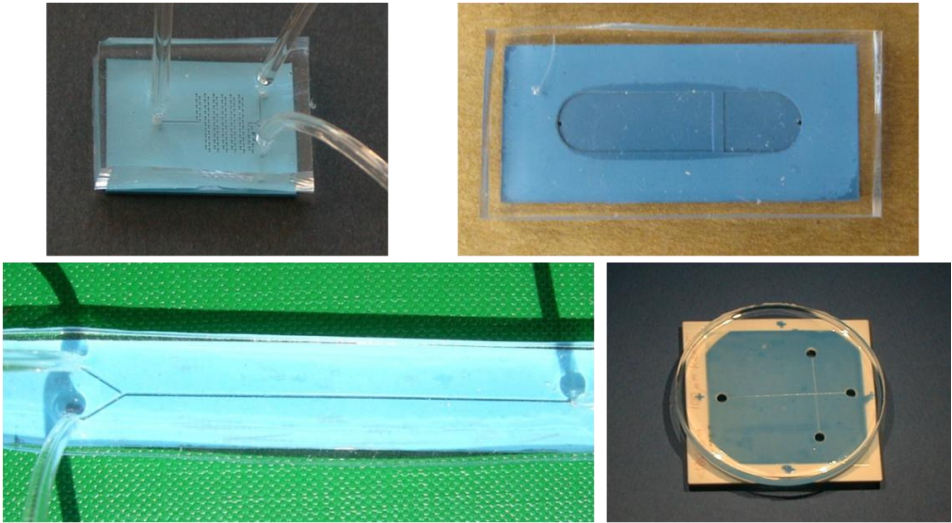


Fig. 8.13. PDMS/LTCC microfluidic structures [5].

After putting the modified sides of the both materials into contact, Si–O–Si covalent bond is formed as a result of condensation reaction between the silanol groups. Exemplary PDMS/LTCC hybrid structures are presented in Fig. 8.13.

8.5. LTCC-ceramic

A ceramic substrate can be bonded to a fired LTCC structure using low temperature glass layer. The flow-chart of the bonding process is presented in Fig. 8.14. In the first step, the ceramic substrate and the LTCC module are covered with a glaze layer. Then the glass-covered surfaces of the materials are put into contact and heated above glass transition temperature. As the temperature decreases the glass layer forms a hermetic bond between the both ceramic substrates. The ceramic structures fabricated using the low temperature glass layer are presented in Fig. 8.15.

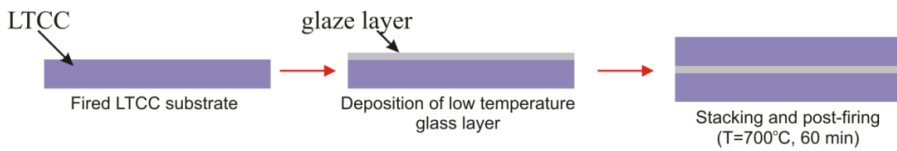


Fig. 8.14. The bonding process of sintered LTCC to ceramic plate.

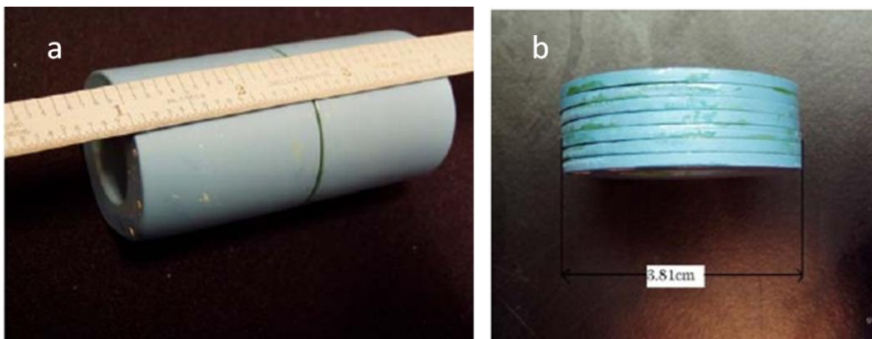


Fig. 8.15. (a) Ion mobility spectrometer drift tube and (b) seven segment stack fabricated using LTCC-LTCC bonding technique [13].

References

- [1] Bergstedt L, Persson K, Printed glass for anodic bonding - a packaging concept for MEMS and system on a chip, *Advancing Microelectronics*, 29 (2002) 1-4.
- [2] Khan MF, Ghavanini FA, Haasl S, Löfgren L, Persson K, Rusu C, Schjölberg-Henriksen K, Enoksson P, Methods for characterization of wafer-level encapsulation applied on silicon to LTCC anodic bonding, *Journal of Micromechanics and Microengineering*, 20 (2010), 064020.1-064010.10.
- [3] Peterson KA, Knudson RT, Garcia EJ, Patel KD, Okandan M, Ho CK, James CD, Rohde SB, Rohrer BR, Smith F, Zawicki LR, Wroblewski BD, LTCC in microelectronics, microsystems and sensors, Proc. 15th IEEE International Conference MIXDES, Poznań (Poland), June 2008, 23-37.
- [4] Bembnowicz P, Golonka LJ, Integration of transparent glass window with LTCC technology for μ TAS application, *Journal of the European Ceramic Society*, 30 (2010) 743-749.
- [5] Chudy M, Malecha K, Golonka LJ, Sosicki A, Roguszczak H, Jakubowska M, Dybko A, Brzózka, Z, Bonding technique of polymer layer with ceramic elements of analytical microsystems, Proc. of SPIE, 6348 (2006) P1-P4.
- [6] Dziuban JA, *Bonding in microsystem technology*, Springer, Netherlands, 2006.
- [7] Müller E, Bartnitzek T, Bechtold F, Pawlowski B, Rothe P, Ehrh R, Heymel A, Weiland E, Schröter T, Schundau S, Kaschlik K, Development and processing of an anodic bondable LTCC tape. Proc. 1st International Conference and Exhibition on Ceramic Interconnect

- and Ceramic Microsystem Technologies, Baltimore (USA), April 2005, 53-58.
- [8] Peterson KA, Rohde SB, Walker CA, Patel KD, Turner TS, Nordquist CD, Microsystem integration with new techniques in LTCC. Proc. IMAPS Conference and Exhibition on Ceramic Interconnect Technology: The Next Generation II, Denver (USA), April 2004, 19-26.
- [9] Malecha K, Gancarz I, Golonka LJ, A PDMS/LTCC bonding technique for microfluidic application. *Journal of Micromechanics and Microengineering*, 19 (2009) 105016.1-105016.8.
- [10] Malecha K, Gancarz I, Tylus W, Argon plasma-assisted PDMS-LTCC bonding technique for microsystem applications. *Journal of Micromechanics and Microengineering*, 20 (2010) 115006.1-115006.8.
- [11] Haines SR, Beamson G, Williams RL, Weightman P, Changes in the electronic structure of silicone rubber surface induced by oxygen plasma treatment, *Surface and Interface Analysis*, 39 (2007) 942-947.
- [12] Wang C, He X, Preparation of hydrophobic coating on glass surface by dielectric barrier discharge using 16 kHz power supply, *Applied Surface Science*, 252 (2006) 8348-8351.
- [13] Weston H, Plumlee DG, Moll AJ, Post-bonding and fabrication of low temperature co-fired ceramic, Proc. 3rd International Conference and Exhibition on Ceramic Interconnect and Ceramic Microsystem Technologies, Denver (USA), April 2007, 320-323.

Chapter 9

LTCC-based microfluidic systems

9.1. Introduction

The modern microfluidic systems consist of several functional blocks (sub-systems). Those sub-systems are responsible for sample transport (micropumps, microvalves), preliminary preparation of the sample (micromixers), carrying out appropriate (bio)chemical reaction (microreactors), product separation and detection of the analyte (electrochemical and/or optical sensors). In this chapter, a briefly description of construction and principle of operation of various ceramic-based microfluidic sub-systems is given.

9.2. Microvalves and micropumps

Microvalves and micropumps cannot be fabricated as monolithic ceramic structures. These devices are made as hybrid structures. The moving part, usually a membrane, is made of silicon or steel. Actuation of the membrane can be made according to the piezoelectric or electromagnetic principle.

Piezoelectric action

Piezoelectricity is an inherent property of a certain group of materials. This feature can be described as a correlation between mechanical and electrical behaviour of these materials. More precisely, applying of mechanical pressure to piezoelectric material produces a small voltage proportional to the applied pressure. Conversely, applying of electric field causes minute dimensional changes in the material [1]. In a microscopic scale, piezoelectricity is a result of non-uniform charge distribution within the unit cell of a crystal. In a consequence of crystal mechanical deformation the positive and negative

charge centres displace by different amounts. Although the overall crystal remains electrically neutral, the variation in the charge centre displacement causes electrical polarization within a crystal structure. This polarization caused by mechanical input is perceived as piezoelectricity [2]. Piezoelectric properties are induced in the ceramics during electrical poling. The poling process is performed at elevated temperature (150°C) in a silicon oil bath. Electrical poling sets mechanical and electrical axes of orientation. When the electric field is applied, the piezoceramics expands along the axis of the field and contracts perpendicular to it (Fig. 9.1).

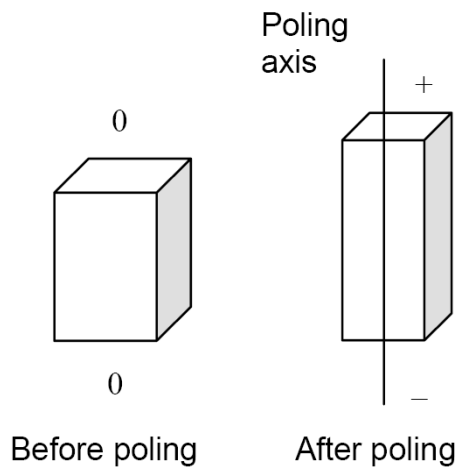


Fig. 9.1. Effect of poling on the dimensions of piezoelectric material [1].

After the poling process the piezoceramics dimensions can be changed, by applying a voltage less than the poling voltage. Dimensional change will be sustained as long as the voltage is applied. Fig. 9.2 illustrates a piezoceramics motor action: conversion of electrical to mechanical energy. An electrically poled ceramics without any applied voltage is presented in Fig. 9.2a. Applying a voltage with polarity matched with the poling voltage results in an additional expansion along the poling axes and contraction perpendicular to it

(Fig. 9.2b). Conversely, applying a voltage with opposite polarity results in contraction along the poling axis and expansion perpendicular to it (Fig. 9.2c). When the voltage is removed the piezoceramics returns to its previous poled dimensions as shown in Fig. 9.2d.

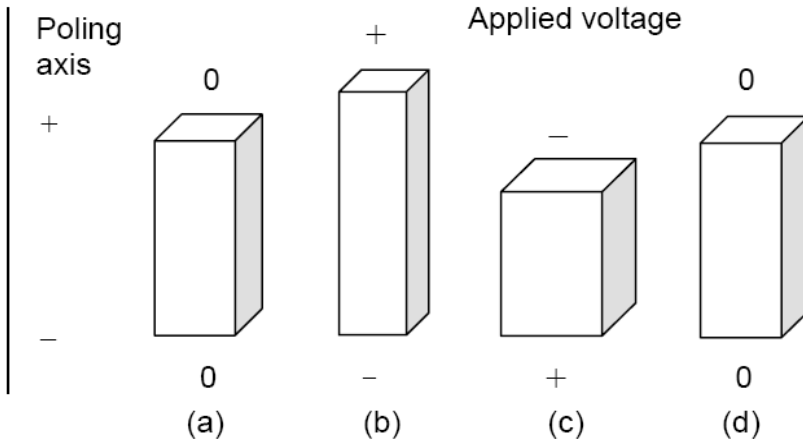


Fig. 9.2. Effect of applying voltage on poled piezoceramics [1].

Generator action (conversion of mechanical to electrical energy) is shown in Fig. 9.3. An electrically poled piezoceramics without applied compressive or tensile stress is presented in Fig. 9.3a. A voltage with a similar polarity as the poling voltage is generated by a compressive force applied parallel to the poling axis, or by a tensile force applied perpendicular to it as shown in Fig. 9.3b. A voltage with reverse polarity is generated by a tensile force applied parallel to the poling axis, or by a compressive force applied perpendicular to it as can be seen in Fig. 9.3c. The piezoceramics returns to its original poled dimensions without generation of voltage as the tensile or compressive stress is removed as presented in Fig. 9.3d.

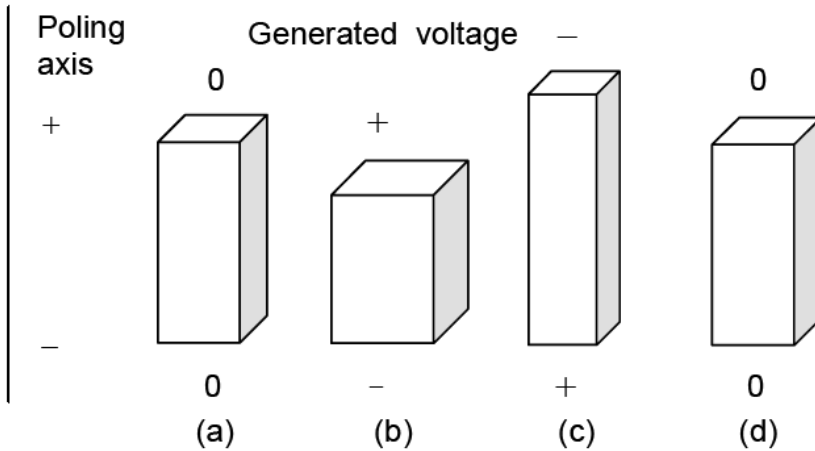


Fig. 9.3. Effect of applying compressive or tensile force on poled piezoceramics [1].

Piezoelectric valve

A piezoelectric initially open valve made using the LTCC technology is presented in Fig. 9.4. It consists of fluidic channels, a cavity, a valve seat and a steel membrane with a deposited piezoelectric layer [3]. The actuation of the valve is based on the piezoelectric unimorph structure which is glued to the fired LTCC module. A unimorph piezoactuator consists of a piezoelectric active layer, and a passive layer i.e. steel membrane. When an electric field is applied transverse expansion and contraction of the piezoelectric active layer with the passive layer occur. These deformations create an internal bending moment and deflection of the structure. Closing of the valve due to bending of the piezoactuator structure under applied voltage is presented in Fig. 9.5.

The unimorph generates approximately $1.3 \mu\text{m}$ displacement, which closes the valve. The dependence between a fluid flow and a pressure applied to the fluid when the valve is opened and closed is presented in Fig. 9.6. The LTCC-based piezoelectric valve exhibits fast actuation due to the relatively high stiffness and high force-delivering capability of the piezoelectric actuator. The valve exhibits off-state leakage of 4% in relation to the flow

rate of the open valve due to surface roughness and LTCC distortion preventing complete sealing of the valve by the membrane.

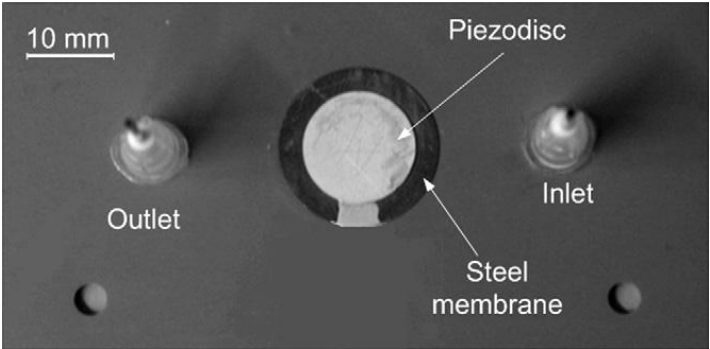


Fig. 9.4. LTCC-based piezoelectric valve [3].

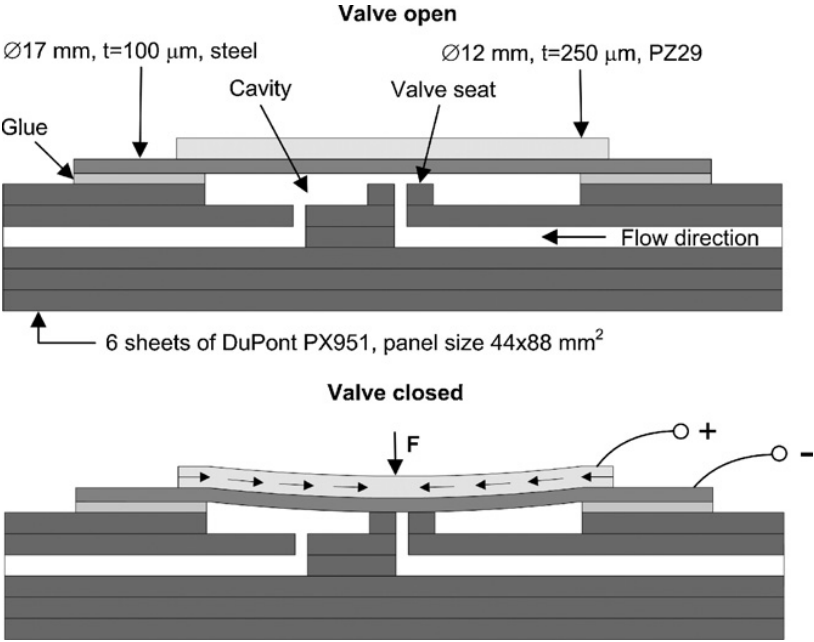


Fig. 9.5. Cross-section of the piezoelectric LTCC valve, not in scale [3].

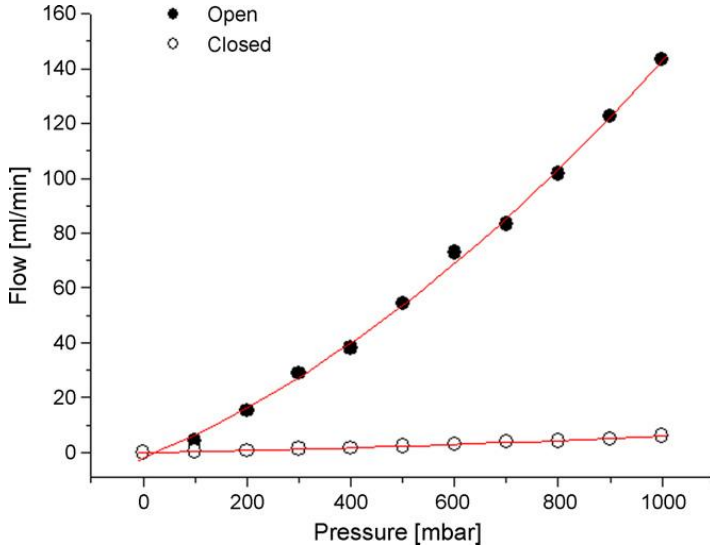


Fig. 9.6. Flow rate as a function of pressure [3].

Piezoelectric pump

The piezoelectric pump consists of fluidic channels, reservoirs, and a pumping chamber with a nozzle-diffuser geometry fabricated in LTCC module. A steel membrane coupled with a piezodisc is glued to the fired structure. The LTCC-based piezoelectric pump is presented in Fig. 9.7.

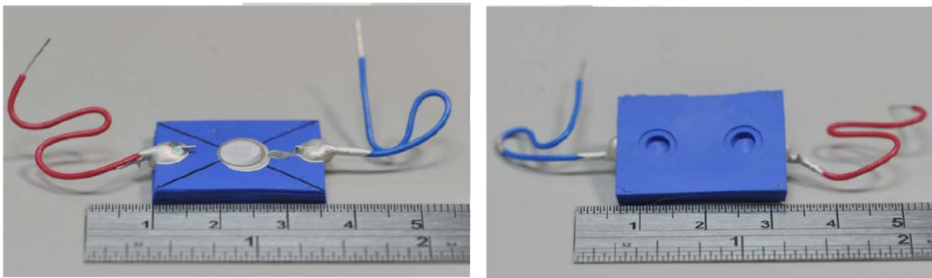


Fig. 9.7. LTCC-based piezoelectric pump [4].

The nozzle-diffuser pumps are built by coupling the nozzle, the pumping chamber and the diffuser together in series. The principle of LTCC-based

piezoelectric pump operation is based on the nozzle-diffuser pumping phenomenon (Fig. 9.8). The volume of fluid in the pumping chamber is periodically varied using an oscillating pressure. Variation of the pressure is provided by a frequent deflection of the steel membrane induced by contraction and expansion of the piezodisc supplied with AC voltage.

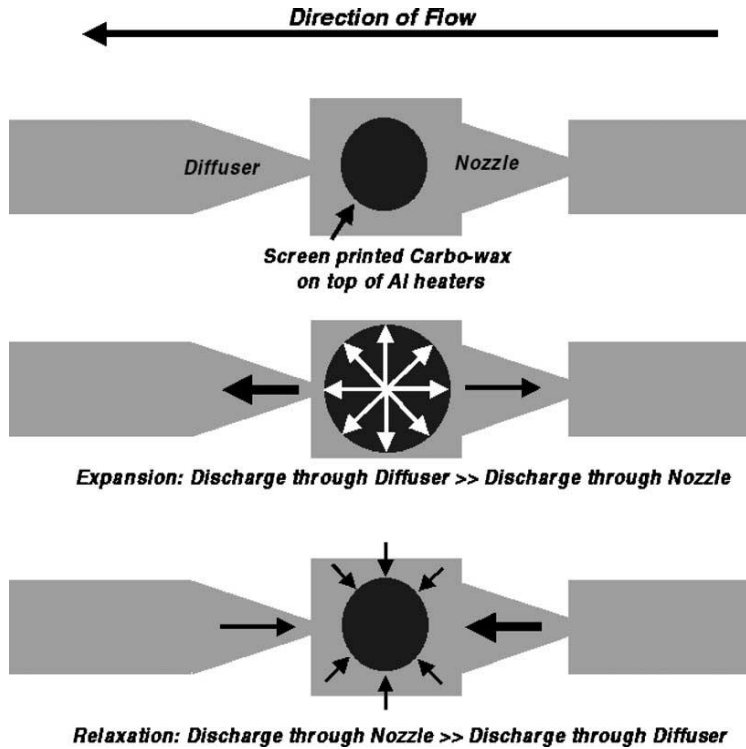


Fig. 9.8. Principle of operation of a nozzle–diffuser pump [5].

The kinetic energy of the fluid (velocity) is converted to the potential energy (pressure) both in the nozzle and diffuser but the efficiency of this process is much greater in the diffuser direction thus discharging more fluid through the diffuser. If Q_d is the discharge through the diffuser and Q_n is the discharge through the nozzle then an increase in the chamber volume causes $Q_d > Q_n$ and a decrease in the chamber volume causes $Q_d < Q_n$ resulting in a net

pumping action [5]. The mean value of fluid flow and displacement of the membrane as a function of applied AC voltage frequency is presented in Fig. 9.9. Nuzzle/ Nozzle-diffuser pumps cannot generate large pressure and are suitable for low-pressure fluidic systems.

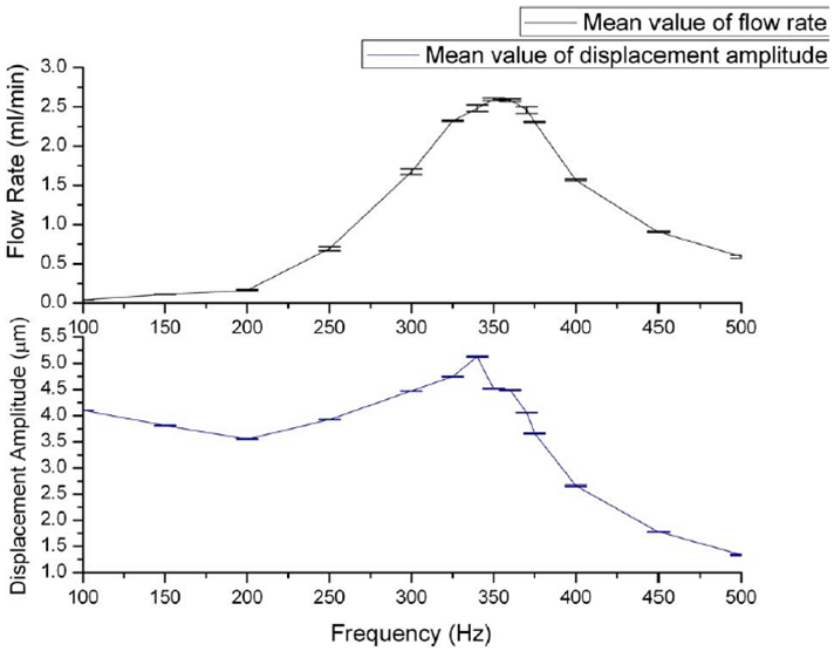


Fig. 9.9. Flow rate and piezoactuator displacement amplitude vs frequency of the AC voltage [4].

Electromagnetic actuation

Forces of magnetic origin are generated by the interaction of a magnetic field with an electrical current [6]. For a vertical actuation, which is commonly used in case of microvalves and micropumps, the force generated by the interaction between magnetic field with intensity H_z created by a current I which flows through a coil and a permanent magnet with magnetization M_z is equal to:

$$dF = M_z \frac{d}{dz} H_z dV \quad (9.1)$$

therefore, the generated force depends on the H_z variation. When the magnet is placed on a flexible spring then the applied force will be equal to:

$$F_z = M_z \int \frac{d}{dz} H_z dV \quad (9.2)$$

As a result of this force, the spring generates a displacement Δz which is proportional to the force divided by the equivalent spring constant k :

$$\Delta z = \frac{F_z}{k} \quad (9.3)$$

Electromagnetic actuation techniques have numerous advantages [6]:

- generation of large force,
- production of relatively large displacement,
- good performance with temperature,
- adequate velocity response,
- robust and inexpensive technique.

Electromagnetic valve

A LTCC-based hybrid microvalve with electromagnetic actuation consists of a multilayer coil, a fluidic channel and a flexible membrane with a permanent magnet bonded to its top surface. The scheme of the magnetic valve is presented in Fig. 9.10.

The fluidic part of the valve is made of three ceramic layers (Fig. 9.11). Layer 1 consists of a fluidic inlet and outlet, a membrane seal and a valve

seat. The fluidic channels are made in layer 2. Layer 3 defines the bottom of the fluidic part.

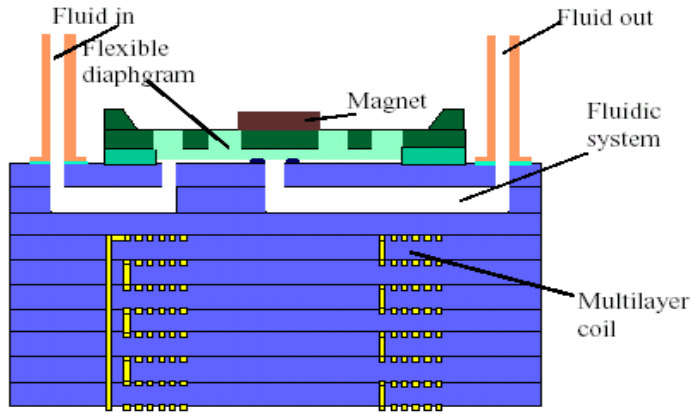


Fig. 9.10. LTCC-based hybrid magnetic valve [6].

The multilayer coil consists of seven layers of a planar spiral implemented on LTCC tapes. The flexible diaphragm attached to the LTCC structure is made of silicon using standard anisotropic etching method. A rare earth magnet (SmCo) is bonded to a flexible diaphragm during its fabrication process. The fabricated hybrid microvalve is presented in Fig. 9.12.

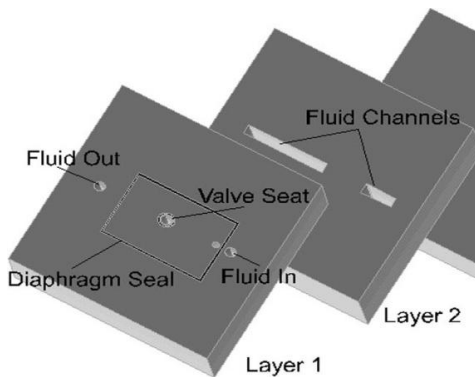


Fig. 9.11. Fluidic part of the magnetic valve [6].

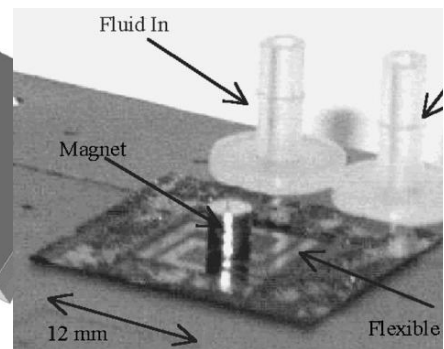


Fig. 9.12. Fabricated hybrid microvalve [6].

Using SmCo magnet with 1 mm diameter it is possible to obtain 200 μm deflection of the 30 μm thick silicon rectangular diaphragm [6]. The dependence between the diaphragm displacement and the current in the coil is presented in Fig. 9.13.

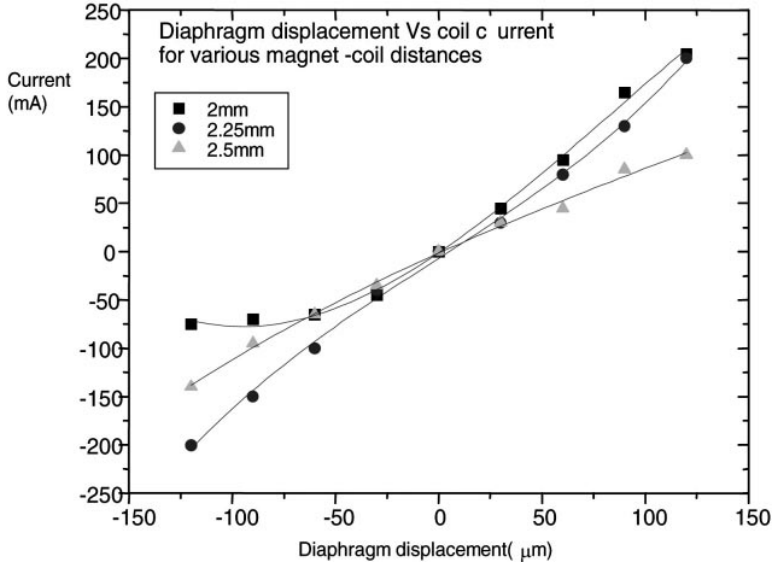


Fig. 9.13. Flexible diaphragm displacement vs. coil current [6].

Electromagnetic pump

A concept of the LTCC-based electromagnetic micropump and its equivalent electronic circuit are presented in Fig. 9.14. The device consists of microfluidic chamber made in the LTCC substrate and a polymeric membrane coupled with a rare earth magnet and an excitation electromagnet [7]. The flexible membrane is made of PDMS (polydimethylsiloxane).

The LTCC-based electromagnetic pump utilizes two ball valves which act as fluidic diodes and prevent back flow. The applied balls are made of

sapphire glass. The principle of LTCC-based electromagnetic pump operation is depicted in Fig. 9.15.

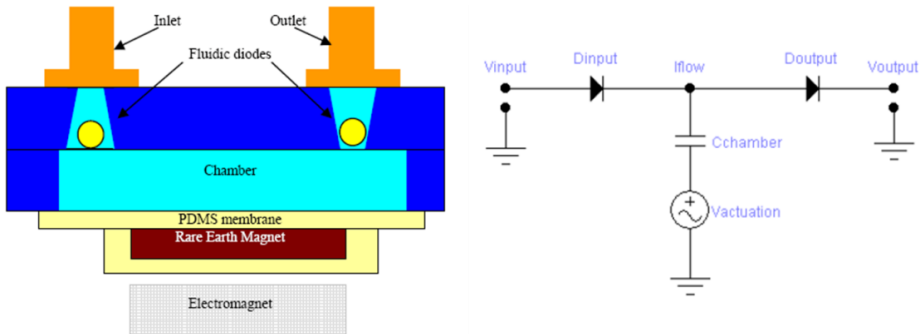


Fig. 9.14. LTCC-based electromagnetic micropump design and its electronic equivalent circuit [7].

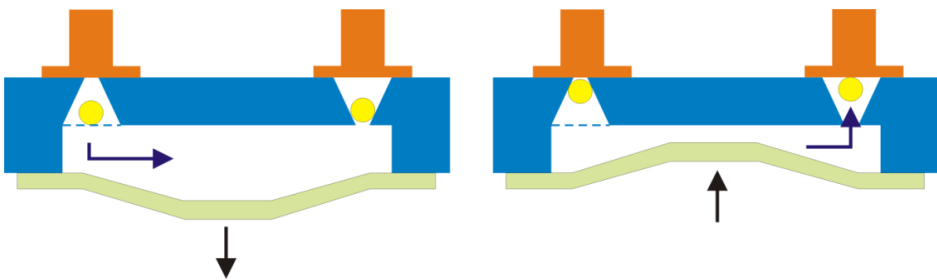


Fig. 9.15. Principle of operation of LTCC-based electromagnetic pump.

The volume of the fluid in the chamber is periodically varied due to deflection of the PDMS membrane. The deflection is caused by frequently changes of the electromagnet polarity. When the membrane goes down (chamber expansion) the inlet fluidic diode is opened and the fluid is drawn into the chamber. When the polarity of the electromagnet is changed the magnetic forces causes a deflection of the membrane. As a result of the chamber contraction the inlet diode is closing. Simultaneously the outlet diode is opening and the fluid can be pumped out of the chamber.

9.3. Ceramic micromixers

One of the essential parts of a modern microfluidic system is an efficient micromixer. For example, enzymatic reactions require the intermix of all reagents for initiations. In general, micromixers can be classified as either active or passive [8]. An active micromixer requires external energy (pressure, temperature, electro-hydro-dynamics, acoustics, etc.) to generate disturbances necessary to achieve efficient mixing process. Contrary to the active micromixers, the passive mixing structures do not require any external forces. Their mixing efficiency relies entirely on molecular diffusion and chaotic advection. The passive micromixers are generally easier to fabricate and integrate with other microfluidic devices. A good mixing structure should homogenise two (or more) fluids in micro- or nanoliter volume scale without taking much space in acceptable time-scales. However, due to very small dimensions of the microfluidic systems the flow is mostly in laminar regime. As a consequence, the mass transfer is based mainly on molecular diffusion. The diffusive mixing process is relatively slow in comparison with the rate at which fluid is convected along the conduit. This make an effective mixing of initially segregated fluids difficult. The Péclet number represents the ratio between the mass transport due to convection and that of diffusion, and is defined as:

$$Pe = \frac{UD_h}{D} \quad (9.4)$$

where U is a mean fluid velocity (m/s), D_h is a hydraulic diameter (m) and D is a coefficient of molecular diffusion (m^2/s). It varies from approximately 10^9 for small molecules (e.g. water) to 10^{11} for the larger ones (e.g. glucose). Convection is dominant at higher Péclet number. Typical values of the Pe for

microfluidic systems are high and vary from 10^1 to 10^6 [2, 7]. The Péclet number can be interpreted as a ratio of diffusive mixing time:

$$\tau_{diff} \sim \frac{D_h^2}{D} \quad (9.5)$$

Using equations (6.6) and (9.5) we can infer that fluids which move with a mean velocity U have to pass through a distance $U(D_h^2/D)$ to be completely mixed. For example, the mixing time and distance required to homogenise the concentrations at a mean flow velocity of 1 mm/s and a channel hydraulic diameter of 200 μm may vary from 40 s and 0.4 m for a diffusion coefficient of 10^{-9} m^2/s to 4000 s and 40 m for diffusivity of 10^{-11} m^2/s .

The magnitude of the mass flux (J) of the fluid particles due to the molecular diffusion is equal to:

$$J = -D\nabla c \quad (9.6)$$

where c is the concentration [m^{-3}]. From this equation, it is clearly seen that the key to efficient mixing in microscale relies mainly on two issues:

1. interface area between two initially segregated fluids,
2. the ability to create high concentration gradients between two mixing fluids.

On one hand, a larger interface area results in a larger area for mass transfer. On the other hand, very high concentration gradients accelerate the diffusion process. Elongation of the intermaterial area and the increase in concentration gradients can be achieved by stretching and folding phenomena characteristic for chaotic advection. These effects can be obtained in microfluidics through the appropriate design of the micromixer's channel geometry. Spatial changes along the fluidic channel axes result in frequent changes of flow direction.

The mixing process in a microfluidic system can be modeled and visualized by solving the convection-diffusion equation:

$$\frac{\partial c}{\partial t} + u\nabla c = D\nabla^2 c \quad (9.7)$$

where $u = (u, v, w)$ is the fluid velocity vector in (m/s). The velocity field can be calculated from the Navier-Stokes equation (6.15).

Magneto-hydro-dynamic(MHD) mixer

The device takes advantage of Lorentz force induced by the coupling between the magnetic field B and the electrical field E . This force is applied to disturb the fluid flow pattern within a device. The MHD mixer is made of three LTCC tapes and a permanent Neodymium magnet. The details of the particular ceramic layers and cross-section of the device are presented in Fig. 9.16.

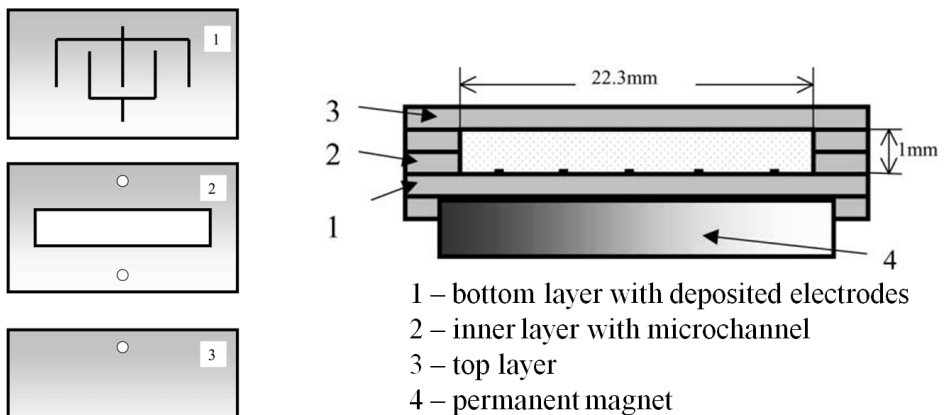


Fig. 9.16. LTCC layers and cross-sectional view of the MHD micromixer [9].

Gold electrodes are deposited on layer 1. Layer 2 contains the mixing channel and two vertical vias for electrical connections. The structure is sealed by layer 3. The mixing channel is filled with an electrolyte solution. By applying alternating potential across the pairs of the electrodes, currents are induced in various directions in the solution. In the presence of a magnetic force (induced by permanent magnet) the currents generate the Lorentz force in a perpendicular direction to both magnetic and electrical fields. The direction of the force alternates according to the changes of the positive and negative poles of a DC power supply. The Lorentz force is applied to induce mixing movement of the fluid in the channel. It causes stretching and folding of the fluid in the mixing channel. As a result, the interface layer (*IL*) between two mixing fluids is being deformed. The structure of the interface layer at various times is shown in Fig. 9.17. As time goes by, the *IL* elongates and deforms. A larger contact area means a larger area for mass transfer between two mixed fluids.

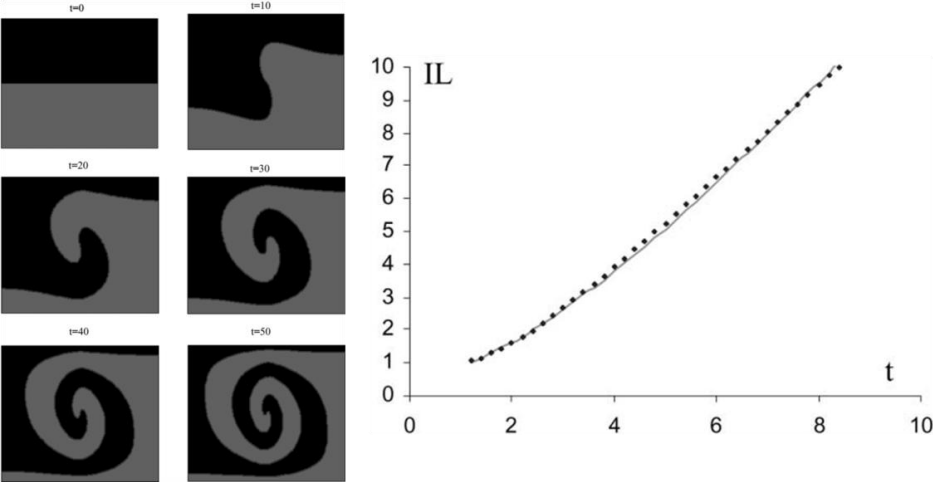


Fig. 9.17. The structure and length of the interface layer (*IL*) as a function of normalized time [9].

Serpentine passive mixers

In case of passive micromixers the improvement of the mixing process can be obtained by increasing the contributions of the convection part in equation (9.7). That can be achieved through the proper design of the mixing structure. Yi and Bau [10] have shown that the appropriate number of bends can enhance the mass transfer in micro-scale. Therefore, most of the passive mixers are arranged in a serpentine configuration (Fig. 9.18).

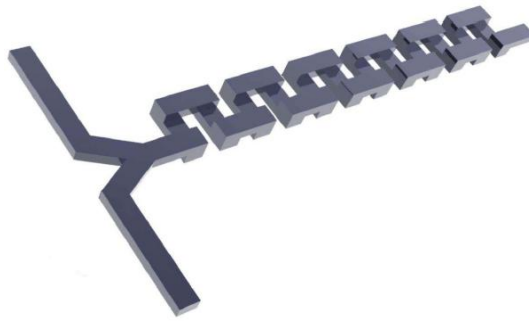


Fig. 9.18. Serpentine micromixer [11].

The efficiency of the serpentine micromixer relies on inertial effects. For relatively low Reynolds numbers (less than ca. 10) the mixing is poor, but for the Reynolds numbers greater than ca. 10 the mixing efficiency increases. The results of mixing modelling for the Reynolds numbers equal to 1 and 10 are presented in Fig. 9.19. For low Re numbers (≤ 5) viscous effects dominate and the bend-induced fluid recirculation and disturbances decay rapidly. When Re number increases the mixing process is much better. The fluids remain separated only in the vicinity of the T-junction, but appear to be well homogenised after passing through about 8 bends. No separation between the fluids can be noticed. For a relatively high values of the Reynolds number (flow rate), the interface layer enlarges due to the stretch and fold phenomena. As the interface layer (IL) length increases, the two

materials are brought into closer contact creating more space for the fluid particles for diffusion. Fig. 9.20

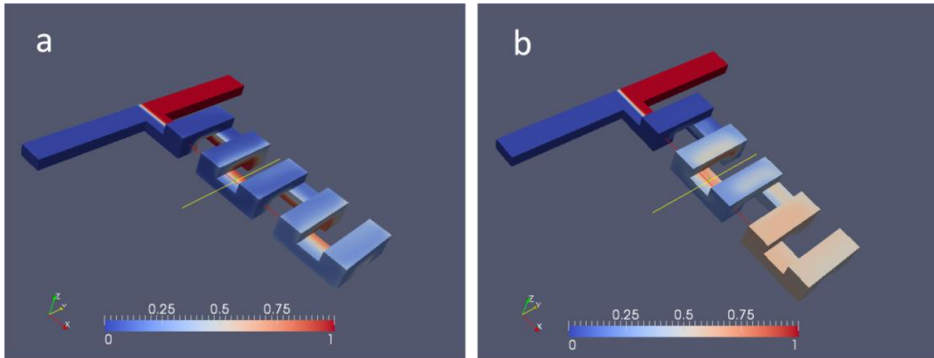


Fig. 9.19. Concentration distribution in a serpentine micromixer for (a) $Re = 1$ and (b) $Re = 10$ (Results of numerical computations).

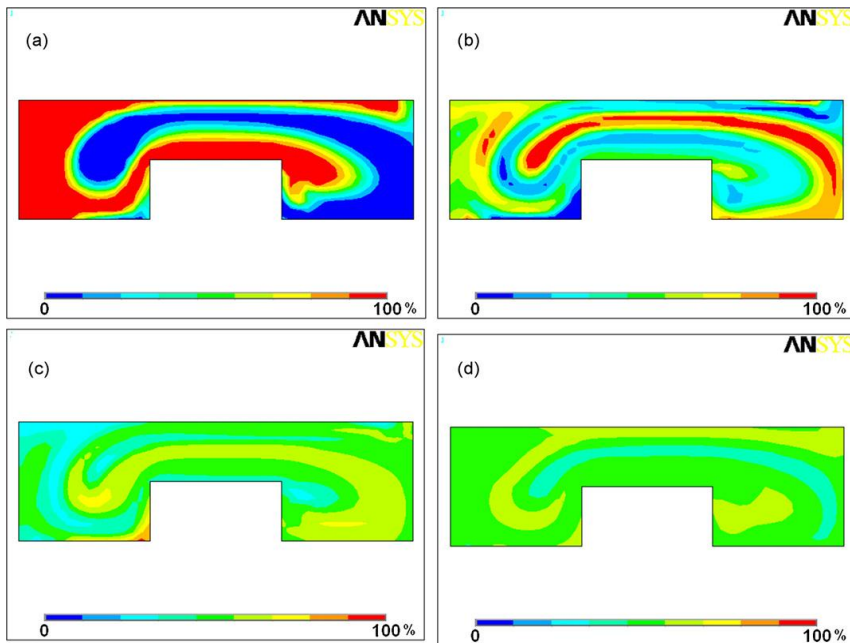


Fig. 9.20. Concentration distribution of the interface layer for a serpentine micromixer as the flow passes through n bends: (a) $n = 1$, (b) $n = 3$, (c) $n = 5$, (d) $n = 7$ (Results of computations) [11].

presents the structure of the interface layer between two fluids after the flow has passed through 1, 3, 5 and 7 bends for $Re = 10$. The length of the interface layer between two miscible fluids rises nearly linearly with the number of the bends and with Re number as can be seen in Fig. 9.21. Exemplary LTCC-based serpentine microfluidic mixer is presented in Fig. 9.22. It is made of three ceramic layers. The first layer defines the bottom of the structure. The next two layers creates serpentine geometry. The LTCC structure is sealed by a transparent PDMS plate with attached fluidic ports.

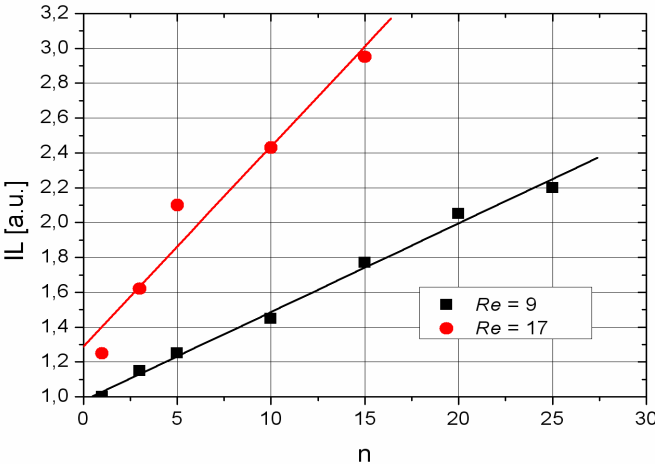


Fig. 9.21. Length of the interface layer as a function of the number of bends [11].

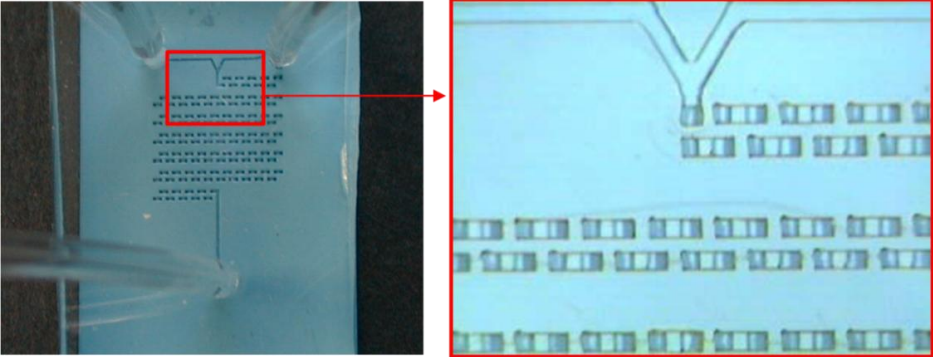


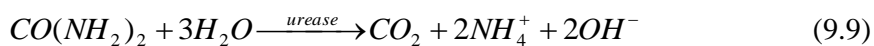
Fig. 9.22. LTCC-based serpentine micromixer with a PDMS cover.

9.4. Microreactors

Microreactor technology has become a new and very promising subject in the field of chemistry, microbiology, process engineering and biotechnology within a very short time. A microreactor is a miniature system, where a reaction proceeds and it uses a very small amounts of reagents. Microreactors can work as a stand-alone devices as well as a part of various lab-on-chip or micro-total analytical systems. The stand-alone microreactors can be used for example in the (i) pharmaceutical industry for evaluation of the influence of different chemical compounds and drugs on enzyme activity, (ii) molecular biology for DNA amplification and sequencing and (iii) high throughput chemical synthesis.

Enzymatic microreactor for urea determination

A batch type flow-through enzymatic microreactor with an integrated platinum heater and temperature sensor made with use of the LTCC technology is shown in Fig. 9.23. The presented construction of the microreactor is based upon similar one made in silicon. The ceramic-based microdevice consists of two cavities separated by a threshold. The batch in the form of porous glass beads with immobilized enzyme (urease) is placed in a larger compartment of the microreactor. The principle of the microfluidic system operation is based on hydrolysis of urea catalyzed by urease:



One of the reaction (9.9) products is a hydroxyl group which can be used for indirect determination of urea (pH measurements) in the investigated sample.

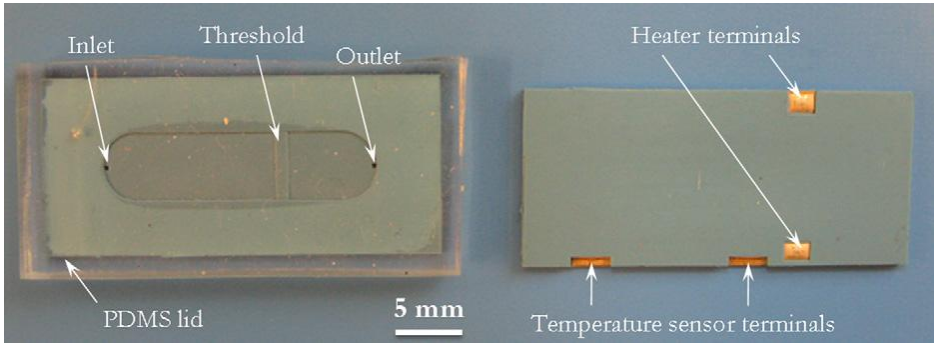


Fig. 9.23. LTCC-based enzymatic microreactor [12].

Geometry of the microreactor is optimized according to the results of the CFD modeling. The goal of the simulation was to estimate conditions that impedes fluid recirculations inside both microreactor's cavities. Simulations were made for a microreactor with rectangular and rounded chambers. The results of the CFD analysis for the rectangular cavity are presented in Fig. 9.24.

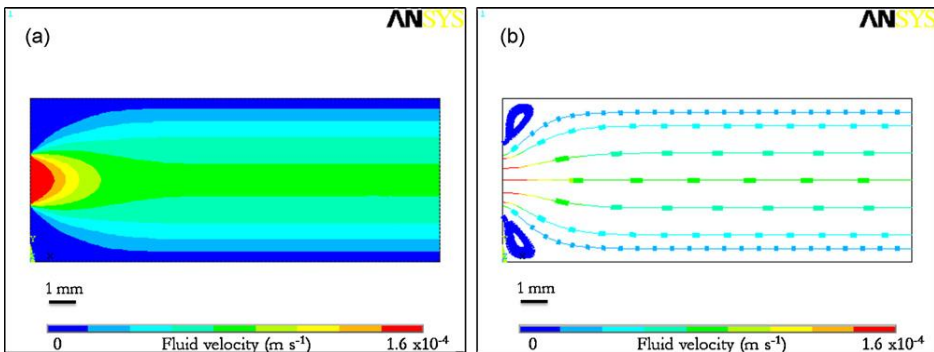


Fig. 9.24. Results of CFD simulations (in m/s) for a rectangular reaction chamber: (a) velocity field and (b) fluid trajectories [12].

As can be seen in Fig. 9.24 in the corners of the rectangular chamber the areas of fluid recirculations are formed. As a result, an effective pumping out of the entire volume from the reaction chamber is hindered. Moreover, the fluid recirculation in the corners makes the removal of all used beads with enzyme (e.g. for enzyme regeneration) impossible. The results of computations obtained for a rounded chamber are presented in Fig. 9.25.

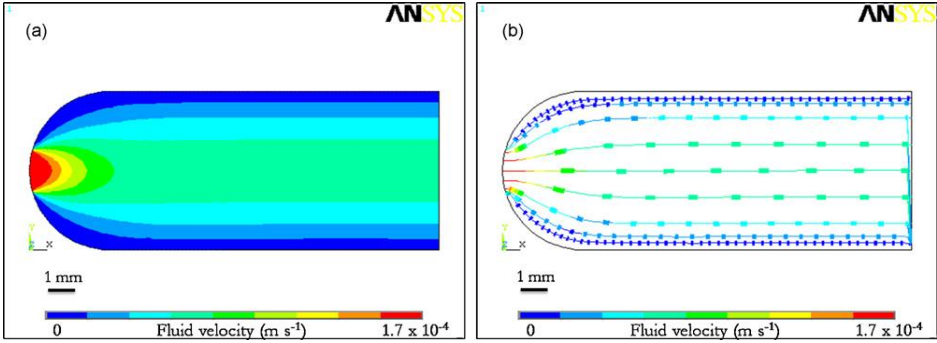


Fig. 9.25. Results of CFD simulations (in m/s) for a rounded reaction chamber: (a) velocity field and (b) fluid trajectories [12].

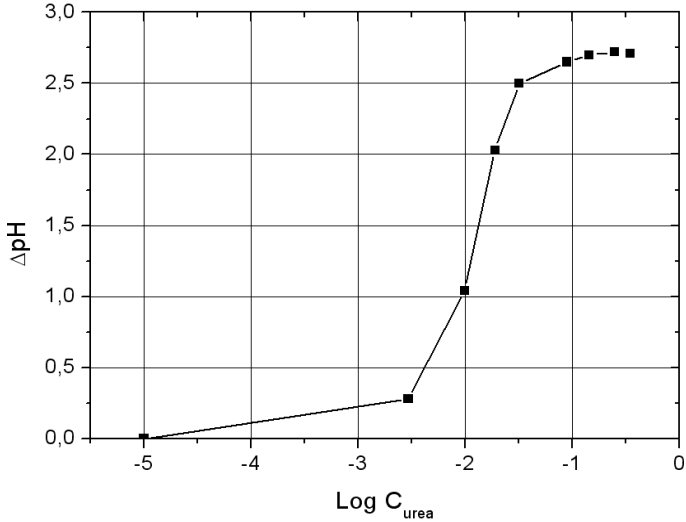


Fig. 9.26. Calibration curve for an enzymatic microreactor with urease immobilized onto glass beads.

For this version of the microfluidic reactor the areas of fluid recirculation seem to be eliminated. Calibration curve for an enzymatic microreactor is shown in Fig. 9.26. The output signal of the microreactor loaded with enzyme immobilized onto porous glass beads is very high – ca. 2.5 pH units – and comparable with the output signal reported for silicon-based microreactor [16]. The main features of the presented batch type enzymatic microreactor are the following: variety of materials for an enzyme support, simplicity of upload, easy control of enzyme activity and very good long-term stability.

PCR (Polymerase Chain Reaction) microreactors

The polymerase chain reaction (PCR) is a unique temperature controlled process, by which the selected DNA fragments can be copied many times. It is one of the most important techniques which finds practical application in genetic identification and gene diagnostics. The PCR reaction is performed during several temperature cycles. Each cycle consists of three specific temperatures: separating a double-strand DNA (denaturation, $T = 94^{\circ}\text{C}$), attaching of the specific primers to the template (annealing, $T = 50 - 60^{\circ}\text{C}$) and extending the primers with chemical enzyme (extension, $T = 72^{\circ}\text{C}$). Theoretically, after each cycle, the number of DNA segments duplicates what gives 2^n copies of specific DNA molecules in n steps [13].

The miniaturization of the thermocyclers for a rapid DNA amplification has been playing a major role to meet the current demands in the field of molecular biology. The PCR microreactors, in comparison with classical laboratory equipment, are characterized by quicker thermal cycling, smaller reactants volumes and less power consumption. Moreover, there is a possibility to integrate such miniature thermocycler with an optical detection system in order to develop a real-time PCR device. There are two main

approaches to construct the PCR microreactors: flow-through and microchamber. The flow-through thermocycler consists of a fluidic channel which is split into three temperature zones. The temperature of each zone corresponds to the specific temperature of the PCR cycle. The amplification of the DNA is performed by pumping the sample through the three temperature zones of the fluidic channels. An exemplary construction of the flow-through PCR microreactor is presented in Fig. 9.27.

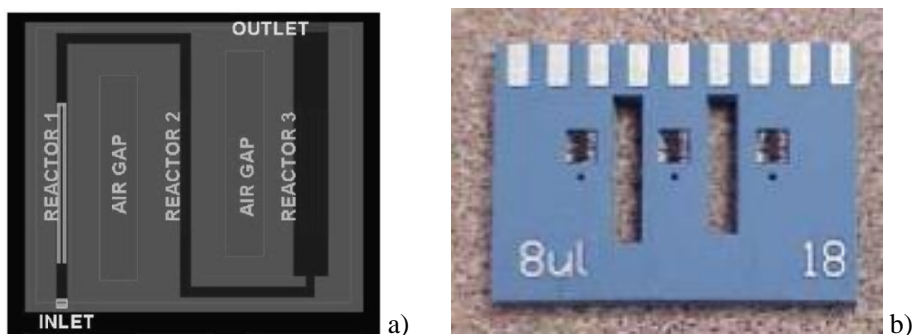


Fig. 9.27. (a) Scheme and (b) photograph of the flow-through PCR microreactor [14].

It consists of a serpentine channel with different cross-sectional areas in different temperature zones to ensure adequate residence time of the sample for denaturation, annealing and extension reaction. Air-gaps made in the PCR microreactor ensure thermal isolation between the individual reaction zones. Thick-film heaters are fabricated below each reaction zone. They are made of AgPd paste using screen-printing method. Simulated temperature profiles across the central plane of the LTCC-based flow-through PCR microreactor and experimentally validated infrared image of its surface temperature are presented in Fig. 9.28.

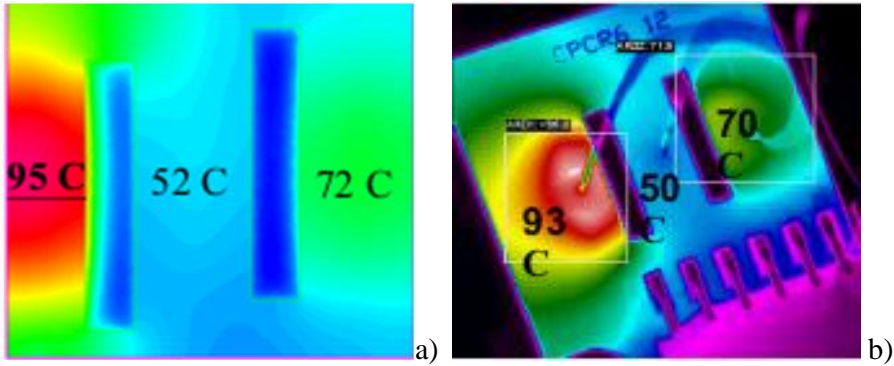


Fig. 9.28. (a) Simulated temperature profiles across the central plane and (b) experimentally validated infrared image of the surface temperature profiles of the three temperature zones [15].

The microchamber PCR reactor is a device where the DNA sample and other reagents are held whilst the temperature is changing [16]. The device consists of a reaction chamber, a thick-film heater, a SMD temperature sensor (Pt 100) and an optical waveguide integrated in one LTCC structure. Integration of the optical waveguide enables light excitation of the DNA sample for fluorescence measurements and optical monitoring of the process. The microchamber PCR reactor is sealed with a sodium glass plate using the LTCC-glass bonding technique. The LTCC-based microreactor is depicted in Fig. 9.29.

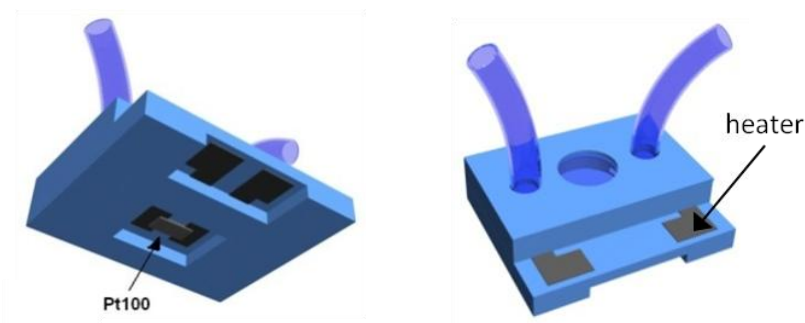


Fig. 9.29. Microchamber PCR reactor [16].

The presented microchamber reactor is suitable for the fluorescence measurement of the PCR reaction product. The sample is excited by an external laser light with the wavelength of 532 nm through an integrated glass optical waveguide. The fluorescent light is collected by the external CCD camera. According to the measurements the LTCC-based microchamber PCR reactor is characterized by sensitivity better than 0.02 ng/ μl . The device during the fluorescence measurements and its corresponding calibration curve are presented in Fig. 9.30.

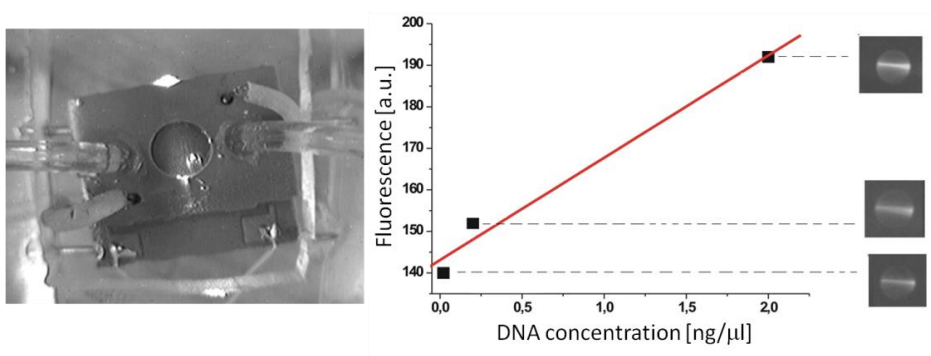


Fig. 9.30. The LTCC-based PCR microreactor during fluorescence measurements (left) and its calibration curve (right) [16].

9.5. Electrochemical sensors

Potentiometric sensor with ion selective electrode (ISE) based array

The LTCC-based potentiometric sensor with an integrated ISE array consists of a fluidic channel with rounded corners and four ISE electrodes. The rounded shape of the fluidic channel is designed according to the CFD analysis. The rounded corners of the fluidic channel let us avoid fluid recirculation and dead-zone formation inside the sensor. The LTCC-based potentiometric sensor is dedicated to potassium ions determination in water. The principle of the sensor operation is based on the measurement of

potential of a specific ion in the solution by ISE electrode. This potential is measured against a stable reference electrode (RE) of constant potential. The potential difference between the two electrodes depends upon the concentration of specific ions in solution. The ISE electrodes work on the basic principle of the galvanic cell (Fig. 9.31).

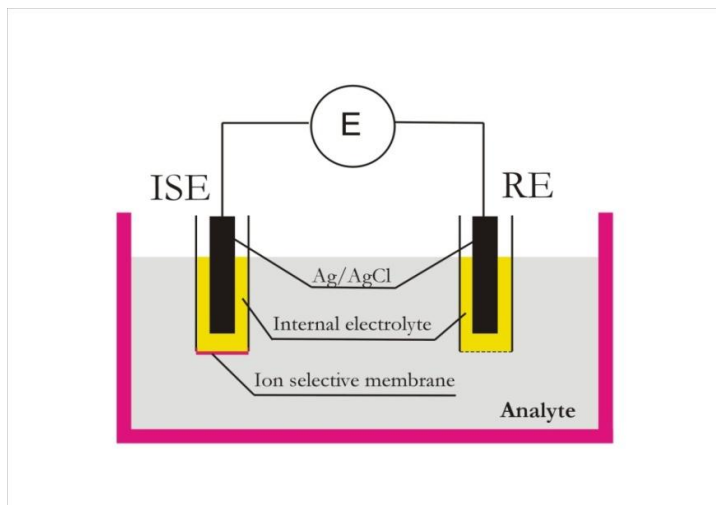


Fig. 9.31. ISE-based galvanic cell.

By measuring the electric potential generated across a membrane by specific ions, and comparing it to a reference electrode, a net charge is determined. The strength of this charge is directly proportional to the concentration of the selected ions. The potential of the ISE electrode (E_{ISE}) depends on the logarithm of the specific ion concentration, according to the Nikolsky equation:

$$E_{ISE} = E^0 + \frac{RT}{nF} \ln \left(c_i + \sum_{j=1}^n K_{ij} c_j^{n/z} \right) \quad (9.10)$$

where E^0 is the standard electrode potential (V), R is the universal gas constant ($8.314 \text{ J} \cdot \text{K}^{-1} \text{ mol}^{-1}$), T is the absolute temperature (K), F is the Faraday constant ($9.648 \cdot 10^4 \text{ C} \cdot \text{mol}^{-1}$), K_{ij} is the selectivity coefficient for ion j of an electrode sensitive to ion i , z is the valence of the primary ion j , n is the valence of the interfering ion j .

The LTCC-based potentiometric sensor is built of a rounded fluidic channel and four chambers for ISE electrodes. Each of the chambers consists of three cavities for an ion-selective membrane, Ag/AgCl electrode and hydrogel layer. Dimensions of the cavities are equal to 2 mm^2 , 1.5 mm^2 and 1 mm^2 , respectively. A schematic view of the LTCC-based potentiometric sensor with integrated ISE array is illustrated in Fig. 9.32.

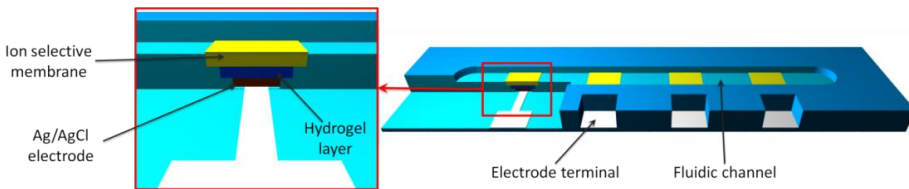


Fig. 9.32. Schematic view of the LTCC-based potentiometric sensor.

The real structure of the sensor was manufactured from nine LTCC tapes. The fluidic channels and cavities were cut out in ceramic layers using Nd-YAG laser before firing. The ISE-array located inside of the LTCC module was deposited with use of silver ink by screen printing method. After laser cutting and screen printing, all ceramic tapes were laminated and co-fired. The real structure of the LTCC-based potentiometric sensor is presented in Fig. 9.33.

The silver/silver chloride electrodes were made by electrochemical chloriding of screen printed silver pads in 0.1 M potassium chloride (+1.5 V vs. Pt electrode, until total decline of the current for at least 15 minutes). After the chloriding, the electrodes were chemically modified to form an intermediate

hygel layer and ion selective membrane. The dynamic response of the sensor for various concentrations of potassium ions and corresponding calibration curve are presented in Fig. 9.34.

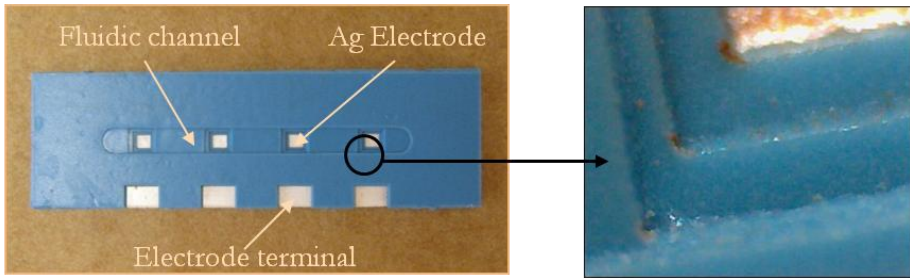


Fig. 9.33. LTCC potentiometric sensor (after chloridization and deposition of hydrogel and ion selective membrane layers) [17].

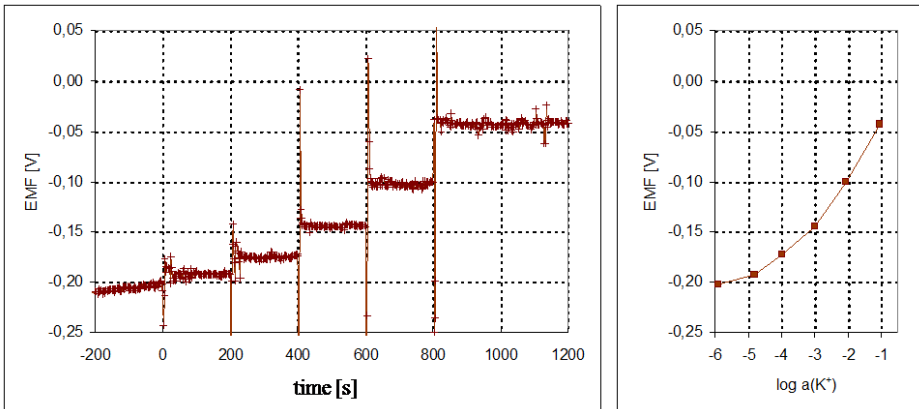


Fig.. 9.34. Time responses and the corresponding calibration curve of the LTCC potentiometric sensor (potassium ions) [17].

PDMS/ceramic module for potentiometric determination of urea

The microfluidic module is fabricated using a hybrid technology which combines ceramic and polymeric materials. The device is designed for determination of urea in biological fluids. Detection of the analyte is based on the hydrolysis reaction of urea catalyzed by urease (9). By measuring

concentration of NH_4^+ ion, which is one of reaction (9) product, it is possible to determine urea concentration in the test solution. The concentration of NH_4^+ ions is determined using potentiometric method. As can be seen in Fig. 9.35, the flow-through detection module is made of three layers: (a) the ceramic substrate with deposited silver electrodes, (b) the PDMS thin layer with the holes for ion-selective membranes and (c) the PDMS cover plate with a microchannel and inlet/outlet holes. The module is based on ceramic (96% Al_2O_3) substrate with screen-printed silver electrodes. The NH_4^+ selective membranes are deposited on the surface of the electrodes.

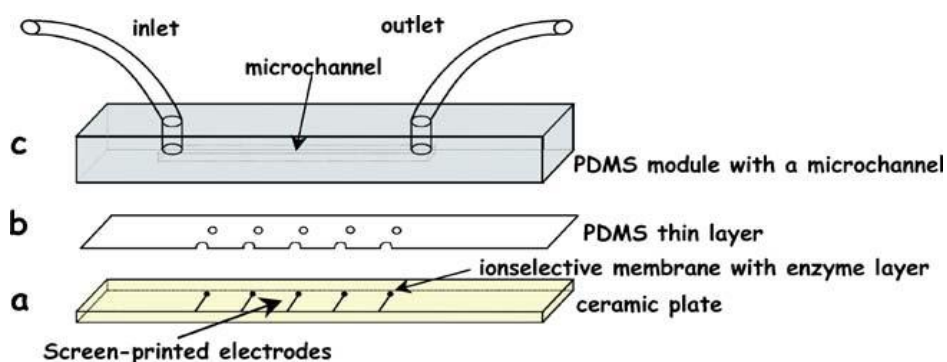


Fig. 9.35. Scheme of the module for potentiometric determination of urea [18].

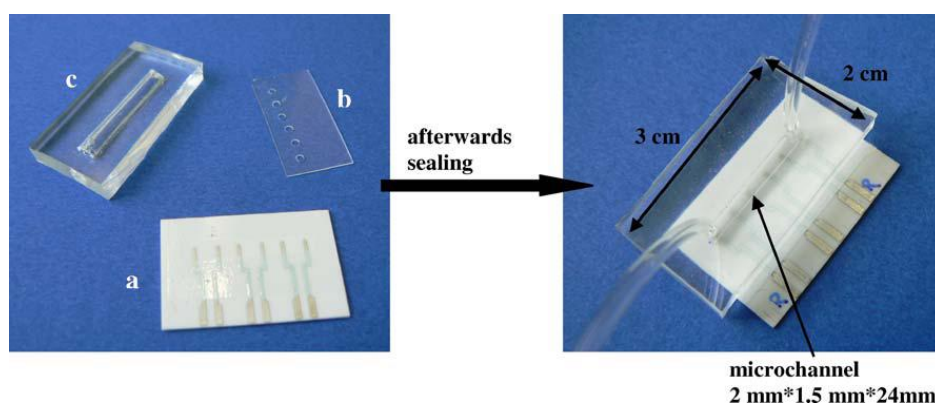


Fig. 9.36. Module made of ceramic and PDMS before (left) and after plasma bonding (right) [18].

Enzyme-urease is covalently immobilized onto the membrane surface. The ceramic substrate is bonded with the PDMS material using microwave plasma. The flow-through detection module before and after the bonding process is presented in Fig. 9.36. The dynamic response and corresponding calibration curve of the module is presented in Fig. 9.37.

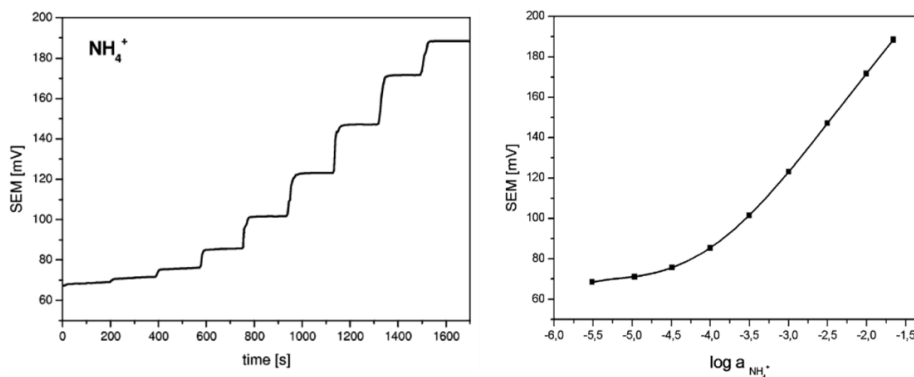


Fig.. 9.37. Time responses and the corresponding calibration curve of the module [18].

Amperometric sensor for continuous glucose monitoring

A flow-through sensor with an integrated microdialysis tube and three thick-film electrodes for amperometric detection fabricated using the LTCC technology is illustrated in Fig. 9.38. This microsystem is destined for continuous monitoring of various (bio)chemical compounds (e.g. glucose, lactate, glutamate). The principle of its operations is based on the size selective diffusion of the glucose. The glucose diffuses from the test sample through the walls of the semi-permeable dialysis tube to the microreaction cell. The microreactor is filled with the buffer solution containing free enzyme – glucose oxidase (GOx).

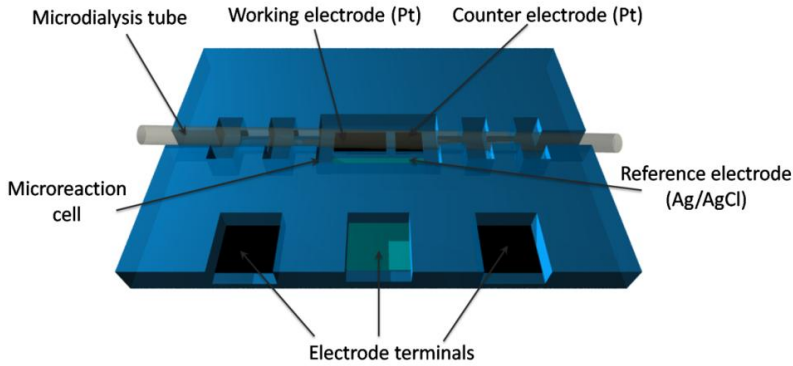
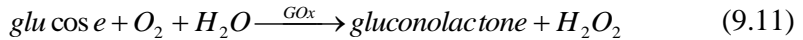
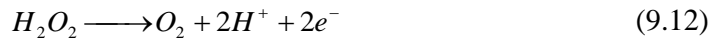


Fig. 9.38. Construction of the amperometric glucose sensor [19].

In the presence of the GOx the glucose is electro-oxidized on the surface of the working electrode and gluconolactone and hydrogen peroxide is produced:



One of the reaction products is a hydrogen peroxide which is detected amperometrically during its oxidation at the surface of the working electrode:



The current resulting from reaction (12) is a measurand as it is proportional to the glucose concentration in the sample. The amperometric glucose sensor is made of ten LTCC layers. The openings for the microreaction cell, the channel for the microdialysis tube and the electrode terminals are made with a Nd:YAG laser. Platinum paste is used for construction of the working and counter electrodes while silver paste is used for the reference electrode. The LTCC-based amperometric sensor's reaction cell with a fixed microdialysis

tube is presented in Fig. 9.39. The dynamic response and corresponding calibration curve of the sensor are presented in Fig. 9.40. A linear response of the LTCC-based amperometric sensor to glucose was up to 13 mM. The presented ceramic sensor has about ten times higher sensitivity (ca. 135 nA/mM) in comparison with a similar construction of sensor made in silicon (ca. 16 nA/mM) [19].

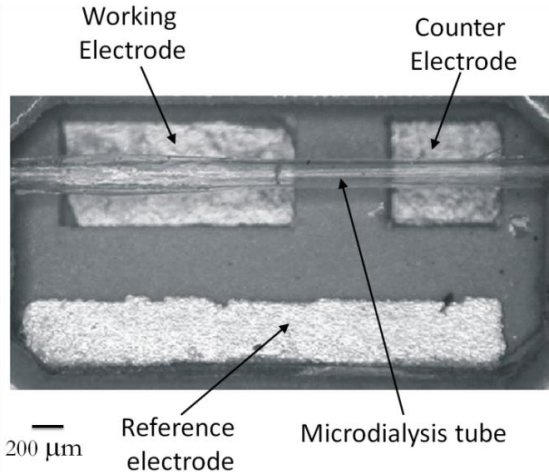


Fig. 9.39. Reaction cell with attached microdialysis tube [19].

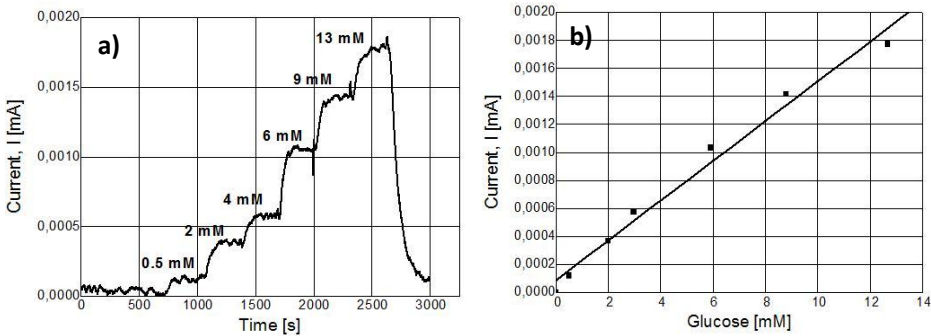


Fig. 9.40. (a) Dynamic response and (b) calibration curve of the LTCC glucose sensor [20].

Electrochemical sensor for heavy metal determination in biomedical and environmental fluids

The LTCC-based manifold for heavy metal detection using anodic stripping voltammetry is presented in Fig. 9.41. The anodic stripping voltammetry is an electrochemical method for quantitative determination of specific ions in the test solution. The detected analyte is firstly electroplated on the surface of the working electrode (WE) and then oxidized on the electrode during the stripping step. In the electroplating step the WE potential is held at a relatively low level. The potential should be low enough to reduce the analyte deposit on the electrode. During the stripping step the potential is rising what results in an oxidation of the analyte. As a result of the oxidation the analyte gives off the electrons which can be measured as a current. The sensor structure is made of seven LTCC. It consists of two fluidic inlets, microchannels, a spiral passive mixer (when a reagent addition is necessary), a measuring cavity, an electrode array and a fluidic outlet.

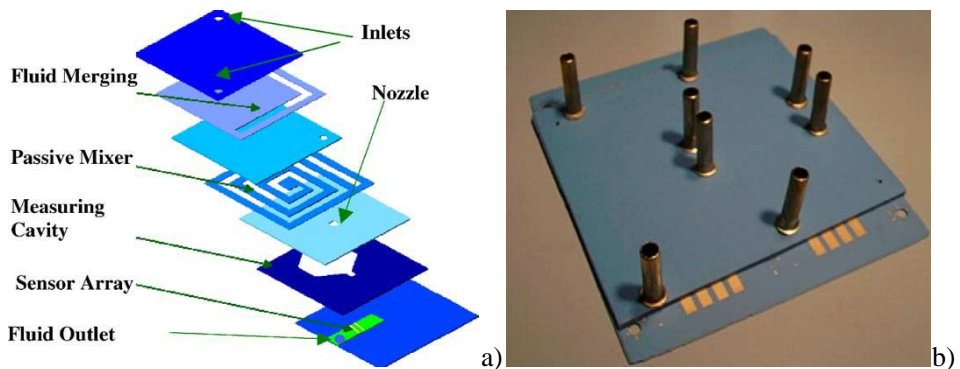


Fig. 9.41. LTCC-based electrochemical sensor: (a) layers for device, (b) fabricated structure [21].

The electrode array for electrochemical measurements is fabricated using thick-film screen printable pastes. The sensor array is composed of

silver/silver chloride reference electrode, a gold counter electrode and two gold working electrodes. The reference electrode is obtained by silver electro-deposition in a solution of AgNO_3 and NH_4OH . The experimental results of square-wave anodic stripping voltammetry obtained for increasing concentrations of copper and mercury are presented in Fig. 9.42.

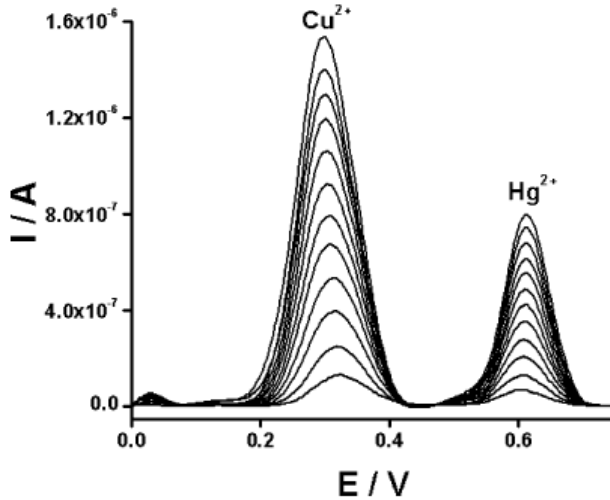


Fig. 9.42. Square-wave stripping responses for increasing concentrations of copper and mercury [21].

9.6. Optical sensors

LTCC-based microfluidic sensor for absorbance measurement

The principle of the sensor operation is based on light absorption by the medium (analyte) which flows in an analytical microchannel between two optical fibers. The changes in light intensity which approaches the photodetector are related to the changes in the analyte concentration. A light absorbance according to Lambert-Beer's law is defined as follows:

$$A \equiv \log\left(\frac{I_o}{I}\right) = c\epsilon l \quad (9.13)$$

where: I_o and I are intensities of the light, c is the molar concentration, ϵ is the molar absorptivity ($\text{cm}^{-1}\text{M}^{-1}$) and l is the optical path length. So it can be noticed that for the same conditions of measurement (the same optical path lengths and molar absorptivity of measured solution) the absorbance is proportional to the concentration of considered chemical in a particular solution. The LTCC microfluidic sensor for absorbance measurements presented in Fig. 9.43 consists of fluidic channels, channels for optical fibers and two polymeric optical fibers. The light emitting diode (LED) is applied as a light source and photodiode coupled with an amplifier and color filter is applied as a light detector.

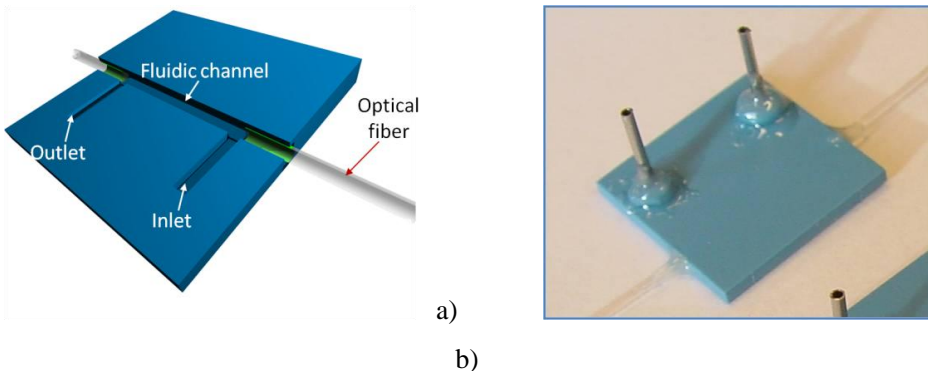


Fig. 9.43. LTCC-based microfluidic optical sensor: (a) schematic view and (b) photograph [22].

The measured output signal is proportional to the light intensity coming to the light detector device. So it is possible to measure the light absorbance versus the concentration of analyte utilizing the following formula:

$$A(c) \equiv \log\left(\frac{I_o}{I(c)}\right) = \log\left(\frac{U_o}{U(c)}\right) \quad (9.14)$$

where U_o is the output voltage for pure water and $U(c)$ is the voltage level related to concentration c . The results of the absorbance measurements for the LTCC sensor are given in Fig. 9.44.

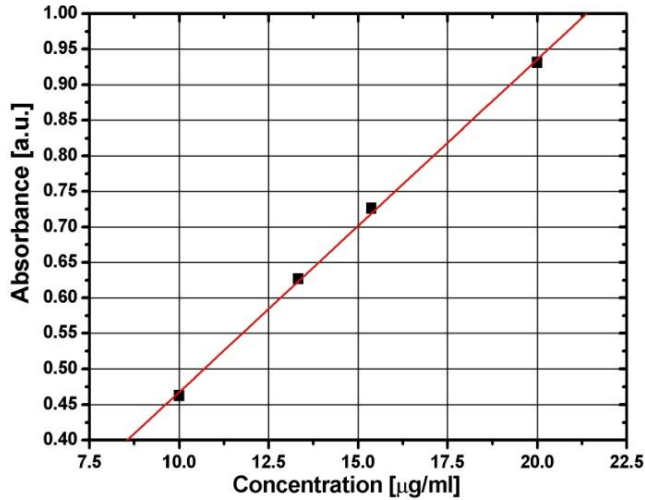


Fig. 9.44. Light absorbance vs. concentration of Sunset Yellow dye measured at wavelength $\lambda = 468$ nm [22].

LTCC-based fluorescent sensor

The LTCC technology is applied to fabrication of a fluorescent detection module. The principle of the presented device operation is based on fluorescence activated cell detection. The LTCC-based fluorescent sensor presented in Fig. 9.45 consists of a microfluidic chamber, two polymeric fibre optics, a miniature light source (UV light emitting diode) and a photodetector (photodiode integrated with an amplifier and a color filter in one CMOS structure).

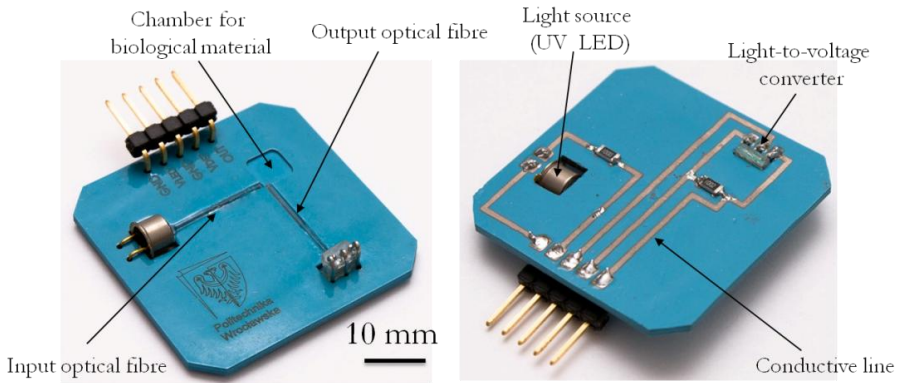


Fig. 9.45. LTCC-based fluorescent sensor [23].

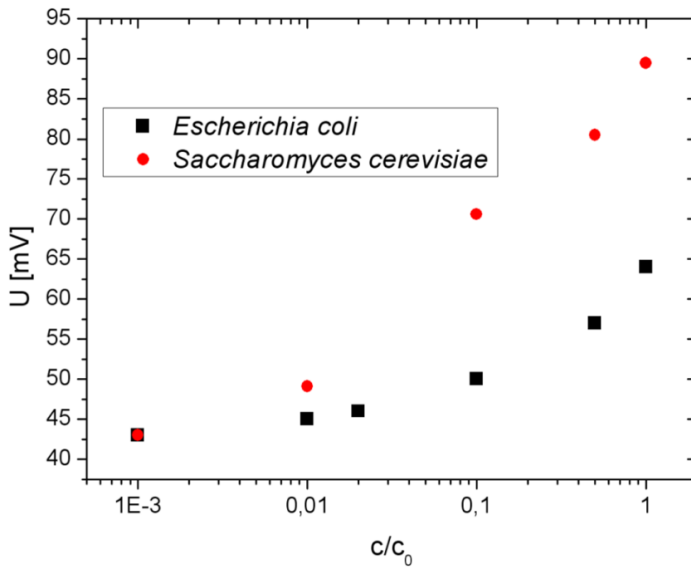


Fig. 9.46. Response of the LTCC-based fluorescent sensor for various concentrations of *Escherichia coli* and *Saccharomyces cerevisiae* cells [23].

The sample is illuminated by UV light which is transmitted via the input optical fibre to the detection chamber. As a result of the light excitation the

cells start to emit blue fluorescent light. The fluorescence signal is collected by the output optical fibre connected to the photodetector. Light intensity is converted to output voltage signal by the photodetector. Exemplary results of the fluorescence measurements for different concentrations of *Escherichia coli* and *Saccharomyces cerevisiae* cells are given in Fig. 9.46.

LTCC-based microfluidic system with optical detection

The LTCC microfluidic system with a heater, a temperature sensor and integrated optical fibers for optical measurements is presented in Fig. 9.47. The integration of heating and temperature sensor elements gives the possibility to obtain the desired temperature level and its distribution inside the ceramic structure. The LTCC device is adapted for absorbance (parallel configuration of the optical fibers) and fluorescence (perpendicular configuration of optical fibers) measurements. The microfluidic part of the device consists of fluid inputs/output, Y-shape reagents junction, a 30 cm long mixing meander and a detection channel.

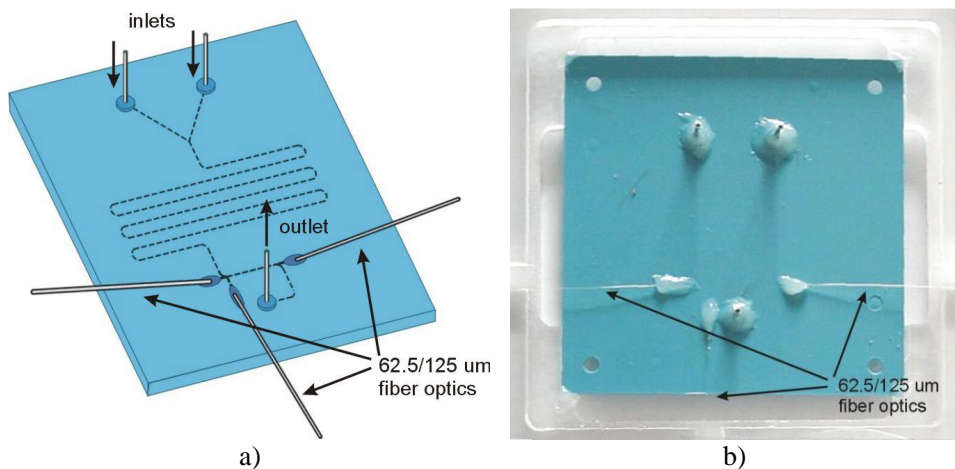


Fig. 9.47. LTCC microfluidic system (a) designed structure, (b) photograph [24].

During measurements, the light from the LED is transmitted via one optical fiber to the detection channel in the microsystem. The parallel and perpendicular fibers are connected with the photomultiplier of the spectrofluorimeter. Exemplary results of absorbance and fluorescence measurements are presented in Fig. 9.48.

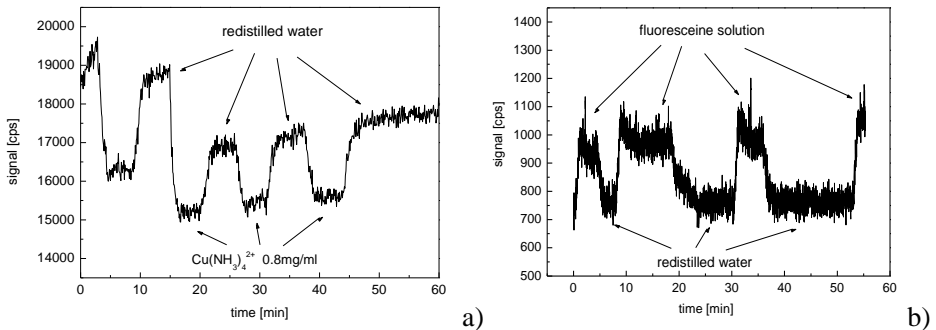


Fig. 9.48. Results of (a) absorbance and (b) fluorescence measurements [24].

References

- [1] Khanna PK, Hornbostel B, Grimme R, Schäfer W, Dorner J, Miniature pressure sensor and micromachined actuator structure based on low-temperature-cofired ceramics and piezoelectric material, *Materials Chemistry and Physics*, 87 (2004) 173-178.
- [2] Khanna PK, Ahmad S, Grimme R, Molecular Weiss domain polarization in piezoceramics to diaphragm, cantilever and channel construction in low-temperature-cofired ceramics for micro-fluidic applications, *Materials Chemistry Physics*, 89 (2005) 56-63.
- [3] Sobociński M, Juuti J, Jantunen H, Golonka LJ, Piezoelectric unimorph valve assembled on an LTCC substrate, *Sensors and Actuators A: Physical*, 149 (2009) 315-319.

- [4] Huang et al., Proc. 6th International Conference and Ceramic Microsystems Technologies, 2010.
- [5] Sethu P, Mastrangel CH, Polyethylene glycol (PEG)-based actuator for nozzle-diffuser pumps in plastic microfluidic systems, *Sensors and Actuators A: Physical*, 104 (2003) 283-289.
- [6] Gongora-Rubio MR, Espinoza-Vallejos P, Sola-Laguna L, Santiago-Avilés JJ, Overview of low temperature co-fired ceramics tape technology for meso-system technology (MsST), *Sensors and Actuators A: Physical*, 89 (2001) 222-241.
- [7] da Cunha MR, Saul CK, Gongora-Rubio MR, Numerical and experimental analysis of microfluidic diode manufactured in LTCC technology, *Proc. International Conference IBERSENSOR*, 2006, 1-5.
- [8] Nguyen NT, Wu Z, Micromixers – a review, *Journal of Micromechanics and Microengineering*, 15 (2005) R1-R16.
- [9] Bau HH, Zhong J, Yi M, A minute magneto hydro dynamic (MHD) mixer, *Sensors and Actuators B: Chemical*, 79 (2001) 207-215.
- [10] Yi M, Bau HH, The kinematics of bend-induced mixing in micro-conduits, *International Journal of Heat and Fluid Flow*, 24 (2003) 645-656.
- [11] Malecha K, Golonka LJ, Bałdyga J, Jasińska M, Sobieszuk P, Serpentine microfluidic mixer made in LTCC, *Sensors and Actuators B: Chemical*, 143 (2009) 400-413.
- [12] Malecha K, Pijanowska DG, Golonka LJ, Torbicz W, LTCC microreactor for urea determination in biological fluids, *Sensors and Actuators B: Chemical*, 141 (2009) 301-308.
- [13] Budniewski K, Golonka LJ, Zawada T, Roguszczak H, Dobosz T, Jonkisz A, Design and FEM analysis of novel microchamber PCR device

- fabricated in LTCC technology, Proc. 28th International Conference of IMAPS Poland Chapter, Wrocław (Poland), September 2004, 191-194.
- [14] Sadler DJ, Changrani R, Roberts P, Chou CF, Zanhausern F, Thermal management of BioMEMS: temperature control for ceramic-based PCR and DNA detection devices, IEEE Transactions on Components and Packaging Technologies, 26 (2003) 309-316.
- [15] Chou CF, Changrani R, Roberts P, Sadler D, Burdon J, Zenhausen F, Lin S, Mulholland A, Swami N, Terbrueggen R, A miniaturized cyclic PCR device – modeling and experiments, Microelectronic Engineering, 61-62 (2002) 921-925.
- [16] Bembnowicz P, Małodobra M, Kubicki W, Szczepańska P, Górecka-Drzazga A, Dziuban J, Jonkisz A, Karpiewska A, Dobosz T, Golonka LJ, Preliminary studies on LTCC based PCR microreactor, Sensors and Actuators B: Chemical, 150 (2010) 715-721.
- [17] Malecha K, Pijanowska DG, Dawgul M, Golonka LJ, Torbicz W, LTCC fluidic potentiometric detector, Proc. 31st IEEE International Spring Seminar on Electronic Technology, Budapest (Hungary) , May 2008, 498-503.
- [18] Grabowska I, Ksok E, Wyzkiewicz I, Chudy M, Miniaturized module with biosensors for potentiometric determination of urea, Microchimica Acta, 164 (2009) 299-305.
- [19] Malecha K, Pijanowska DG, Golonka LJ, Kurek P, Low temperature co-fired ceramic (LTCC)-based biosensor for continuous glucose monitoring, Sensors and Actuators B: Chemical, (2011) doi:10.1016/j.snb.2011.01.002.
- [20] Malecha K, Pijanowska DG, Golonka LJ, Kurek P, LTCC flow-through amperometric sensor for glucose determination, Proc. 5th IMAPS/ACerS

International Ceramic Interconnect and Ceramic Microsystem Technologies, Denver (USA), April 2009, 157-162.

- [21] Gongora-Rubio MR, Fontes MBA, da Rocha ZM, Richter EM, Angnes L, LTCC manifold for heavy metal detection system in biomedical and environmental fluids, *Sensors and Actuators B: Chemical*, 103 (2004) 468-473.
- [22] Malecha K, Zawada T, Golonka LJ, LTCC based microfluidic optical detector, *Proc. 28th IEEE International Spring Seminar on Electronic Technology*, Wiener Neustadt (Austria), May 2005, pp. 347-351.
- [23] Malecha K, Czok M, Hetnar A, Pawlik A, Sztajer H, Golonka LJ, Micro ceramic cell analyzer (MCCA) - preliminary results, *Proc. 34th International Conference and Exhibition IMAPS-CPMT Poland*, Wrocław (Poland), September 2010.
- [24] Golonka LJ, Roguszczak H, Zawada T, Radojewski J, Grabowska I, Chudy M, Dybko A, Brzózka Z, Stadnik D, LTCC based microfluidic system with optical detection, *Sensors and Actuators B: Chemical*, 111-112 (2005) 396-402.